

# Earthquake Moment-Area Scaling Relations and the Effect of Fault Heterogeneity on Slow to Fast Earthquake Slip

Thesis by  
Yingdi Luo

In Partial Fulfillment of the Requirements for the  
degree of  
Doctor of Philosophy

The logo for the California Institute of Technology (Caltech), featuring the word "Caltech" in a bold, orange, sans-serif font.

CALIFORNIA INSTITUTE OF TECHNOLOGY  
Pasadena, California

2018  
Defended July 31, 2017

© 2018

Yingdi Luo

ORCID: 0000-0002-1165-6107

All rights reserved except where otherwise noted

## ACKNOWLEDGEMENTS

Pursuing a Ph.D. at Caltech has been the most wonderful journey and once-in-a-lifetime experience to me. For the past almost seven years, I have enjoyed beautiful sunshine of the Golden State, and the ultimate hospitality from local Californians. But most importantly, I enjoyed working with many many amazing and most talented researchers and fellows at Caltech, who have accompanied me and shaped me in so many ways.

First and foremost, I would like to thank Pablo Ampuero, who is not only my Ph.D. advisor, but more the mentor of my life. Pablo has a sharp mind, keen observation, and is always full of energy and curiosity. Working together we have brainstormed so many amazing ideas, although most of them are just gone with the wind because of my laziness and dumbness. Nevertheless, Pablo has always been absolutely supportive and patient on my slow progress and sloppiness from time to time. Thank you for being so awesome!

I would also like to thank Don Helmberger. Being my co-advisor in my first year, Don has again and again stunned me with his enigmatically sophisticated knowledge in seismology: having a peek on a seismogram, pointing to some arrival phases and telling me 'Hey I bet there's some rough structure near the interface' sounded like magic to me, but Don proved it to be solid science. Don is simultaneously serious and humorous. Thank you for being so amazing!

I would like to thank my former academic advisor Victor Tsai and Jennifer Jackson, who helped me a lot caring for my academic progress and giving useful advices.

I would also like to thank the rest of my thesis committee members: Rob Clayton, Jean-Philippe Avouac and Nadia Lapusta, for dedicating your precious time to reading my thesis and tracking its progress.

I thank a lot the rest of the faculty members of the Seismological Laboratory and of the Division of Geological and Planetary Sciences of Caltech, who I had classes with, who had chatted and discussed with me, or inspirited me in various ways, especially Zhongwen Zhan (also former officemate and good friend, lot of crazy

discussion together), Mark Simons (being on my TAC committee, unfortunately absent from my Thesis committee due to time conflicts), Hiroo Kanamori, Tom Heaton, Joann Stock, Mike Gurnis, Paul Asimow and Joe Kirschvink.

I would as well thank all my colleagues that I worked with and helped me in various ways: Paul Somerville at AECOM, Anatoly Petukhin at GRI, Heidi Houston at U. Washington, Bruce Shaw at Lamont, Allan Rubin at Princeton, Zhen Liu at JPL, Risheng Chu and Sidao Ni at China Academy of Science, Yoshi Kaneko at GNS, NZ, Sylvain Barbot at NTU, SG.

I thank Xiaofei Chen, my undergraduate advisor, who opened the door for me to the amazing world of Geophysics and recommended me over to Caltech, the best place to study Geophysics.

I would also like to say thank you to all the current and former Seismo Lab and GPS staff, especially Donna, Priscilla, Julia, Kim, Julie, Dian, Viola, Rosemary and Naveed. I thank you all for your dedicated work. I really enjoyed chatting with all of you.

Thank you to my best buddies here, Junle (buddy home-towner), Lingsen (gym partner and gaming buddy), Zhan (buddy USTC'er and a good cook), Dongzhou (amazing Wiki contributor), Yiran and Dunzhu (Seismolab cohort and lovely couple), Yihe (great event organizer), Kangchen (genius computer geek), Xiaolin (in the lab every weekend). I really enjoy hanging out with you, guys.

I thank all the other current and former members of our research group: Jess, Asaf, Surendra, Zacharie, Olivier, Han, Benjamin, Bryan, Percy. It is a great pleasure to work with you guys and I learned a lot.

I also want to thank all current and former officemates in SM368: Rachel (unlimited cookie supply!), Chris, Ethan, Celeste, Natalia, Albert, Michelle, Dan, Qingyang. You all made the office welcoming and vivid, especially all my current officemates, who must be tolerating a lot with my endless and endless typing on my ultra-clicky mechanical keyboard recently. Thank you for your understanding!

High five to my basketball fellows: Shengji, Fan-chi, Justin, Naofumi, Zhong-

wen, and occasionally Victor. I'm not a particularly good player, but I enjoy playing with you, guys.

I also thank other Seismo Lab and GPS fellows: Zhihong, Daoyuan, Bing, Xi-angyan, Ting, Wei, Yanghui, Voon, Semechah, Minyan, Zhe, Xi Zhang, Xuan, Brent, Miki, Lingling, Xi Liu, Men-Andrin, Junjie, Hao. You are all wonderful!

Thank you as well to other fellow students at Caltech: Linghu, Wendy, Liang, Jiang and Brian for being nice to me.

My gratitude also goes to Ta-liang, former Seismological Laboratory fellow and USC professor emeritus of Geophysics, and Evelyn, USC professor emeritus of Neurology, for taking care of me and treating me like their child. You are so nice!

I owe my special thanks to my fiancée Vera, for your love and understanding. Having 2500 miles apart is tough. Having a Ph.D. candidate boyfriend is tougher. Having a Ph.D. candidate boyfriend 2500 miles away who is dull and stupid is  $\tan \frac{\pi}{2}$  tough. Yet we have overcome all kinds of strenuous terrains holding hands together. With you, my life is meaningful and colorful, and thus we journey on.

Last but not least, I thank my parents, Jianhua and Yunqing, for your unconditional love and eternal support on whatever I do. I feel sorry for being so far away as the only child they have. My mom cried when I went to USTC, 300 miles away from home. Now I'm in the States, 6000 miles away. Thus I also thank my fellow golden-retriever, "HuTou", ("Tiger-head" in Chinese), for taking my role and accompanying my parents.

I love you all.

Thank you! Thank you all!

感谢大家!

## ABSTRACT

Earthquake moment-area scaling relations play a key role in both earthquake physics studies and earthquake hazard assessment. A three-stage moment-area relation, based on advances in earthquake source inversion, is currently in use in Japan. The second stage has a scaling exponent outside the range of commonly accepted models of small and very large earthquakes. We develop theoretical insight on the mechanical origin of this second-stage scaling. We utilize an analytical dislocation model, a numerical crack model and multi-cycle rate-and-state simulations of strike-slip faults with heterogeneous friction properties. We find that the second stage in earthquake moment-area scaling results from a combination of surface rupture effects, comprising an effective rupture elongation along-dip due to a mirror effect and systematic changes of the shape factor relating slip to stress drop. Based on this physical insight, we propose a simplified formula to account for these effects in moment-area scaling relations.

Geological, seismological, geodetic and experimental studies provide evidence of the heterogeneous structure of natural faults. To advance our understanding of the mechanical role of fault heterogeneity on the diversity of earthquake slip behavior, we conduct a theoretical and computational study of heterogeneous fault models. We consider faults with a mixture of frictionally stable and unstable materials and spatial contrasts of fault zone pore fluid pressure, akin to hydraulically sealed brittle asperities embedded in a ductile fault zone matrix. We first study faults with a regular alternation of materials, using linear stability analysis and quasi-dynamic rate-and-state simulations. We find transitions in fault behavior from fast to slow earthquakes to steady slip, and determine how these transitions depend on the composition and strength contrast of the material mixture. Based on these results, we develop rate-and-state models with stochastic distributions of brittle asperities in a ductile matrix to study slow slip and tremor phenomena. We focus on the hierarchical patterns of tremor migration observed in subduction zones, which feature distinct tremor propagation speeds in different directions. Our models are in quantitative agreement with observations of episodic slow slip and tremor events in Cascadia. We discovered that, in contrast to a common view, slow slip might well be a result of tremor activity rather than its cause. The collective interaction of asperities with a broad range of material properties, mediated by creep, is a novel and robust

mechanism for the generation of slow slip events. We find that the hierarchical patterns of tremor migration and the nucleation locations of tremor swarms provide constraints on fault rheology. Our study also shows that, despite multiple asperity interactions, there is a close relation between tremor rate and the underlying slip rate which supports an approach to constrain slow slip rate via observed tremor rates.

## PUBLISHED CONTENT AND CONTRIBUTIONS

Luo, Y., J. P. Ampuero, K. Miyakoshi, and K. Irikura, (2017).

"Surface Rupture Effects on Earthquake Moment-Area Scaling Relations."

*Pure and Applied Geophysics*, 1-12, doi:10.1007/s00024-017-1467-4.

Luo and Ampuero co-designed study and analyzed theoretical models. Luo performed all the rate-and-state simulations and analyzed the results; produced all figures and drafted the manuscript. Miyakoshi and Irikura inspired the study and contributed to content of observations and addressing corresponding reviewers' comments. Both Luo and Ampuero contributed to interpreting the results and real-world implications.

Y. Luo, J. P. Ampuero, P. Galvez, M. van den Ende and B. Idini (2017).

"QDYN: a Quasi-DYNamic earthquake simulator (v1.1)"

*Zenodo*. doi:10.5281/zenodo.322459

Luo and Ampuero co-developed the numerical code. Luo developed most pre-processing and post-processing packages and example packages; drafted the code manual. Galvez implemented MPI, van den Ende and Idini developed additional functionalities of the code and Python wrappers.

Y. Luo and J. P. Ampuero, (2017)

"Stability and effective friction of faults with heterogeneous friction properties and fluid pressure"

Submitted

Luo and Ampuero co-designed study. Luo performed all rate-and-state simulations and analyzed the results; derived all linear stability analysis and corresponding simplifications; produced all figures and drafted the manuscript. Both Luo and Ampuero contributed to interpreting the results and real-world implications.

## TABLE OF CONTENTS

Acknowledgements . . . . .	iii
Abstract . . . . .	vi
Table of Contents . . . . .	ix
Chapter I: Introduction . . . . .	1
Chapter II: Surface rupture effects on earthquake moment-area scaling relations	3
2.1 Introduction . . . . .	3
2.2 A rate-and-state earthquake cycle model . . . . .	6
2.3 Dislocation models . . . . .	11
2.4 Crack models . . . . .	15
2.5 Conclusions . . . . .	19
Chapter III: Stability and effective friction of faults with heterogeneous friction properties and fluid pressure . . . . .	24
3.1 Introduction . . . . .	25
3.2 Rate-and-state models . . . . .	30
3.3 Linear stability analysis . . . . .	38
3.4 Prediction of instability boundaries . . . . .	45
3.5 Discussion and conclusions . . . . .	53
3.6 Appendices . . . . .	55
Chapter IV: Tremor migration patterns and the collective behavior of deep asperities mediated by creep . . . . .	66
4.1 Introduction . . . . .	67
4.2 Modeling . . . . .	71
4.3 Results . . . . .	85
4.4 Discussion . . . . .	94
4.5 Conclusions . . . . .	100
Appendix A: Supplements . . . . .	108
Appendix B: Numerical code: QDYN - Quasi-Dynamic earthquake simulator	110

*Chapter 1*

## INTRODUCTION

This dissertation on theoretical and computational earthquake modeling includes two parts.

Part I consists of Chapter 2 and is focused on the mechanical origin of earthquake moment-area scaling relations. It is based on material published in

Luo, Y., Ampuero, J. P., Miyakoshi, K., and Irikura, K. (2017).

Surface Rupture Effects on Earthquake Moment-Area Scaling Relations.

Pure and Applied Geophysics, 1-12, doi:10.1007/s00024-017-1467-4.

Topical Volume on "Best Practices in Physics-based Fault Rupture Models for Seismic Hazard Assessment of Nuclear Installations"

In this chapter we explore the origin of an intriguing intermediate regime in a scaling relation between earthquake moment and rupture area currently in use for ground motion prediction in Japan, which has a scaling exponent outside the range of exponents predicted by commonly accepted models of small and very large earthquakes. This scaling regime for earthquakes of intermediate sizes, or “second stage”, is scarcely studied but critical for earthquake hazard assessment; ignoring it can lead to underestimation of the seismic moment that can be released by a fault of a certain size. To investigate the mechanical origin of the second stage, we utilize an analytical dislocation model, a numerical crack model and multi-cycle rate-and-state simulations. The latter comprise heterogeneous strike-slip faults with stochastic spatial distributions of characteristic slip distance. We find that the second stage emerges from a combination of surface rupture effects, comprising an effective rupture elongation along-dip due to a mirror effect and systematic changes of the shape factor relating slip to stress drop. Based on this physical insight, we propose a simplified formula to account for these effects in moment-area scaling relations.

Part II consists of Chapters 3 and 4 and is focused on the effect of fault heterogeneity on the diversity of earthquake slip behavior. The two chapters are based on one submitted manuscript and one manuscript in preparation for submission. In

Chapter 3 we study a heterogeneous fault model with a regularly alternating mixture of competent and incompetent materials and spatial contrasts of fault zone pore fluid pressure. We find that fault behaviors transit from fast earthquakes to slow earthquakes, and to completely stable (steady sliding), controlled by both the mixture composition (the proportion of brittle and ductile materials) as well as the relative strength between the two alternating materials (via difference in pore pressure). We then utilize an analytical method, Linear Stability Analysis, and find it predicts the overall fault stability very well. We further study the fault stability with heuristic approximations based on physical insights, and propose simple criteria that accurately predict the stability of slip on a heterogeneous fault.

Based on this fundamental study, in Chapter 4 we develop a model of competent asperities with stochastic properties embedded in a frictionally stable fault matrix. We find that, compared to the regularly alternating model, the model with stochastic heterogeneity permits slow slip behavior over a much wider range of model parameters. The model reproduces the hierarchical tremor migration patterns and accompanying slow slip events in quantitative agreement with observations in the Cascadia subduction zone. The tremor activities observed in Cascadia feature distinct tremor propagation speeds in different directions, including Rapid Tremor Reversals (RTR, backward propagating tremor) with a propagating speed 5-50 times faster than the forward tremor migration. We compared two end-member models, which differ by the assumed rheology of the fault zone matrix: in one model slow slip drives tremor, in the other tremor drives slow slip. Comparing the two models with observations we find that, in contrast to a common view, slow slip is likely the result of tremor activity rather than the cause.

Part I and Part II are related by the use of rate-and-state models that incorporate fault heterogeneities. These are building blocks towards the ultimate goal to understand the mechanics underlying the broad range of fault slip behaviors observed in nature, from small to large, slow to fast.

In the appendix we present the software QDYN, the Quasi-Dynamic earthquake simulator we have developed and utilized for this work. It is a boundary element software to simulate earthquake cycles under the quasi-dynamic approximation, which is already in use by other teams internationally.

*Chapter 2***SURFACE RUPTURE EFFECTS ON EARTHQUAKE  
MOMENT-AREA SCALING RELATIONS****Abstract**

Empirical earthquake scaling relations play a central role in fundamental studies of earthquake physics and in current practice of earthquake hazard assessment, and are being refined by advances in earthquake source analysis. A scaling relation between seismic moment ( $M_0$ ) and rupture area ( $A$ ) currently in use for ground motion prediction in Japan features a transition regime of the form  $M_0 \sim A^2$ , between the well-recognized small (self-similar) and very large ( $W$ -model) earthquake regimes, which has counter-intuitive attributes and uncertain theoretical underpinnings. Here, we investigate the mechanical origin of this transition regime via earthquake cycle simulations, analytical dislocation models and numerical crack models on strike-slip faults. We find that, even if stress drop is assumed constant, the properties of the transition regime are controlled by surface rupture effects, comprising an effective rupture elongation along-dip due to a mirror effect and systematic changes of the shape factor relating slip to stress drop. Based on this physical insight, we propose a simplified formula to account for these effects in  $M_0 - A$  scaling relations for strike-slip earthquakes.

**2.1 Introduction**

Earthquake scaling relations are empirical relations between source parameters, such as seismic moment, rupture dimensions and average slip (e.g. Leonard 2010). They are significant in basic earthquake physics studies, as they constitute a first-order synthesis of static source properties to constrain earthquake mechanics models. They are also practically important as a key component of earthquake hazard assessment and ground motion prediction. Recent advances in observational techniques and source inversion methods are providing opportunities to refine the empirical relations between seismic moment and rupture geometry (Miyakoshi et al. 2015; Murotani et al. 2015) and to better understand their underlying physics.

Observations of strike-slip earthquakes show two end-member regimes in the scaling of seismic moment ( $M_0$ ) vs. rupture area ( $A$ ):  $M_0 \sim A^{3/2}$  for small earthquakes and  $M_0 \sim A$  for very large ones. Intuitively, the transition between these two regimes

should be  $M_0 \sim A^n$  with an exponent  $n$  taking intermediate values,  $1 < n < 3/2$ . However, some authors have proposed values of  $n$  larger than  $3/2$ . In particular, [Irikura and Miyake \(2011\)](#) introduced a  $M_0$  vs.  $A$  scaling relation with three scaling regimes (referred to hereafter as Stages 1, 2 and 3, in increasing order of  $M_0$ ) and  $n = 2$  at intermediate magnitudes (see also [\(Fujii and Matsu'ura 2000; Hanks and Bakun 2002; Irikura and Miyake 2001; Matsu'ura and Sato 1997; Murotani et al. 2015\)](#)). [\(Figure 2.1\)](#) shows the current version of the 3-stage scaling relation calibrated by [Murotani et al. \(2015\)](#). In contrast to previous studies that suffer from significant uncertainties on the rupture area (e.g. [Wells and Coppersmith 1994](#)), the work of [Irikura and Miyake \(2011\)](#) and follow up work are primarily based on rupture areas derived from kinematic source inversions ([Miyakoshi et al. 2015; Murotani et al. 2015; Somerville et al. 1999; Song et al. 2008](#)). While the empirical data strongly supports Stage 1, evidence for Stage 3 has been the subject of a long-standing debate due to the limited number of very large strike-slip earthquakes ([Romanowicz and Rundle 1993; Scholz 1982](#)). [Hanks and Bakun \(2002\)](#) and [Irikura and Miyake \(2001\)](#) independently proposed Stage 2, [Murotani et al. \(2015\)](#) calibrated its properties based on slip distributions inferred by source inversion, and [Miyakoshi et al. \(2015\)](#) analyzed a large amount of crustal earthquakes in Japan to confirm the existence of Stage 2. Our focus here on the 3-stage scaling relation introduced by [Irikura and Miyake \(2011\)](#) and calibrated by [Murotani et al. \(2015\)](#) is motivated by its wide adoption in ground motion prediction studies in Japan. The study of the 3-stage model, especially the least understood Stage 2, is of great importance in earthquake hazard estimation because the seismic moment predicted for a given rupture area, and hence strong ground motions, can be significantly higher if predictions include Stage 2.

The present work aims at developing a mechanical model consistent with Stage 2, namely  $M_0 \sim A^2$  for  $10^{19} N.m < M_0 < 1.8 \times 10^{20} N.m$  or moment magnitude  $M_w$  6.6 to 7.5 ([Murotani et al. 2015](#)). Stage 1 is classically explained by a self-similar rupture model, e.g. a circular crack with scale-independent stress drop. Stage 3 is naturally explained by the so-called  $W$ -model, a rupture very elongated along-strike with scale-independent depth extent and stress drop ([Bodin and Brune 1996; Leonard 2010; Mai and Beroza 2000; Scholz 1982](#)). Due to the limited number of available observations of very large strike-slip earthquakes, other models like the  $L$ -model have also been advocated ([Hanks and Bakun 2002](#)). Three main models have been proposed to explain Stage 2: rupture penetration below the seismogenic zone ([Shaw 2009; Shaw and Wesnousky 2008](#)), effect of the viscous asthenosphere ([Matsu'ura](#)

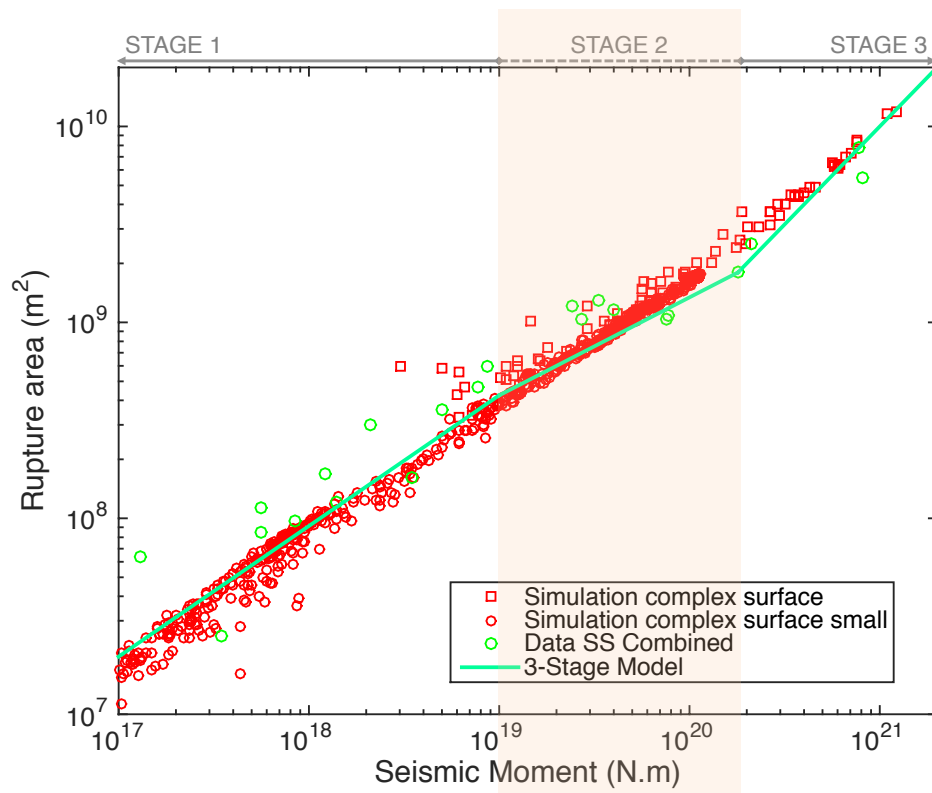


Figure 2.1: Earthquake seismic moment ( $M_0$ ) vs. rupture area ( $A$ ) empirical and simulation data and 3-stage scaling model. Green curve: empirical 3-stage relation by Murotani et al. (2015). Green circles: observational data from kinematic inversion of vertical strike-slip faults (Miyakoshi et al. 2015; Murotani et al. 2015; Somerville et al. 1999). Red circles and squares: synthetic earthquake data from our rate-and-state simulation of “reduced-scale” and “full-scale” models, respectively.

and Sato 1997), and scale-dependent stress drop (Dalguer et al. 2008). On the one hand, evidence for the deep rupture penetration required by Shaw’s model (up to 46 km depth in Figure 2.2) and for scale-dependent stress drop are scarce (e.g. Hanks and Bakun 2014). On the other hand, the model by (Matsu’ura and Sato 1997) assumes that the depth of the lithosphere and the depth of the seismogenic zone are the same, which is inconsistent with the current view that faults slip aseismically in the lower crust. Hence, the mechanical origin of Stage 2 remains unclear.

In this study, we develop a mechanical model consistent with the 3-stage  $M_0 - A$  scaling relation of Murotani et al. (2015). We show that the existence of Stage 2 can be attributed to surface rupture effects, even if stress drop is constant. Thus the effects of scale-dependent stress drop, deep rupture penetration and deeper viscous rheology, while possibly present, can be considered as secondary. In Section 2.2 we

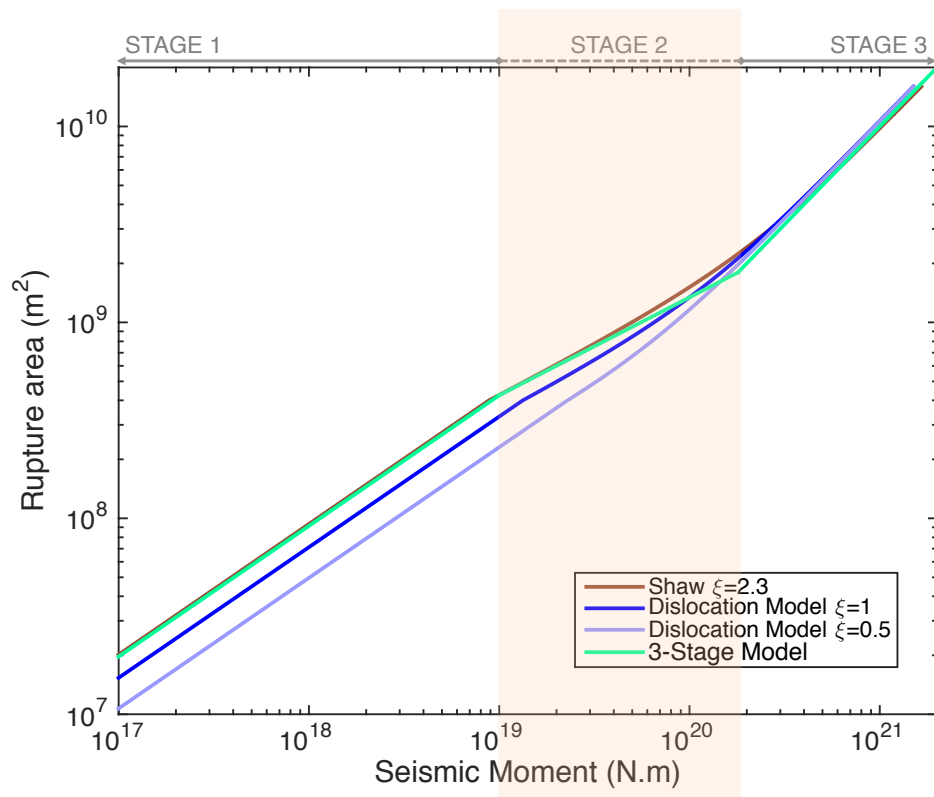


Figure 2.2: Earthquake M0 - A relations for dislocation and deep rupture penetration models. Brown curve: deep penetration model (Shaw 2009; Shaw and Wesnousky 2008). Dark blue curve: our dislocation model with free surface (Model D2,  $\xi = 1$ ). Light blue curve: our dislocation model without free surface (Model D1,  $\xi = 0.5$ ). Green curve: empirical 3-Stage relation by Murotani et al. (2015). Model D2 has Stage 2 while model D1 does not, which indicates that the free surface is key to Stage 2.

present results of rate-and-state earthquake cycle simulations with a wide magnitude range that are consistent with the observational data and the 3-stage scaling relation. In Section 2.3 we investigate dislocation models and find a geometrical effect of the free surface that contributes to Stage 2. In Section 2.4 we develop crack models that fit the proposed 3-stage model and reveal a shape factor effect of the free surface that further contributes to Stage 2. Based on our numerical and analytical results, we propose a simplified equation that captures the 3-stage earthquake scaling relation.

## 2.2 A rate-and-state earthquake cycle model

We perform multi-cycle quasi-dynamic simulations on vertical strike-slip faults governed by rate-and-state friction with heterogeneous characteristic slip distance ( $D_c$ ). In contrast with dynamic rupture simulations of single earthquakes, multi-

cycle modeling does not require assumptions about initial stresses before each earthquake: heterogeneous stresses emerge spontaneously throughout the cycles and lead naturally to heterogeneous co-seismic slip distributions. The approach is similar to that developed in (Hillers et al. 2006, 2007), where more details can be found, but progress in computational capabilities allows us to adopt realistic values of the radiation damping coefficient. Our simulations are done with the boundary element method with adaptive time-stepping implemented in the software QDYN (Luo et al. 2017). The fault is governed by the laboratory-motivated rate-and-state friction law (Marone 1998). The friction parameter  $D_c$  is the characteristic slip distance of frictional evolution and controls the fracture energy and nucleation length (Rubin and Ampuero 2005). Two friction parameters,  $a$  and  $b$ , control the non-linear viscous resistance and slip-weakening rate of the frictional surface, respectively. Their competition leads to either Velocity-Weakening ( $VW$ ) behavior when  $a < b$ , allowing earthquake nucleation, or Velocity-Strengthening ( $VS$ ) behavior when  $a > b$ , promoting stable sliding (Scholz 1998). The distribution of frictional properties as a function of depth introduces  $VW$  to  $VS$  transitions at depth and near the surface controlled by the temperature dependence of  $a$  and  $b$  (Figure 2.3, Figure 2.4(c)). Our model faults have a reference seismogenic depth ( $W_{s\_ref}$ ) of 18 km defined as the width of the  $VW$  region (from 2 to 20 km depth). On natural faults the seismogenic depth is often defined by the lower depth of the distribution of hypocenters, which corresponds to the bottom of the  $VW$  region in our model. The effective normal stress increases linearly from 0 to 10 km depth until it saturates at 75 MPa based on the assumption that pore pressure increases at the same rate as the lithostatic stress at depth (super-hydrostatic pore pressure, e.g. Streit and Cox (2001)). We assume a stochastic, spatially correlated lognormal distribution of  $D_c$ . The model parameters are tuned so that each individual model produces seismic events of various magnitudes. In addition, in order to obtain events with a sufficiently wide range of magnitudes, we combine results from multiple models with different random seeds, correlation lengths  $L_{co}$  and ranges of  $D_c$  values. Typical values used in our rate-and-state simulations are provided in Table 2.1. Figure 2.3-right shows the  $D_c$  profile of a typical model. A thorough discussion of how model parameters affect the distribution of magnitudes will be published elsewhere (see also Hillers et al. 2006, 2007). A characteristic length scale of the problem is the nucleation size  $L_c = G \times D_c / ((b - a)\sigma)$ , where  $G$  is the shear modulus and  $\sigma$  is the effective normal stress. To reduce the computational cost, we combined two sets of simulations. A "full-scale" set targets Stages 2 and 3 on long faults (512 km length)

with minimum and average  $L_c$  of 2.7 km and 6 km, respectively, at the middle depth of the seismogenic zone. A "reduced-scale" set targets Stages 1 and 2 on smaller faults (64 km length) with half smaller  $D_c$  and finer mesh. The nucleation size also varies between models with different  $D_c$  ranges. The range of magnitudes obtained from these two sets of simulations have significant overlap, which allows us to verify that our composite approach does not generate artifacts in the scaling relations. The seismic events detected in all these simulations are combined in a single catalog with over 10,000 events whose seismic moments span over four orders-of-magnitude.

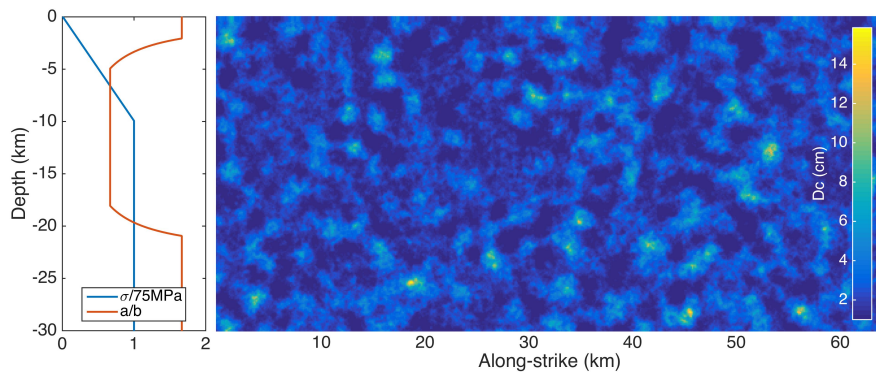


Figure 2.3: Rate-and-state model settings. Left: effective normal stress (blue curve) and  $a/b$  ratio (red curve) as a function of depth. The seismogenic zone ( $a/b < 1$ ) extends roughly from 2 to 20 km depth. Right: an example of heterogeneous distribution of characteristic slip distance  $D_c$  with correlation length of 1 km.

We detect seismic events based on slip-rate thresholds. Because of significant slip rate fluctuations caused by the strong heterogeneity of  $D_c$ , the event detection procedure artificially divides some large events into several smaller successive events. We crudely mitigate this unrealistic feature by treating events that occur less than 10 minutes apart as being part of the same rupture. This correction comes with the cost of possibly overlooking some very early aftershocks. However, manual inspection shows that the number of overlooked aftershocks is very limited, and our focus here is on earthquake scaling rather than individual events, hence the benefits of amendment greatly outweigh its limitations.

The small events in our simulated catalog have unrealistic, scale-dependent stress drops that may adversely affect the scaling results. Those unrealistic stress drops have two main origins. First, relatively large  $D_c$  values are used to keep the computational cost affordable, leading to large nucleation areas with large aseismic pre-slip within which co-seismic stress drops are unrealistically low. Second, our catalog

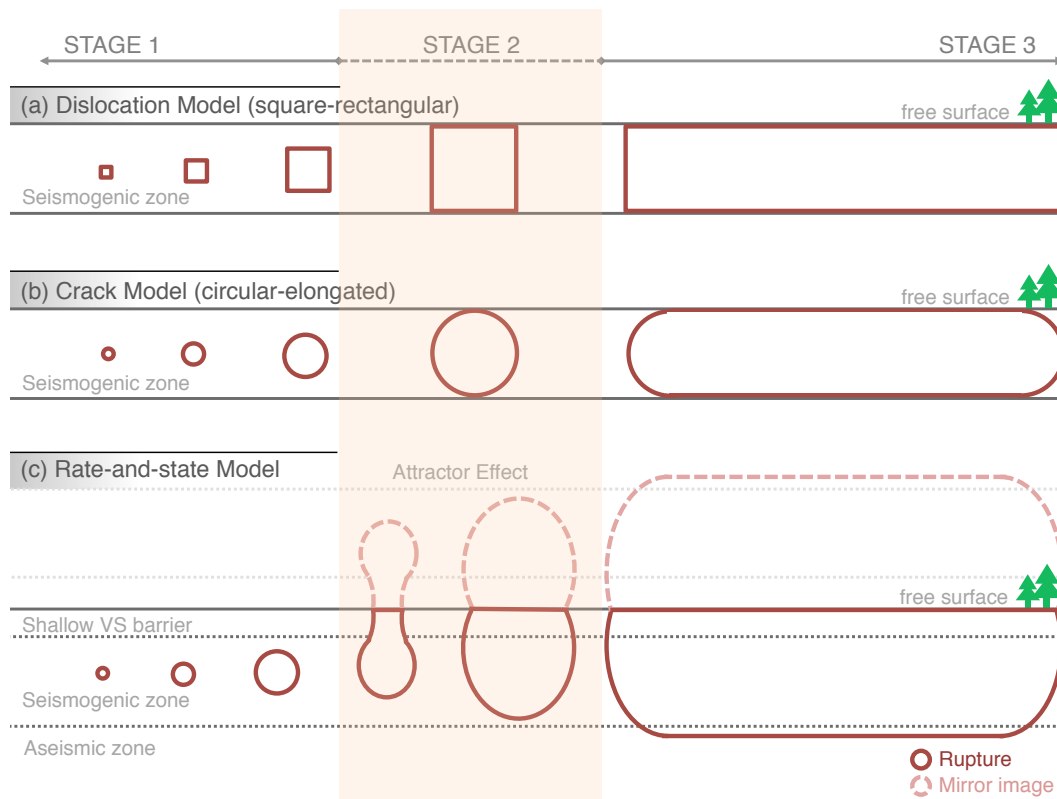


Figure 2.4: Rupture geometry in different models considered in this study. (a) Dislocation model with square to rectangular rupture transition. (b) Crack model with circular to elongated rupture transition. (c) Rate-and-state model with self-similar to elongated rupture transition. The free surface mirror image effect applies to all models. The "attractor effect" (coalescence between real and mirror image ruptures) enhances Stage 2 in the rate-and-state model.

still contains some ill-shaped early aftershocks which should have been considered as part of their mainshock rupture. Note that only events in Stage 1 are significantly affected by these artifacts, while in Stages 2 and 3, which span over 2 orders of magnitude, stress drops show no significant scale-dependency (Figure 2.5). The variability of stress drop in Stages 2 and 3 is much smaller than the variability inferred for real earthquakes: the standard deviation of  $\ln \Delta\tau$  (stress drop) from our rate-and-state simulations is 0.1, while from seismological estimates it is 0.7 or more (e.g. Table 1 of Causse and Song (2015)). To mitigate the stress drop artifacts and to focus on the effect of geometry and free surface on the moment-area scaling, we compute for each event in our simulated catalog the spatial average of stress drop over the rupture area (defined as the area where peak slip rate exceeds 1 cm/s), then we divide its moment by the average stress drop and multiply it by a reference stress drop  $\Delta\tau_{ref}$ . In the resulting modified catalog all events have the same average

stress drop,  $\Delta\tau_{ref}$ , and the scattering in the  $M_0 - A$  scaling plots is significantly reduced. While earthquake moment-area data can be alternatively interpreted as resulting from scale-dependency of stress drop (Dalguer et al. 2008), validation of this hypothesis has been challenging due to the large uncertainties of seismological estimates of stress drops. Here we will demonstrate that a model with constant stress drop is sufficient to explain the main characteristics of Stage 2.

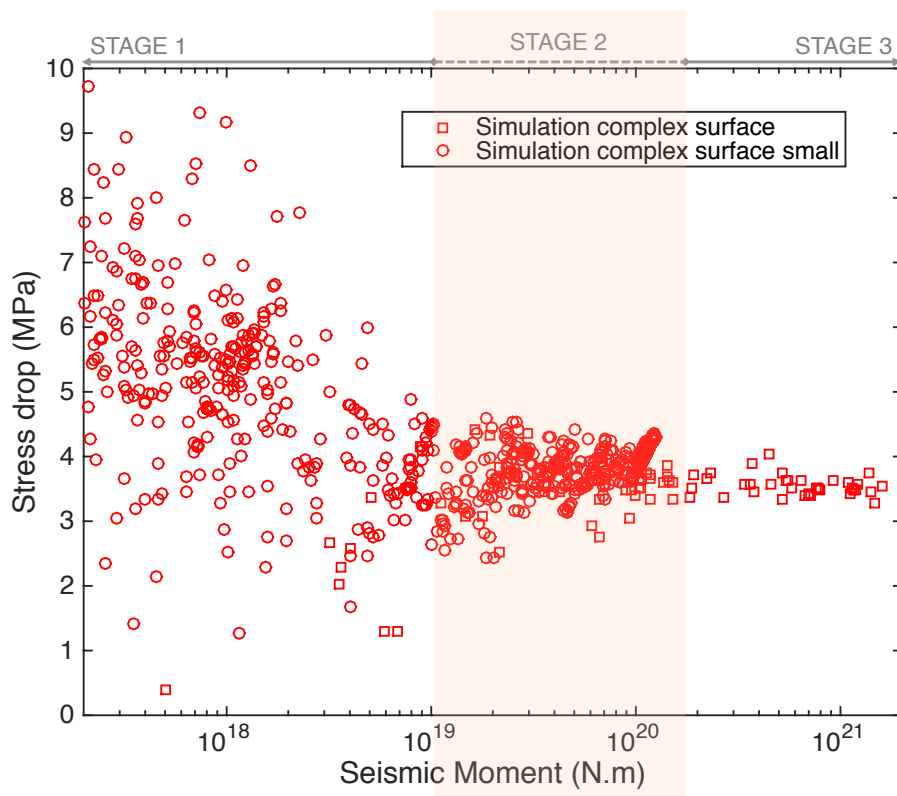


Figure 2.5: Stress drop as a function of seismic moment from rate-and-state simulations. Red circles and squares: synthetic earthquake data from rate-and-state simulation of “reduced-scale” and “full-scale” models, respectively. In stages 2 and 3 the variability of stress drop is small.

Two model parameters are calibrated to achieve a good match of the empirical  $M_0 - A$  relation: the seismogenic depth ( $W_s$ ) and the stress drop ( $\Delta\tau$ ). Dimensional analysis shows that, assuming the ratio  $L_c/W_s$  is fixed,  $A$  is proportional to  $W_s^2$  and  $M_0$  is proportional to  $\Delta\tau W_s^3$  (since  $M_0 = GAD \propto A\Delta\tau W_s \propto \Delta\tau W_s^3$ ). We can use this rationale to rescale our reference model results to obtain catalogs for different values of  $W_s$  and  $\Delta\tau$ . We first rescale the seismogenic depth: we multiply  $A$  by  $(W_s/W_{s\_ref})^2$  and  $M_0$  by  $(W_s/W_{s\_ref})^3$  where the seismogenic depth  $W_s$  is tuned to match as well as possible the range of  $M_0$  spanned by Stage 2 in the empirical model.

We then rescale the stress drop: we multiply  $M_0$  by  $\Delta\tau/\Delta\tau_{ref}$ , where the stress drop  $\Delta\tau$  is tuned to obtain the best overall match to the empirical model. The moment and rupture area data from our simulation catalog after these post-processing steps are shown in [Figure 2.1](#). The resulting  $M_0 - A$  scaling is in reasonable agreement with the 3-stage empirical relation. The events transit from small, self-similar ruptures to large, elongated ruptures ([Figure 2.4\(c\)](#)), and the  $M_0 - A$  scaling displays all the 3 stages. The best fitting model parameters have reasonable values:  $W_s = 20$  km and  $\Delta\tau = 2.4$  MPa. The best fitting seismogenic depth of our rate-and-state model is in the upper end of the typical range of seismogenic depths of real strike-slip faults. Penetration of rupture into the deep VS region is observed in the large events of our rate-and-state simulations (Stage 3), but remains modest, up to 2 km into the VS region (approximately 10% of seismogenic depth).

An additional set of simulations reveals the importance of the free surface in generating Stage 2. We ran earthquake cycle simulations on a pure velocity-weakening, deeply buried fault. Other settings are comparable to those of the simulations introduced above; the main difference is the absence of the free surface in the new set. The resulting catalog shows Stages 1 and 3, but no Stage 2 ([Figure 2.6](#)). In the next sections we develop a theoretical understanding of surface rupture effects on  $M_0 - A$  scaling relations.

### 2.3 Dislocation models

We first develop a dislocation model for which we can obtain an analytical expression of the  $M_0 - A$  relation in closed form, allowing fundamental insight into the problem. Dislocation models are rupture models with prescribed uniform slip and rupture geometry. The rupture shapes are assumed square for small events with rupture length  $L < W_s$  and rectangular for large events with  $L > W_s$  ([Figure 2.4\(a\)](#)). We consider two cases: (D1) without free surface and (D2) with free surface. The latter is achieved by mirroring the rupture with respect to the free surface.

From formulas for the stress changes induced by a rectangular dislocation in unbounded media ([Galović 2008](#)), we derive the following relation between average slip  $\bar{d}$  and stress drop  $\Delta\tau$  at the center of a dislocation of length  $L$  and width  $W$ :

$$\bar{d} = \frac{\pi\overline{\Delta\tau}}{2G} \cdot \frac{f\left(\frac{L}{2\xi W}, \nu\right)}{\sqrt{1/L^2 + 1/(2\xi W)^2}} \quad (2.1)$$

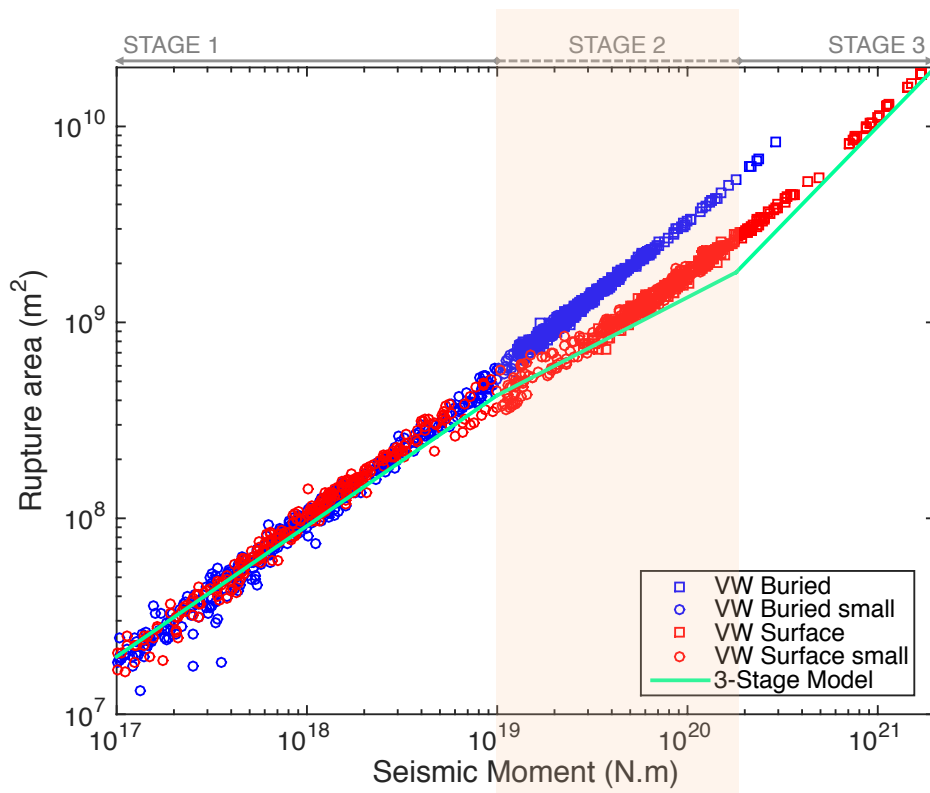


Figure 2.6: Effect of free surface on  $M_0 - A$  scaling. Red circles and squares: synthetic earthquake data from rate-and-state simulation with free surface in “reduced-scale” and “full-scale” models, respectively. blue circles and squares: synthetic earthquake data from rate-and-state simulation without free surface in “reduced-scale” and “full-scale” models, respectively. Green curve: empirical 3-Stage relation. The difference between the two rate-and-state models indicates that the free surface is key to Stage 2.

where

$$f(x, \nu) = \frac{x^2 + 1}{x^2 + 1/(1 - \nu)}$$

$\nu$  is Poisson’s ratio and  $\xi$  is a dimensionless parameter accounting for the free surface:  $\xi = 0.5$  for a deeply buried dislocation (D1) and  $\xi = 1$  for a vertical strike-slip dislocation breaking the free surface (D2). The seismic moment is

$$M_0 = GA\bar{d} \quad (2.2)$$

For ruptures smaller than the seismogenic depth  $W_s$  we assume self-similarity,  $L = W$ , and the rupture area is  $A = L^2$ . For longer ruptures that saturate the

<b>Physical properties</b>	<b>Value</b>
Total fault depth	30 km
Reference seismogenic depth	About 18 km
Total fault length	64 km / 512 km ("Reduced-scale" / "Full-scale" fault)
Fault dipping	90°(vertical strike-slip)
Effective normal stress	0-75 MPa (saturated at 10 km)
Lamé's first parameter	30 GPa
Lamé's second parameter (Shear modulus)	30 GPa
Shear wave velocity	3000 m/s
Frictional coefficient $a$ (Direct effect)	0.01
Frictional coefficient $b$ (Indirect effect)	0.015 (VW) / 0.006 (VS)
Characteristic slip distance $D_c$	Lognormal distribution 0.01 m to 0.15 m
$D_c$ correlation length $L_{co}$	1 to 10 km
Reference friction coefficient	0.6
Grid size	125 m / 250 m ("Reduced-scale" / "Full-scale" fault)
<b>Post-processing parameters</b>	<b>Value</b>
Event detecting threshold	Global max slip rate of 0.01 m/s
Event separating threshold	10 minutes between events
Best fitting stress drop	2.4 MPa
Best fitting seismogenic depth	20 km

Table 2.1: Typical parametric settings of rate-and-state simulation.

seismogenic depth,  $L > W = W_s$  and  $A = LW_s$ . Combining Equations 2.1 and 2.2 gives in these two cases:

$$M_0 = L^3 \cdot \frac{\pi \overline{\Delta\tau}}{2} \cdot \frac{f\left(\frac{1}{2\xi}, \nu\right)}{\sqrt{1 + \left(\frac{1}{2\xi}\right)^2}} \quad L \leq W_s \quad (2.3a)$$

$$M_0 = LW_s \cdot \frac{\pi \overline{\Delta\tau}}{2} \cdot \frac{f\left(\frac{L}{2\xi W_s}, \nu\right)}{\sqrt{\left(\frac{1}{L}\right)^2 + \left(\frac{1}{2\xi W_s}\right)^2}} \quad L > W_s \quad (2.3b)$$

From this we derive the following moment-area relations:

$$M_0 = A^{3/2} \cdot \frac{\pi \overline{\Delta\tau}}{2} \cdot \frac{f\left(\frac{1}{2\xi}, \nu\right)}{\sqrt{1 + \left(\frac{1}{2\xi}\right)^2}} \quad L \leq W_s \quad (2.4a)$$

$$M_0 = A \cdot \frac{\pi \overline{\Delta\tau}}{2} \cdot \frac{f\left(\frac{A}{2\xi W_s^2}, \nu\right)}{\sqrt{\left(\frac{W_s}{A}\right)^2 + \left(\frac{1}{2\xi W_s}\right)^2}} \quad L > W_s \quad (2.4b)$$

Equation 2.4a shows that the dislocation model reproduces the  $M_0 \sim A^{3/2}$  scaling of Stage 1 when  $L < W_s$ . By considering the asymptotic behavior of Equation 2.4b we find that the dislocation model also reproduces the  $M_0 \sim A$  scaling of Stage 3 when  $L \gg W_s$ . The resulting  $M_0 - A$  curves, shown in [Figure 2.2](#) (assuming  $W_s = 20$  km,  $\Delta\tau = 3$  MPa for model D1 and  $\Delta\tau = 1.5$  MPa for model D2), confirm that both models have Stages 1 and 3. However, only model D2 has a noticeable Stage 2, which appears in [Figure 2.2](#) as an intermediate regime with lower slope than Stages 1 and 3. This confirms our previous conclusion that the free surface is essential for Stage 2.

In model D2, because of our simplified use of the mirror image method, the stress drop is actually evaluated at the surface rather than at mid-rupture depth. Evaluating it at a mid-depth yields a more complicated formula and a  $M_0 - A$  relation in between models D1 and D2.

An asymptotic argument provides insight on the role of the free surface. By extrapolating equation 2.4b towards  $L \ll W_s$  ( $A \ll W_s^2$ ), essentially considering ruptures that are elongated in the vertical direction, yields:

$$M_0 = \frac{A^2}{W_s} \cdot \frac{\pi \overline{\Delta\tau}}{2} \cdot (1 - \nu) \quad (2.5)$$

This is a  $M_0 \sim A^2$  relation like the proposed Stage 2. Hence, the dislocation model reveals an underlying asymptotic tendency towards Stage 2 due to vertical elongation of the rupture. The vertical elongation is not necessarily real: an effective elongation may result from the free surface effect. In an infinite space model, the free surface can be mimicked by a mirror image rupture. The effective rupture (the combination of real and image ruptures) is elongated vertically up to an aspect ratio of 2. This is a geometrical effect of the free surface, which we denote as the "G effect".

Our rate-and state simulations reveal an additional "surface attraction effect" that enhances the G effect. The shallow VS zone discourages small events from breaking the surface. Ruptures that grow to a certain size (still smaller than  $W_s$ ) penetrate the shallow VS barrier and may break the free surface. Considering the free surface as a mirror, the real and image ruptures are two interacting coplanar cracks. The stress increase beyond their tips enhances their propagation, they attract each other and coalesce. This attractor effect can extend the vertical elongation beyond aspect ratio of 2, thus further enhancing the "G effect" (Figure 2.4(c)).

The dislocation model D2 agrees qualitatively with our rate-and-state model (Figure 2.7). However, it cannot fit the empirical Stages 1 and 3 simultaneously: the width of Stage 2 is narrower than in the empirical model. This limitation of dislocation models motivates our next improvement of the theory.

## 2.4 Crack models

We now consider crack models, i.e. models in which stress drop is prescribed within a given rupture area. There is no simple analytical  $M_0 - A$  expression for a crack of general shape and including the free surface, so we compute it numerically. The spatial distributions of slip and stress drop, discretized over a fault grid, are related by a linear system of equations whose coefficients can be computed with formulas by (Okada 1992). We prescribe a rupture geometry and uniform stress drop ( $\Delta\tau$ ), and solve the system of equations to obtain the slip distribution. We then compute the average slip  $\bar{d}$  and the "geometrical shape factor"  $C$  defined by

$$C = \Delta\tau \min(L, W_s)/G\bar{d} \quad (2.6)$$

$C$  is a non-dimensional function of  $L/W_s$ . Knowing  $C$  we can calculate  $M_0$  of any given event using

$$M_0 = GA\bar{d} = \Delta\tau \min(L, W_s)A/C \quad (2.7)$$

We solved crack models ranging from small circular ruptures (100 m in diameter) to horizontally elongated ruptures (up to 600 km in length). The latter have semi-circular lobes on both lateral ends (Figure 2.4(b)) to ensure a smooth shape transition from circular to elongated ruptures. We have considered other shapes of crack models but the presented model offers the best fit to data.

The  $M_0 - A$  curve resulting from the crack model is shown in gray in Figure 2.7. This model also reproduces the 3 stages. Overall, it fits better the empirical relation than our dislocation models: it can fit Stages 1 and 3 simultaneously and has a reasonable range of Stage 2. The crack model also agrees well with our rate-and-state model.

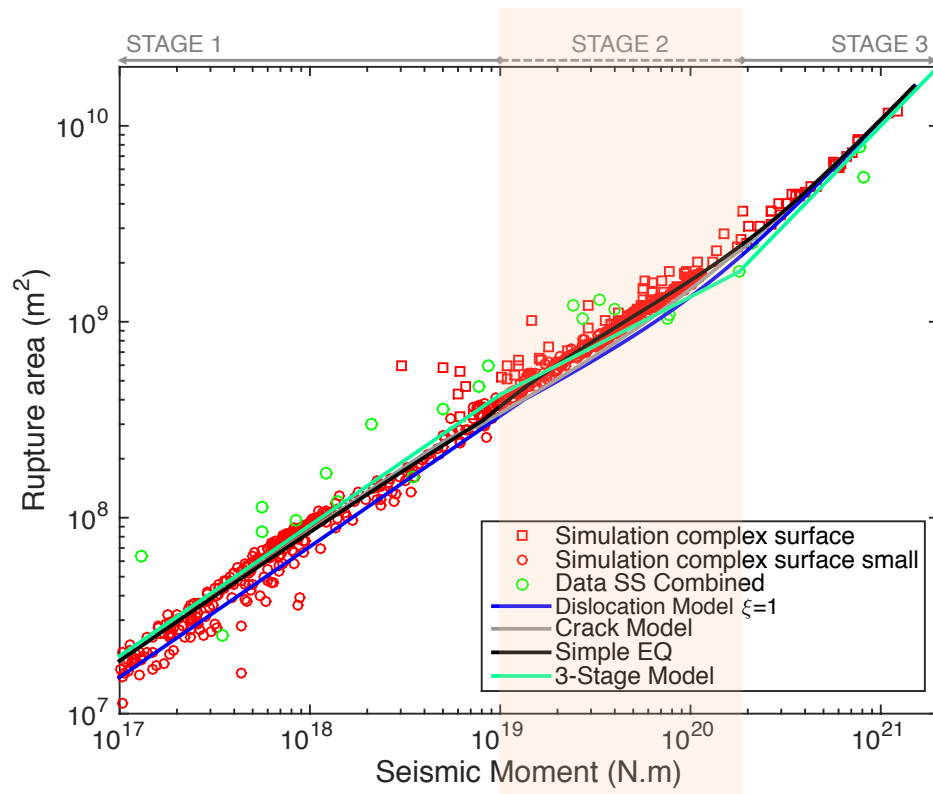


Figure 2.7: Earthquake  $M_0 - A$  scaling in empirical data, synthetic catalogs and theoretical models. Green circles: strike-slip earthquake data. Green curve: empirical 3-stage relation. Red circles and squares: synthetic earthquake data from earthquake cycle simulations of "reduced-scale" and "full-scale" models, respectively. Dark blue curve: dislocation model with free surface (Model D1). gray curve: crack model. Black curve: proposed simple equation 2.8 with best fitting parameters  $p = 2.08$  and  $\lambda = 1.93$ . The crack model fits the data better than the dislocation model, and the simple equation 2.8 fits both the simulation and observation data extremely well.

Our crack model reveals an additional mechanism contributing to Stage 2: the change of shape factor  $C$  due to the free surface, which we refer to as "C effect" hereafter (Figure 2.8). When a rupture grows towards the free surface ( $L/W_s$  increases and approaches 1 in Figure 2.8),  $C$  decreases rapidly by approximately a factor of 2. The  $C$  values of a deep buried circular crack and an infinitely long strike-slip rupture that reaches the surface are  $C_0 = 7\pi/8$  and  $C_1 = 2/\pi$ , respectively (Kanamori and

Anderson 1975), which differ by a factor of about 4. Equation 2.7 shows that the decrease of  $C$  pushes Stage 3 "to the right" in the  $M_0 - A$  plot (larger moment for a given area). This effectively increases the apparent value of the scaling exponent  $n$  and extends the range of Stage 2. In nature, the  $C$  effect always occurs together with the  $G$  effect and both contribute to Stage 2. Thus the transition between small buried ruptures and large surface-breaking ruptures is the major origin of Stage 2. The combination of  $C$  effect and  $G$  effect, that we name "surface rupture effect", are sufficient to explain the observed Stage 2 in both real world earthquakes and simulated earthquakes.

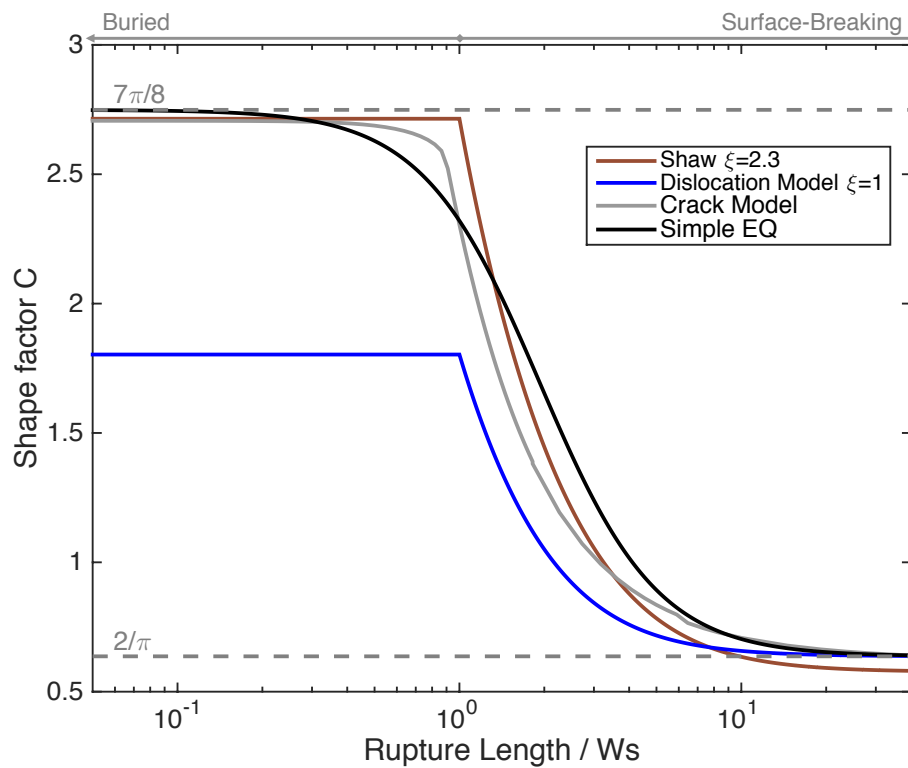


Figure 2.8: Shape factor  $C$  of different models as a function of rupture length  $L$  normalized by seismogenic depth  $W_s$ . Brown curve: Shaw's deep penetration model. blue curve: dislocation model with free surface (model D2). gray curve: crack model with free surface. Black curve: our proposed simple equation 2.8 with best fitting parameters  $p = 2.08$  and  $\lambda = 1.93$ . The theoretical values of an infinitely long strike-slip rupture and a deep buried circular crack are  $2/\pi$  and  $7\pi/8$ , respectively.

Our crack model fits quantitatively well with both empirical and simulation  $M_0 - A$  data. However, there is no analytical expression for crack models. Here we propose

a simplified equation in closed form for the shape factor  $C$  that can be useful for practical purposes. (Figure 2.8)

$$C\left(\frac{L}{W_s}\right) = C_0 + \frac{C_1 - C_0}{1 + (\lambda W_s/L)^p} \quad (2.8)$$

This equation has the following controlling parameters: the seismogenic depth  $W_s$  (or, in more general terms, the maximum rupture width) and two tunable variables  $p$  and  $\lambda$ . Similar to equations 2.4a,2.4b we get the following general forms of the  $M_0 - A$  relation

$$M_0 = A^{3/2} \cdot \frac{\overline{\Delta\tau}}{C} \quad L \leq W_s \quad (2.9a)$$

$$M_0 = A \cdot W_s \cdot \frac{\overline{\Delta\tau}}{C} \quad L > W_s \quad (2.9b)$$

We performed a grid search to find the values of parameters  $p$  and  $\lambda$  that minimize the least squares misfit between the moment – area data from rate-and-state simulations (smoothed by a sliding median) and predicted by combining equations 2.8 and 2.9a,2.9b. We find that the best fitting values and their 95% confidence intervals are  $p = 2.08 \pm 0.2$  and  $\lambda = 1.93 \pm 0.1$  (Figure 2.9).

Combining equations 2.8 and 2.9a,2.9b gives a convenient and reasonably accurate relation between seismic moments and rupture area across all earthquake magnitudes. The  $M_0 - A$  relation resulting from equation 2.8 with the best fitting parameter values  $p$  and  $\lambda$  is presented in black in Figure 2.7. It is in very good agreement with both rate-and-state simulation results and the earthquake data and is noticeably better than the original crack model, especially in Stage 2. Plotting  $M_0$  versus  $A/M_0^{2/3}$  (Figure 2.10) allows a more critical assessment of the agreement between equation 2.8 and the synthetic rate-and-state catalog.

Equation 2.8 is simple and has a clear physical meaning. Its asymptotic limits,  $C_0$  and  $C_1$ , are consistent with values from well-accepted crack models. The value of  $\lambda$  is expected to be 2 from the free surface effect in the absence of deep rupture penetration, and the best fitting value  $\lambda = 1.93$  indicates that no deep penetration is required by our model. In comparison, fitting our rate-and-state catalog with Shaw's model requires rupture to extend much deeper, 200% of the seismogenic depth. Most importantly, our physically sound model fits very well the real earthquake data, so

it can be used as a simple yet accurate moment-area scaling model. Adopting the values  $p = 2$  and  $\lambda = 2$ , within the 95% confidence level of the best fitting values, we propose the following simple equation for use in practical applications:

$$C\left(\frac{L}{W_s}\right) = \frac{\pi}{8} \left( 7 - \frac{3}{1 + (2W_s/L)^2} \right) \quad (2.10)$$

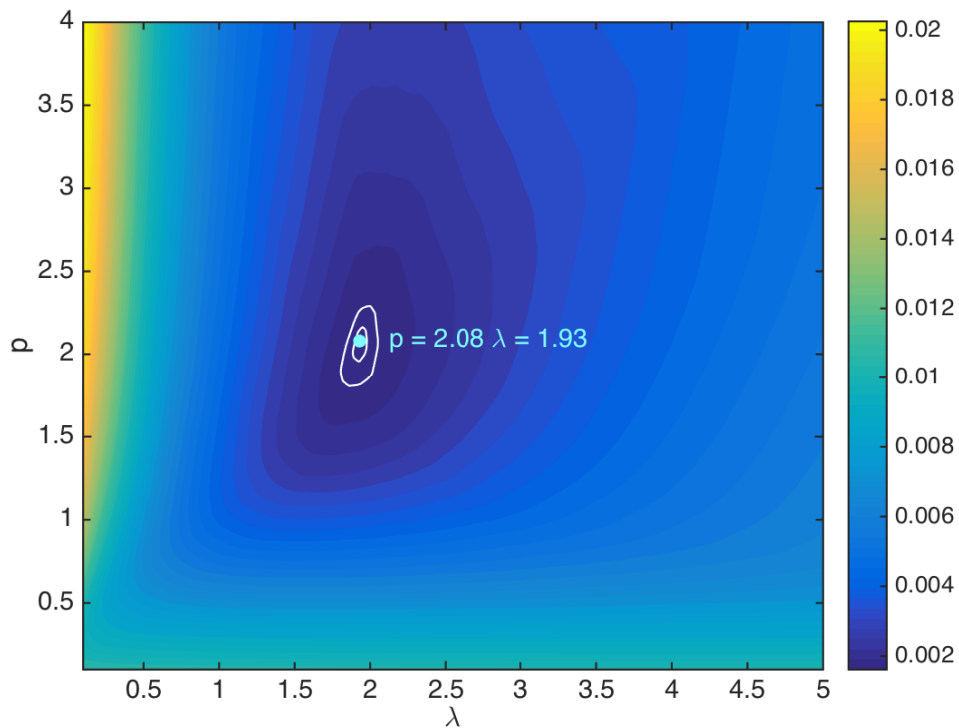


Figure 2.9: Misfit between moment-area data from our rate-and-state catalog and our equation 2.8 as a function of  $\lambda$  and  $p$ . The best fitting values are  $p = 2.08$  and  $\lambda = 1.93$  (light blue dot). White contours are the 95% and 99% confidence levels.

## 2.5 Conclusions

We investigated the mechanical origin of the transition in earthquake moment-area scaling between the small (self-similar) and very large (W-model) earthquake scaling regimes via rate-and-state earthquake cycle simulations, analytical dislocation models and numerical crack models on strike-slip faults. We demonstrated that the counter-intuitive form of the transitional Stage 2 ( $M_0 \sim A^2$ ) can be mainly attributed to surface rupture effects, comprising an effective rupture elongation along-dip due to a mirror effect (G effect) and systematic changes of the shape factor relating slip to stress drop (C effect). Other effects, like deep rupture penetration, deeper viscous

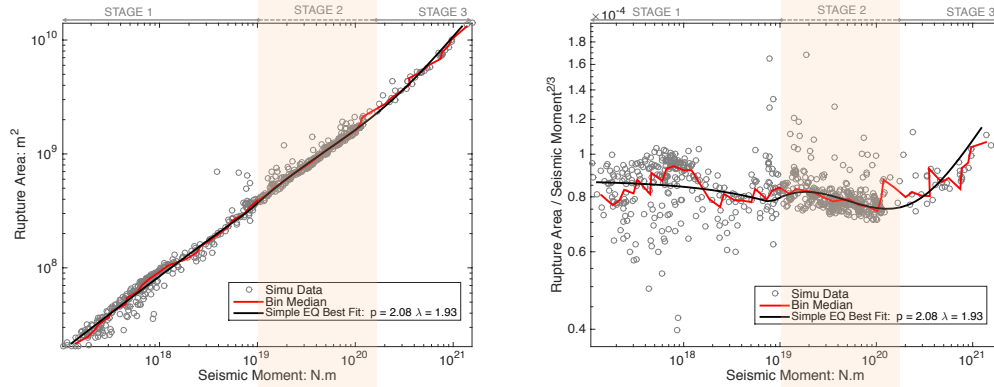


Figure 2.10: Left: earthquake  $M_0 - A$  scaling in synthetic catalogs and best fitting simple practical model. Right: reduced  $M_0 - A/M_0^{2/3}$  scaling, which allows a more critical assessment of the agreement between equation 2.8 and the synthetic rate-and-state catalog. Gray circles: synthetic earthquake data from our rate-and-state simulation. Red curve: sliding median of synthetic data. Black curve: proposed simple equation 2.8 with best fitting parameters  $p = 2.08$  and  $\lambda = 1.93$ . The proposed equation is in good agreement with the synthetic data.

layer and scale-dependency of stress drop, while possibly present and contributing to the origin of the 3-stage model, should be considered as secondary. Based on this physical insight, we proposed a physically sound approximate formula that conveniently relates seismic moment and rupture size across all earthquake magnitudes, and can be of practical use in earthquake hazard assessment and ground motion prediction. The parameters of our rate-and-state model (seismogenic depth and stress drop) and of our simplified equation are calibrated to fit the empirical 3-stage model. While our models require a seismogenic depth of 20 km, in the upper end of typical values for strike-slip faults, including additional mechanisms like scale-dependency of stress drop might allow us to fit the real earthquake data with a smaller seismogenic depth.

**Acknowledgements:** This study was based on the 2015 research project "Improvement for uncertainty of strong ground motion prediction" by the Nuclear Regulation Authority (NRA), Japan.

## References

- Bodin, P. and J. N. Brune (1996), “On the scaling of slip with rupture length for shallow strike-slip earthquakes: Quasi-static models and dynamic rupture propagation”. *Bulletin of the Seismological Society of America*, 86 (5), pp. 1292–1299.
- Causse, M. and S. G. Song (2015), “Are stress drop and rupture velocity of earthquakes independent? Insight from observed ground motion variability”. *Geophysical Research Letters*, 42 (18), pp. 7383–7389.
- Dalguer, L. A., H. Miyake, S. M. Day, and K. Irikura (2008), “Surface rupturing and buried dynamic-rupture models calibrated with statistical observations of past earthquakes”. *Bulletin of the Seismological Society of America*, 98 (3), pp. 1147–1161.
- Fujii, Y. and M. Matsu’ura (2000), “Regional difference in scaling laws for large earthquakes and its tectonic implication”. *Pure and Applied Geophysics*, 157 (11), pp. 2283–2301.
- Gallovič, F. (2008), “Heterogeneous Coulomb stress perturbation during earthquake cycles in a 3D rate-and-state fault model”. *Geophysical Research Letters*, 35 (21).
- Hanks, T. C. and W. H. Bakun (2002), “A bilinear source-scaling model for M-log A observations of continental earthquakes”. *Bulletin of the Seismological Society of America*, 92 (5), pp. 1841–1846.
- (2014), “M–logA Models and Other Curiosities”. *Bulletin of the Seismological Society of America*, 104 (5), pp. 2604–2610.
- Hillers, G., Y. Ben-Zion, and P. M. Mai (2006), “Seismicity on a fault controlled by rate-and state-dependent friction with spatial variations of the critical slip distance”. *Journal of Geophysical Research: Solid Earth*, 111 (B1).
- Hillers, G., P. M. Mai, Y. Ben-Zion, and J. P. Ampuero (2007), “Statistical properties of seismicity of fault zones at different evolutionary stages”. *Geophysical Journal International*, 169 (2), pp. 515–533.
- Irikura, K. and H. Miyake (2001), “Prediction of strong ground motions for scenario earthquakes”. *Journal of Geography (Chigaku Zasshi)*, 110 (6), pp. 849–875.
- (2011), “Recipe for predicting strong ground motion from crustal earthquake scenarios”. *Pure and Applied Geophysics*, 168 (1-2), pp. 85–104.
- Kanamori, H. and D. L. Anderson (1975), “Theoretical basis of some empirical relations in seismology”. *Bulletin of the seismological society of America*, 65 (5), pp. 1073–1095.
- Leonard, M. (2010), “Earthquake fault scaling: Self-consistent relating of rupture length, width, average displacement, and moment release”. *Bulletin of the Seismological Society of America*, 100 (5A), pp. 1971–1988.

- Luo, Y., J. P. Ampuero, P. Galvez, M. Ende, and B. Idini (2017), *QDYN: a Quasi-DYNamic earthquake simulator (v1.1)*. DOI: 10.5281/zenodo.322459. URL: <https://doi.org/10.5281/zenodo.322459>.
- Mai, P. M. and G. C. Beroza (2000), “Source scaling properties from finite-fault-rupture models”. *Bulletin of the Seismological Society of America*, 90 (3), pp. 604–615.
- Marone, C. (1998), “Laboratory-derived friction laws and their application to seismic faulting”. *Annual Review of Earth and Planetary Sciences*, 26 (1), pp. 643–696.
- Matsu’ura, M. and T. Sato (1997), “Loading mechanism and scaling relations of large interplate earthquakes”. *Tectonophysics*, 277 (1), pp. 189–198.
- Miyakoshi, K., K. Irikura, and K. Kamae (2015), “Re-examination of scaling relationships of source parameters of the inland crustal earthquakes in Japan based on the waveform inversion of strong motion data”. *Journal of Japan Association for Earthquake Engineering*, 15 (7), pp. 141–156.
- Murotani, S., S. Matsushima, T. Azuma, K. Irikura, and S. Kitagawa (2015), “Scaling relations of source parameters of earthquakes occurring on inland crustal megafault systems”. *Pure and Applied Geophysics*, 172 (5), pp. 1371–1381.
- Okada, Y. (1992), “Internal deformation due to shear and tensile faults in a half-space”. *Bulletin of the Seismological Society of America*, 82 (2), pp. 1018–1040.
- Romanowicz, B. and J. B. Rundle (1993), “On scaling relations for large earthquakes”. *Bulletin of the Seismological Society of America*, 83 (4), pp. 1294–1297.
- Rubin, A. M. and J. P. Ampuero (2005), “Earthquake nucleation on (aging) rate and state faults”. *Journal of Geophysical Research: Solid Earth*, 110 (B11).
- Scholz, C. H. (1982), “Scaling laws for large earthquakes: consequences for physical models”. *Bulletin of the Seismological Society of America*, 72 (1), pp. 1–14.
- (1998), “Earthquakes and friction laws”. *Nature*, 391 (6662), p. 37.
- Shaw, B. E. (2009), “Constant stress drop from small to great earthquakes in magnitude-area scaling”. *Bulletin of the Seismological Society of America*, 99 (2A), pp. 871–875.
- Shaw, B. E. and S. G. Wesnousky (2008), “Slip-length scaling in large earthquakes: The role of deep-penetrating slip below the seismogenic layer”. *Bulletin of the Seismological Society of America*, 98 (4), pp. 1633–1641.
- Somerville, P. et al. (1999), “Characterizing crustal earthquake slip models for the prediction of strong ground motion”. *Seismological Research Letters*, 70 (1), pp. 59–80.
- Song, S. G., G. C. Beroza, and P. Segall (2008), “A unified source model for the 1906 San Francisco earthquake”. *Bulletin of the Seismological Society of America*, 98 (2), pp. 823–831.

- Streit, J. E. and S. F. Cox (2001), “Fluid pressures at hypocenters of moderate to large earthquakes”. *Journal of Geophysical Research: Solid Earth*, 106 (B2), pp. 2235–2243.
- Wells, D. L. and K. J. Coppersmith (1994), “New empirical relationships among magnitude, rupture length, rupture width, rupture area, and surface displacement”. *Bulletin of the seismological Society of America*, 84 (4), pp. 974–1002.

*Chapter 3***STABILITY AND EFFECTIVE FRICTION OF FAULTS WITH  
HETEROGENEOUS FRICTION PROPERTIES AND FLUID  
PRESSURE****Abstract**

Abundant geological, seismological and experimental evidence of the heterogeneous structure of natural faults motivates the theoretical and computational study of the mechanical behavior of heterogeneous frictional interfaces. Fault zones are composed of a mixture of competent and incompetent materials with contrasting strength, which may affect the spatial variability of seismic coupling and high-frequency radiation as well as the diversity of slip behavior observed in natural faults. To develop a quantitative understanding of the effect of strength heterogeneity on the mechanical behavior of faults, here we investigate a fault model with spatially variable frictional properties and pore pressure. Conceptually, this model corresponds for instance to two rough surfaces in contact along discrete asperities, the space in between being filled by compressed gouge. The asperities have different permeability than the gouge matrix, resulting in different pore pressure. We systematically study the diversity of slip behaviors generated by this model through multi-cycle simulations of faults governed by rate-and-state friction and linear stability analysis. Our study reveals that the fault can be either stable without spontaneous slip transients, or unstable with spontaneous rupture. When fault is unstable, slip can rupture part or the entire fault. In some cases we find a combination of these behaviors throughout multiple cycles. We explore how the overall fault behavior is controlled by the proportions of competent and incompetent materials, their relative strength and other frictional properties. We also develop, through heuristic approximations, closed-form equations to predict the stability of slip on heterogeneous faults. Our study shows that a fault model with competent-incompetent material mixture and pore pressure contrasts is a viable framework to reproduce the full spectrum of fault behaviors observed in natural faults: from fast earthquakes, to slow transients, to stable sliding. In particular, this model constitutes a building block for models of episodic tremor and slow slip events.

### 3.1 Introduction

#### Geological and physical background

The spectrum of earthquake phenomena has been greatly expanded by the discovery in the past decade of a family of slow earthquake processes including tectonic tremors (also known as non-volcanic tremors), low frequency earthquakes (LFE), very low frequency earthquakes (VLFE) and slow-slip events (SSE) (Ide et al. 2007). These seismic and aseismic events often occur together, for instance recurrent SSE are often accompanied by tremors, a phenomenon known in Cascadia as “episodic tremor and slow-slip events” (ETS). These slow earthquake phenomena mostly occur in the deep seismic-aseismic transition region of faults, or in the shallow accretionary prism of subduction zones. For instance, in the Cascadia subduction zone, ETS are located below the seismogenic depth limit determined by thermal modeling. In most cases, the transition from fast to slow, to stable slip behavior as a function of depth is gradual. With increasing depth, the inter-event time between episodic slow events (ETS and episodic tremors) and their duration decrease gradually. The amount of background (non-episodic, continuous) tremors increases with depth, and eventually transits into continuous steady slip (Wech and Creager 2011).

Regular earthquakes (i.e. earthquakes with rupture speed comparable to wave speeds) may also feature intermingled slow and fast rupture processes. Teleseismic back-projection source imaging of the 2011 Tohoku-Oki earthquake revealed a period of relatively slow rupture in the down-dip direction (Meng et al. 2011). This slow stage of the rupture was interspersed by strong high-frequency radiation bursts. The frequency content of this deeper part of the rupture, near the bottom of the seismogenic zone, was richer in high frequencies than the shallower part. This depth-dependent frequency content of the source has been observed in other megathrust events, including the 2015 Gorkha, Nepal earthquake (Avouac et al. 2015; Lay et al. 2012).

These gradual transitions and coexistence of fast to slow earthquake slip behaviors in different environments suggest common mechanisms behind the full spectrum of earthquakes. Yet there is currently no model that can conceptually unify and quantitatively reproduce such a large span of phenomena. This gap in our understanding of the mechanics of fast and slow earthquakes has encouraged us to search for viable physical models, and the present work is a building block in that effort.

Geological field observations show heterogeneity of fault materials over a broad range of length scales. Exhumed subduction fault zones show a pattern of block-in-

matrix mélange, with competent lenses embedded in a incompetent matrix, at scales ranging from millimeters to tens of meters (Bebout and Barton 2002; Fagereng 2011; Fagereng and Cooper 2010; Fagereng and Sibson 2010; Meneghini et al. 2010). Laboratory experiments indicate that heterogeneity can affect the mechanical response of a fault. Kocharyan et al. (2016) found in laboratory experiments that the stress drop of slip transients depends on the proportion of materials mixed in a composite gouge. Ma and He (2001) found period doubling phenomena in experiments with two segments of competent and incompetent materials along a frictional surface. Thus, fault heterogeneity involving contrasts of material competence is a potentially important ingredient to model rich fault slip behaviors.

Geological observations also show evidence of spatial and temporal variability of pore fluid pressure across various scales in fault zones. This contributes to fault heterogeneity and can affect the fault slip behavior. Mechanisms such as hydraulic fracturing and cracking (Luo and Vasseur 2002), and pore-space reduction by solution and cementation (Rittenhouse 1971) change the permeability of fault materials and affect the pore pressure and hence frictional strength. The formation of fluid seals in a fault zone causes high pore pressures if the sealed material compacts or produces more fluids. Excess pressure can then be released by rupture of the seals, over the long time scales of plate subduction, or recur with fault-valve behavior over the time periods between earthquakes (Hillers and Miller 2007; Sibson 1992, 2014; Sibson et al. 1988). Also, various direct and indirect evidences show localized changes in pore pressure. Healy et al. (1968) and a body of subsequent work studies seismicity changes due to changes of pore pressure. Thermal expansion of pore fluids, e.g. via shear heating, in media with heterogeneous permeability can create highly localized pore pressure contrasts (Osborne and Swarbrick 1997). Roberts and Nunn (1995) found that fluid transport results in localized pore pressure changes on various time scales. Fagereng and den Hartog (2017) studied pressure solution at seismogenic depths and found that more soluble elements dissolve first, which causes porosity and pore pressure differences between competent and incompetent fault materials at fine length scales of material heterogeneity.

Other fault properties can also be heterogeneous. Hillers et al. (2006, 2007) and Perfettini et al. (2003) studied the effect of heterogeneity of the characteristic slip distance  $D_c$  of the evolution of friction (see definition in section 3.2). Luo et al. (2017b) also considered a fault with heterogeneous  $D_c$  to model earthquakes with a wide range of magnitudes for a study of earthquake scaling relations. Marone

and Kilgore (1993) found, in laboratory experiments, a scaling between  $D_c$  and the thickness of the gouge layer, a fault zone property that shows variability along natural faults. Scuderi and Collettini (2016) found that  $D_c$  is positively related to normal stress, which can also be variable along a fault. Parsons (2005) hypothesized that changes of  $D_c$  could help explain dynamic triggering.

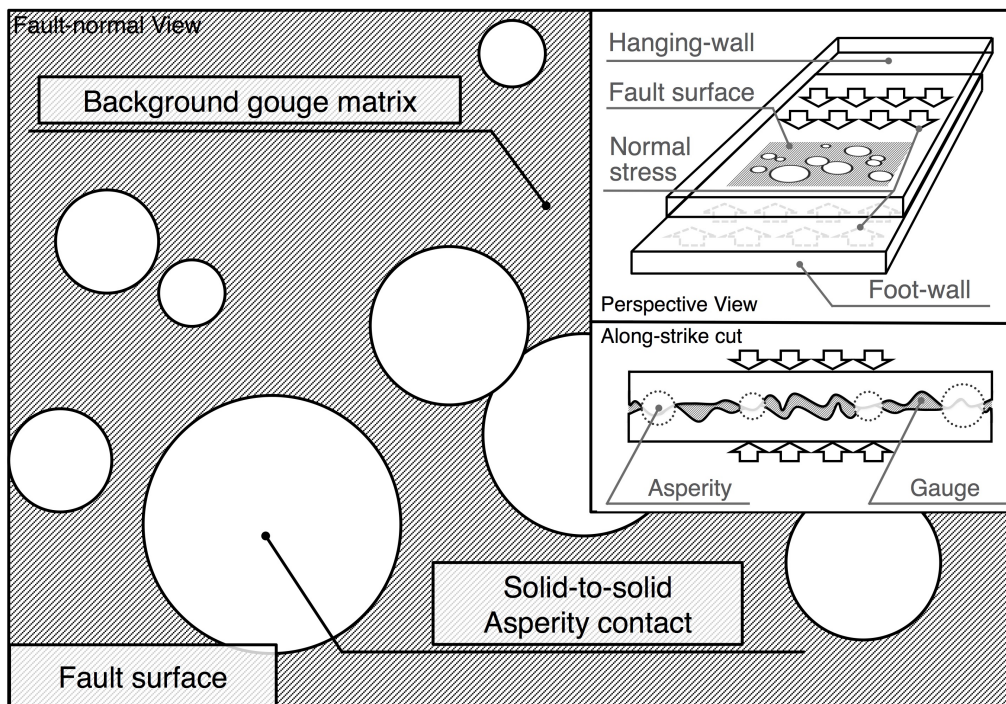


Figure 3.1: Sketch of conceptual model, where asperities make solid-to-solid contact at fault surface and surrounded by a gouge matrix which can have different compressibility and permeability

Here, we develop a conceptual model consistent with the foregoing picture of heterogeneous faults of contrasting material competence. Our modeling framework is generally applicable to faults with variable strength and pore pressure, regardless of how those heterogeneities emerged. However, it may be useful to illustrate the model through one specific situation. Consider a fault zone composed of two rough surfaces in contact and gouge or sediments in between. When the two fault surfaces are pressed together by the increasing confining stresses during subduction, the rough surfaces make contact at discrete "asperities" and the intervening gouge matrix is compressed. In the case of asperity contacts have different compressibility and permeability than the gouge matrix and are prone to hydraulic sealing (Figure

3.1). Influx of fluids, e.g. due to dehydration, can change the pore pressure in the gouge but not in the sealed asperities. This results in differences of effective normal stress between asperities and the gouge matrix.

### **Background on fault stability**

In theoretical and computational models, a fault can display a wide range of slip behaviors. We refer to a fault as "stable" if it slips steadily when driven by a steady loading. If instead the fault generates spontaneous slip transients, we qualify it as "unstable". On unstable faults, slip transients range from quasi-static (aseismic, such as SSE) to dynamic (seismic, such as regular earthquakes). The distinction between aseismic and seismic slip transients is based on radiation efficiency, i.e. the ratio of radiated energy to the sum of radiated and fracture energies. The radiation efficiency of an earthquake or any propagating slip transient is primarily controlled by its rupture speed (Venkataraman and Kanamori 2004). The stability of a fault depends on its frictional properties, state of stress and boundary conditions, as will be explained in detail in section 3.2 within the framework of rate-and-state friction. The propensity to stability of a rate-and-state material depends strongly on whether its steady-state friction coefficient is velocity-weakening (VW) or velocity-strengthening (VS). A VW material can be unstable and will represent here a competent fault zone material, whereas a VS material tends to be stable.

Our study extends previous theoretical and computational work on the stability of faults governed by rate-and-state friction with an alternation of VW and VS materials along the fault. Skarbek et al. (2012) studied fault stability with various ratios of VW to VS material content. They found that, with other parameters fixed, the relative portion of the VW and VS materials controls the stability of slip. They focused on instabilities that involve rapid slip over the whole fault, which we will refer to as "Total instabilities" or "T-instabilities". They found the critical VW/VS area ratio required for instability in numerical simulations is accurately predicted by linear stability analysis (LSA). Dublanchet et al. (2013) introduced the concept of a critical (minimum) density of VW asperities required for instability. Their results are consistent with those of Skarbek et al. (2012). Yabe and Ide (2017) reported an additional instability that involves rapid slip mainly in the VW segments, and possibly minor slip extending to the VS material in their immediate vicinity, which we will refer to as "Partial instability" or "P-instability". The existence of P-instabilities is not unexpected: it is known that an isolated VW fault is unstable if its size exceeds a critical length (Chen and Lapusta 2009; Rubin and Ampuero 2005,

see also section 3.2). Yabe and Ide (2017) argued that the P-instability occurs when the size of the VW segment exceeds the critical size for instability on a homogeneous VW fault. We will show in section 3.2 that such argument, while adequate to first-order, is incomplete: the P-instability is affected by the surrounding VS material as well. They also found that, if the loading stiffness is very low, the T-instability occurs only if the fault is velocity neutral on average (average  $a - b = 0$ ). This condition can be derived as a special case of the theoretical results by Skarbek et al. (2012). Viesca (2016) further studied the evolution of slip rate during the nucleation of frictional instabilities on heterogeneous faults.

### Goals and scope

In this study, we focus on the following two questions about faults with mixture of competent/incompetent materials and pore pressure contrasts, within the framework of rate-and-state faults with alternating VS and VW properties:

1. Under what conditions is the fault stable or unstable?
2. Does unstable slip span the whole fault or only part of it?

In particular, our study includes an investigation on the effect of heterogeneous characteristic slip distance  $D_c$ , fault width  $W$ , and effective normal stress contrast between the VW and VS materials, which have not been considered in previous studies. Allowing variations of pore pressure and  $D_c$  unveils unexpected characteristics of instabilities that are of theoretical and practical significance.

In section 3.2, we introduce the model and study numerically its stability as a function of the proportion of VW and VS materials, their relative strength and the degree of intrinsic instability of the VW asperity. In section 3.3, we utilize analytical tools of linear stability analysis (LSA) to study the stability of a simplified two-degree-of-freedom spring-block model. The results are in good agreement with the instability conditions found numerically in section 3.2. The role of other model parameters is then explored via LSA. In section 3.4, we develop compact formulas in closed form which accurately predict the instability conditions based on heuristic approximations of the LSA results. Finally, in section 3.5, we discuss implications of our results and conclude.

### 3.2 Rate-and-state models

#### Model definition

We adopt the classical rate-and-state friction law motivated by laboratory experiments at low slip rate (Dieterich 1979; Marone 1998; Ruina 1983). This friction law has shown its modeling capacity from laboratory scales to natural earthquake scales (Ampuero and Rubin 2008). The rate-and-state framework assumes that the fault is always slipping and hence the shear stress  $\tau$  is always equal to the frictional strength,  $\tau = \mu\sigma$ , where  $\sigma$  is the effective normal stress (normal stress minus pore fluid pressure). The friction coefficient  $\mu(V, \theta)$  depends on slip velocity  $V$  and on a state variable  $\theta$ . In the most commonly used form:

$$\mu(V, \theta) = \mu^* + a \ln \frac{V}{V^*} + b \ln \frac{V^*\theta}{D_c} \quad (3.1)$$

where  $\mu^*$  is the reference friction coefficient,  $V^*$  the reference slip rate,  $D_c$  the characteristic slip distance of state evolution,  $a$  and  $b$  the constitutive parameters quantifying the importance of the direct and evolution effects, respectively. The state variable  $\theta$  evolves with time, as described by empirical evolution laws. Here we adopt the so-called "slip law", the state evolution law that is most consistent with laboratory experiments (Bhattacharya et al. 2015):

$$\dot{\theta} = -\frac{V\theta}{D_c} \ln \frac{V\theta}{D_c} \quad (3.2)$$

At steady state, i.e. when  $\dot{\theta} = 0$ , the friction coefficient is

$$\mu_{ss}(V) \doteq \mu(V, D_c/V) = \mu^* + (a - b) \ln \frac{V}{V^*} \quad (3.3)$$

When  $a - b < 0$ , the steady-state friction coefficient  $\mu_{ss}(V)$  decreases as slip rate increases, the fault is velocity-weakening (VW). Spontaneous slip transients occur if the fault stiffness (which is inversely proportional to the fault size) is below a critical stiffness that depends on friction properties and effective normal stress. A VW fault is conditionally stable: it is unstable if its size  $L$  exceeds a certain critical length  $L_c$ :

$$L_c = \frac{GD_c}{\sigma(b - a)} \quad (3.4)$$

where  $G$  is shear modulus. We refer to a fault with size larger than  $L_c$  as *supercritical*. An unstable VW fault is seismic if  $L \gg L_c$  (very supercritical) and aseismic if  $L \gtrsim L_c$  (slightly supercritical). If  $L < L_c$ , we qualify the fault as subcritical. Under the slip law, a subcritical fault is stable when driven by steady loading, but can

develop fast slip transients if stimulated by an external perturbation of sufficiently large amplitude (Gu and Wong 1994). If  $a-b > 0$ , the fault is velocity-strengthening (VS). A VS fault is stable, but it can host slip transients when perturbed (e.g. Perfettini and Ampuero 2008).

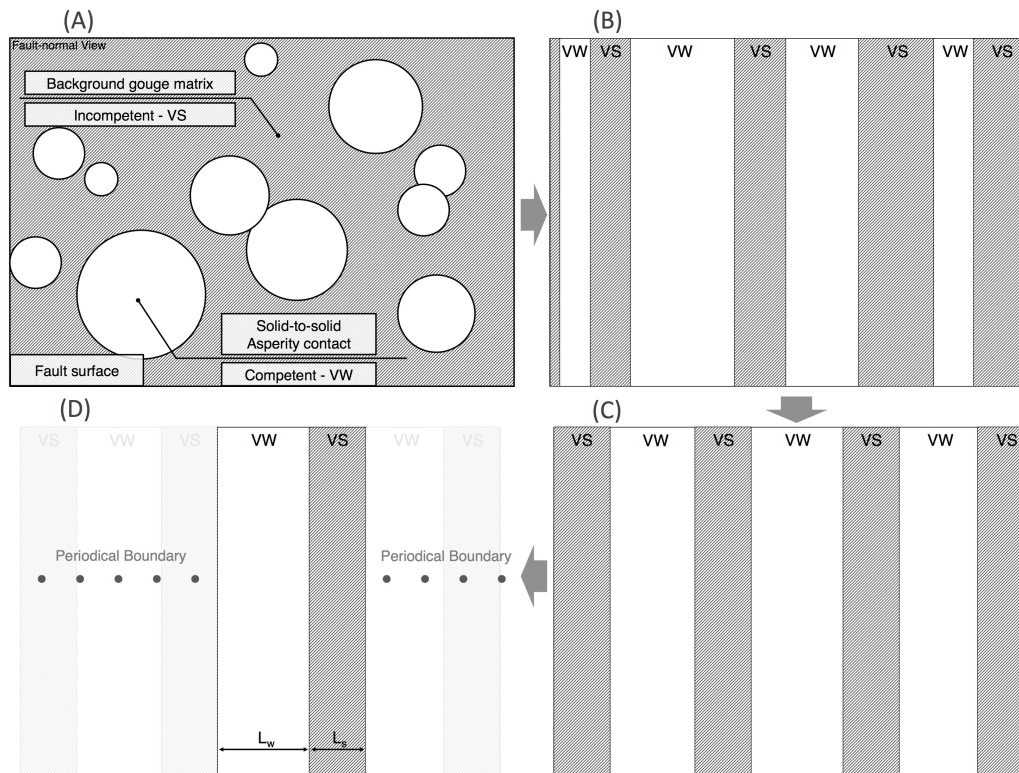


Figure 3.2: Realization and simplification of the asperity conceptual model in Figure 3.1. (A) Asperity conceptual model, the solid-to-solid asperity contact and the background gouge matrix is represented as VW and VS material, retrospectively. (B) The asperities and the background gouge are simplified as 1D along-dip strips. (C) The VW/VS strips are then regularized in space. (D) Assuming that slip remains spatially periodic in VW/VS segments, periodical along-strike boundary condition is applied on one pair of VW/VS stripe (with length of  $L_w$  and  $L_s$ , respectively), the fault is ultimately reduced into a infinitely long, linear fault in a 2D medium with periodic alternation of VW and VS segments

We adopt a minimalistic approach to model the effects of having a mixture of competent and incompetent materials in a fault zone. In nature the heterogeneity of the fault spans a large range of length scales (Fagereng 2011), and also in our proposed conceptual asperity model (Figure 3.1). We consider a simplified representation of the heterogeneous fault: the competent asperity contacts and incompetent background gouge matrix are interpreted as VW and VS materials,

respectively (Figure 3.2 (A)). The asperities and the gouge matrix are then simplified as 1D along-dip strips (Figure 3.2 (B)). We further assume a pattern of material heterogeneity repeats in space, with a spatial period  $L$  containing one VW strip and one VS strip (Figure 3.2 (C)). We assume that slip remains spatially periodic, also with spatial period  $L$ . In this way, the heterogeneous fault is reduced to an infinitely long, linear fault in a 2D medium with periodic alternation of VW and VS segments (Figure 3.2 (D)). These simplifications allow us to do the simulations on a single period of the heterogeneous pattern, reducing computational cost significantly and allowing a broad parametric study.

We study the behavior of the model numerically, by performing multi-cycle quasi-dynamic simulations. The quasi-dynamic approach utilizes radiation damping to approximate the effect of inertia (Rice 1993). We employ the software QDYN (Luo et al. 2017a), which utilizes the boundary element method (BEM, used in rate-and-state earthquake simulations since Tse and Rice (1986)) and adaptive time-stepping. To focus on features that are independent of the (arbitrary) initial conditions, we perform multi-cycle simulations and discard the initial "warm-up" cycles from our analysis.

To incorporate the effect of the missing third dimension while keeping the computational efficiency of a 2D model, we adopt a 2.5D approximation similar to that by Hawthorne and Rubin (2013). We consider a 2D fault embedded in an unbounded elastic 3D medium. The fault is infinitely long along strike but has a finite width  $W$  along dip. We assume the depth-dependence of slip is known and has the same shape as a function of depth at all positions along strike. We then reduce the problem to a 2.5D problem in which we solve only for slip variations along strike. The static stress transfer involves convolution between slip and an elasto-static stress interaction kernel, which is efficiently computed via Fast-Fourier Transform (FFT). A brief derivation of the 2.5D static kernel in spectral domain is given in appendix 3.6.

To further simplify the problem, we assume slip is uniform within the VW segment. Thus in practice, the VW segment is represented by a single computational cell, while the VS segment is a continuum in which slip is well resolved in space and time.

physical properties	value
fault period $L$	200 m
fault width $W$	110 km (primary)   11 km   1.1 km
shear modulus $G$ (Lamé's second parameter)	30 GPa
shear wave velocity	3000 m/s
reference friction coefficient $\mu^*$	0.6
tectonic loading rate $V_{pl} = V^*$	$10^{-9}$ m/s
VW/VS area ratio $f$	1   1/3   1/7
VW effective normal stress $\sigma_w$	0.5-250 MPa (various)
VS effective normal stress $\sigma_s$	5 MPa
VW characteristic slip distance $D_{cw}$	$4 \times 10^{-8} - 4 \times 10^{-1}$ m
VS characteristic slip distance $D_{cs}$	$4 \times 10^{-4}$ m (primary)   $4 \times 10^{-3}$ m
VW friction coefficient $a_w$ (direct effect)	0.009
VW friction coefficient $b_w$ (indirect effect)	0.01
VS friction coefficient $a_s$ (direct effect)	0.12
VS friction coefficient $b_s$ (indirect effect)	0.01
(arbitrary and artificial) constrain relation	$\xi^2 = \frac{f}{1+f} \frac{\alpha}{6\beta}$

Table 3.1: Typical values of parameters used in rate-and-state simulation.

### Non-dimensional model parameters and parametric study program

Table 3.1 shows the list of symbols, the corresponding range of parameters studied and the typical values of model parameters. Despite being minimalistic, the model has as many as seven essential independent non-dimensional numbers:

1. *Relative strength*  $\alpha = \frac{(b_w - a_w)\sigma_w}{(a_s - b_s)\sigma_s}$  is the ratio between the amount of weakening in the VW area to the amount of strengthening in the VS area, due to heterogeneity of  $|b - a|\sigma$ .
2. *Individual criticalness of the VW segment*  $\beta = \frac{L_w}{L_{cw}} = \frac{L_w((b_w - a_w)\sigma_w)}{\mu D_{cw}}$  is the ratio between the size of the VW segment,  $L_w$ , and the critical nucleation size of the VW material ( $L_{cw}$ ). If the VW segment were isolated, instead of embedded in a VS matrix, it would be unstable if  $\beta > 1$ .
3. *VW/VS area ratio*  $f = L_w/L_s$ , where  $L_s$  is the size of the VS segment.
4. *VW/VS characteristic slip distance ratio*  $\xi^2 = D_{cw}/D_{cs}$ .
5. *Fault aspect ratio*  $W' = W/L$  is the ratio of the fault width  $W$  to the assumed spatial period of the fault,  $L$ .
6. *a/b ratio of VW segment*,  $\gamma_w = a_w/b_w$ .

7.  $a/b$  ratio of VS segment,  $\gamma_s = a_s/b_s$ .

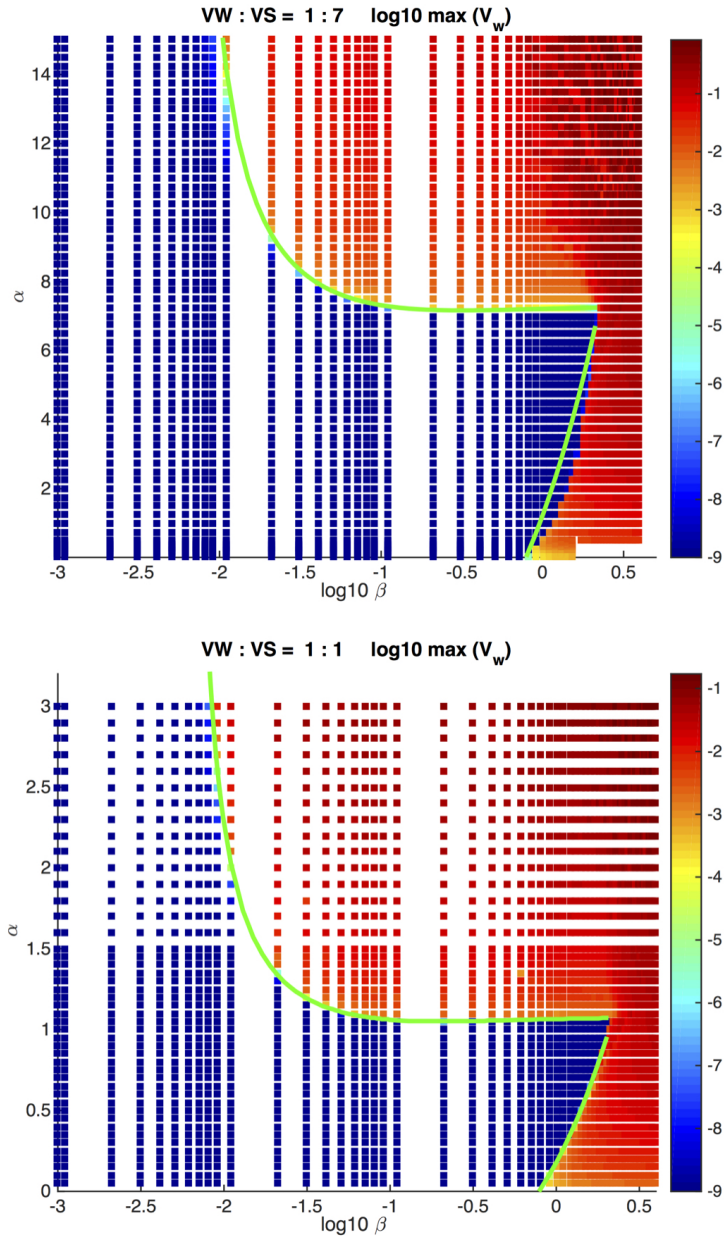


Figure 3.3: Top: Comparison of rate-and-state simulation results and corresponding linear stability analysis results varying  $\alpha$  and  $\beta$ , with  $f = 1/7$ . Color-coded squares: logarithmic peak slip rate reached in the VW segment after the "warm-up" cycles in rate-and-state simulation, each square represents one simulation. Green solid curve: corresponding full LSA results (Equation 3.9). Bottom:  $f = 1$

[Skarbek et al. \(2012\)](#) studied the effect of  $f$ ,  $\gamma_w$  and  $\gamma_s$  on the fault stability of a similar heterogeneous fault model. In this work, we study the role of the first

five non-dimensional numbers listed above. We pay particular attention to the first non-dimensional number,  $\alpha$ . In this section, we further focus on the first three non-dimensional numbers. The results will serve as reference in section 3.3 to validate the LSA approach. Once the agreement between rate-and-state models and LSA is demonstrated, the less computationally demanding LSA will allow us to study the model behavior over a broader range of parameters and to develop more general implications.

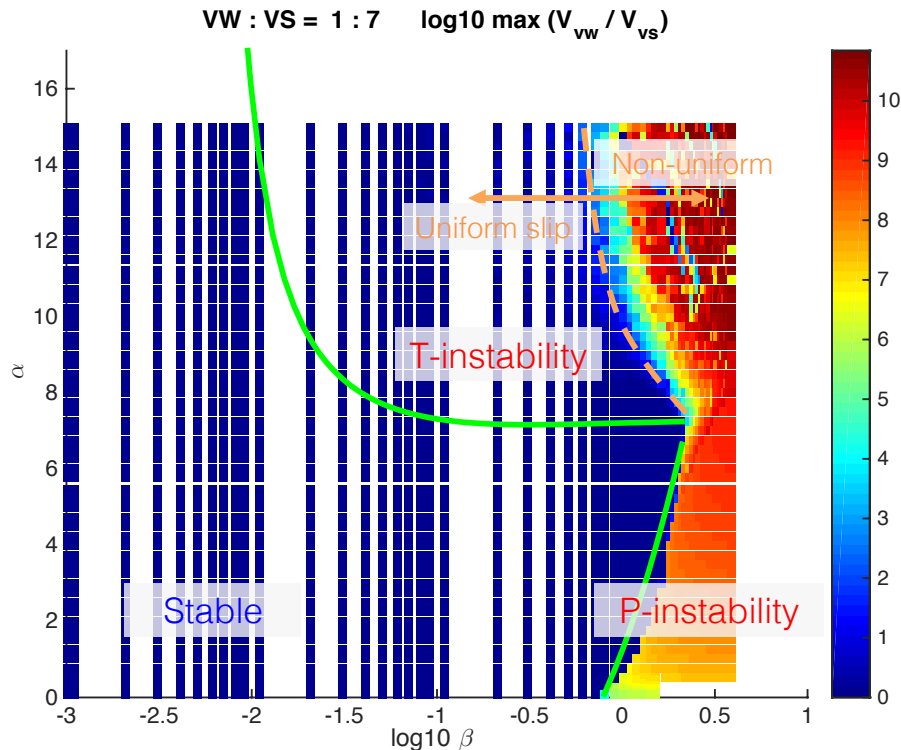


Figure 3.4: Analogous to Figure 1. Color-coded squares: maximum slip rate contrast between the VW segment and the center of VS segment (maximum ratio of slip rate measured at the VW segment and in the center of VS segment at the same time). Models with large slip rate contrast in general means slip is non-uniform over the fault. Green solid curve: corresponding full LSA results (Equation 3.9). Orange dash curve: approximate boundary of T-instability with uniform and non-uniform slip.

The program of the parametric study in this section is summarized as follows. We perform quasi-dynamic rate-and-state simulations varying the VW/VS area ratio,  $f$ , fault relative strength,  $\alpha$ , and criticalness of the VW segment,  $\beta$ , while keeping  $a_w, a_s, b_w, b_s, \sigma_s$  and  $D_{cs}$  fixed. We vary  $\alpha$  by changing  $\sigma_w$ . This also changes  $\beta$ , but we further control  $\beta$  by varying  $D_{cw}$ . We consider three different values

of  $f = 1, 1/3$  and  $1/7$ . Defining a characteristic length in the VS segment as  $L_{cs} = \frac{\mu D_{cs}}{(a_s - b_s)\sigma_s}$ , we keep the ratio  $L_{cs}/L$  fixed and equal to an arbitrary value of 6. This ratio is related to other non-dimensional numbers by  $L_{cs}/L = \frac{f}{1+f} \frac{\alpha}{\beta \xi^2}$ . Hence our approach also changes  $\xi$ , following the relation  $\xi^2 = \frac{f}{1+f} \frac{\alpha}{6\beta}$ . Later in section 3.3, we use LSA to explore the effect of  $L_{cs}/L$ , characteristic slip distance ratio  $\xi^2 = D_{cw}/D_{cs}$  and fault aspect ratio  $W'$ .

### Results of numerical simulations

The results of a set of simulations with fixed  $f = 1/7$  and varying  $\alpha$  and  $\beta$  are summarized in [Figure 3.3 top](#), which shows the peak slip rate reached in the VW segment as a function of  $\alpha$  and  $\beta$  (see also examples with  $f = 1$  in [Figure 3.3 bottom](#)). A peak slip rate higher than the tectonic slip rate  $V_{pl} = 10^{-9} \text{ m/s}$  indicates fault instability manifested by spontaneous slip transients. We further quantify the uniformity of slip along the fault in [Figure 3.4](#) by the maximum ratio between the slip rates on the VW segment and at the center of the VS segment at the same time. We find that the fault stability depends on  $\alpha$  and  $\beta$ , and displays a rich spectrum of slip behaviors:

1. *Stable slip* (left and lower-left of [Figure 3.3 and 3.4](#) in blue). At low  $\beta$  (below a certain minimum value  $\beta_{min}$ ) the whole fault is stable for all  $\alpha$ . At intermediate  $\beta > \beta_{min}$ , the fault is stable only for small  $\alpha$  (smaller than a certain value  $\alpha_T$  that depends on  $\beta$ ).
2. *Total instability* (upper-right of [Figure 3.3 and 3.4](#)). When  $\alpha > \alpha_T(\beta)$ , the whole fault is unstable: both the VW and VS segments slip episodically. We name this "T-instability", short for "total instability". The value of  $\alpha_T(\beta)$  decreases with increasing  $\beta$ , and converges to a constant value  $\alpha_{Tc}$ . We observe that  $\alpha_{Tc} \approx 1/f$  ([Figure 3.5 and Figure 3.3](#)). Two main patterns of slip are observed in the regime of T-instabilities ([Figure 3.4](#)). When  $\alpha$  is slightly above  $\alpha_T(\beta)$ , unstable slip is uniform along the whole fault ([Figure 3.4](#); see also slip patterns in [Figure 3.6\(A\)](#)). With the increase of  $\alpha$ , fault slip gradually transits into more complicated patterns. When  $\alpha$  is well above  $\alpha_T(\beta)$ , instability with non-uniform slip occurs. In this regime we observe multi-stage super-cycle behavior in which T-instabilities are preceded by one or multiple failures that start in the VW segment but do not propagate over the whole fault ([Figure 3.6\(C\)](#)). In super-cycles with multiple precursors, each precursor consistently penetrates further into the VS area and the inter-

event time between each precursor shortens until a large event ruptures the whole fault. The inter-event time and magnitude of T-instabilities increase with increasing  $\alpha$  and decreasing  $\beta$  (Figure 3.7). Also note that near the T-instability boundary, there is a narrow transitional regime where the fault slips aseismically (yellow-to-green color in Figure 3.3)

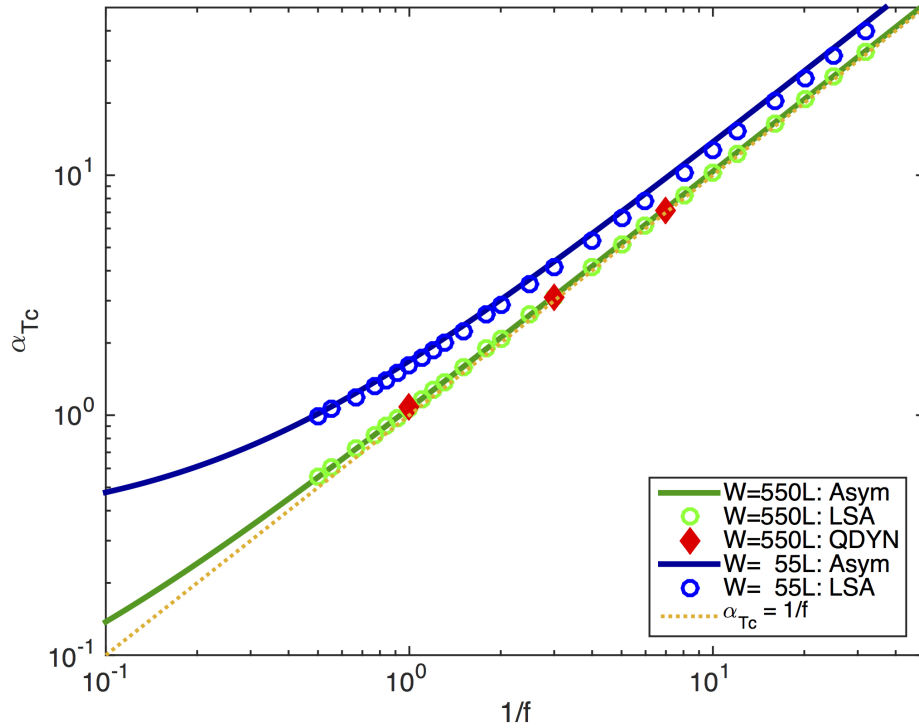


Figure 3.5: Comparison of the horizontal asymptotic limit  $\alpha_{Tc}$  between rate-and-state simulations, LSA, and simplified equations with various  $f$  value. Red diamond:  $\alpha_{Tc}$  measured from rate-and-state simulations, with  $f = 1, 1/3$  and  $1/7$ ,  $W = 550L$ . Green circle:  $\alpha_{Tc}$  measured from full LSA results (Equation 3.9),  $W = 550L$ . Dark green solid curve: asymptotic Equation 3.35 with  $W = 550L$ . Golden dotted line:  $\alpha_{Tc} = 1/f$ . Blue circles and solid curve:  $\alpha_{Tc}$  measured from full LSA (Equation 3.9) and corresponding asymptotic Equation 3.35 with  $W = 55L$ .

3. *Partial instability* (lower-right of Figure 3.3 and 3.4). At larger  $\beta$  (above a certain  $\beta_{P\_min} \approx 1$ ) and low  $\alpha$  (below a certain  $\alpha_P(\beta) < \alpha_{Tc}$ ), partial instabilities occur in which unstable slip is mainly confined to the VW segment (Figure 3.4, Figure 3.6(B)). We refer to these as "P-instabilities". Their existence is expected from the instability of an isolated VW segment, without surrounding VS segments, whose size exceeds the critical nucleation size

$L_c$  (Ampuero and Rubin 2008; Rubin and Ampuero 2005). However, such interpretation predicts the P-instability should happen at a critical value of  $\beta$ , independent of  $\alpha$  (i.e. a vertical boundary is expected in Figure 3.3 and 3.4), which is in contrast with our simulation results. Thus, the interaction between VW and VS parts of the fault influences the P-instability. The inter-event time and magnitude of P-instabilities are much smaller than those of T-instabilities. The ratio of both inter-event time and magnitude between T-instability and P-instability are roughly proportional to the ratio of  $W/L_w$  (Figure 3.7). Also, the inter-event time and magnitude of P-instabilities, as well as their rupture penetration distance into the VS area, all increase with increasing  $\alpha$  (Figure 3.7). If  $\alpha$  increases, P-instabilities are eventually merged with T-instabilities. If  $\beta$  is large this transition is direct, but at intermediate values of  $\beta \approx 1$  a transitional stable regime exists between P-instability and T-instability (Figure 3.3 and 3.4).

4. At large  $\beta > \beta_{max}$  (to the right of Figure 3.3 and 3.4) the fault is unstable for any  $\alpha$ , by either P-instability or T-instability. At low  $\alpha$  (roughly below  $\alpha_{Tc}$ ) P-instability occurs. At high  $\alpha > \alpha_{Tc}$ , T-instability occurs with non-uniform slip. We observe no instability with uniform slip in our simulations. Slip behavior can be complicated near the zone of convergence of T-instability and P-instability (Figure 3.6(D)). We see super-cycles interspersed by clustered occurrences of rupture of the VW segment, with short inter-event-times, and penetrating substantially into the VS part.

### 3.3 Linear stability analysis

#### Model concepts and assumptions

To study the fundamentals of the problem and to gain a better understanding of the two distinct unstable regimes observed in our rate-and-state simulations, we perform a theoretical study of the models using linear stability analysis of a periodic two-degree-of-freedom spring-block system, similar to Skarbak et al. (2012). To further simplify the problem while preserving its essence, we assume that slip is uniform within each VW and VS segment. That reduces the model to a Burridge-Knopoff model: a linear array of blocks connected by springs and loaded by constant velocity through side springs. With the assumed periodic alternation of VW and VS blocks, the model is reduced to a two-degree-of-freedom system with periodic boundary conditions (Figure 3.8).

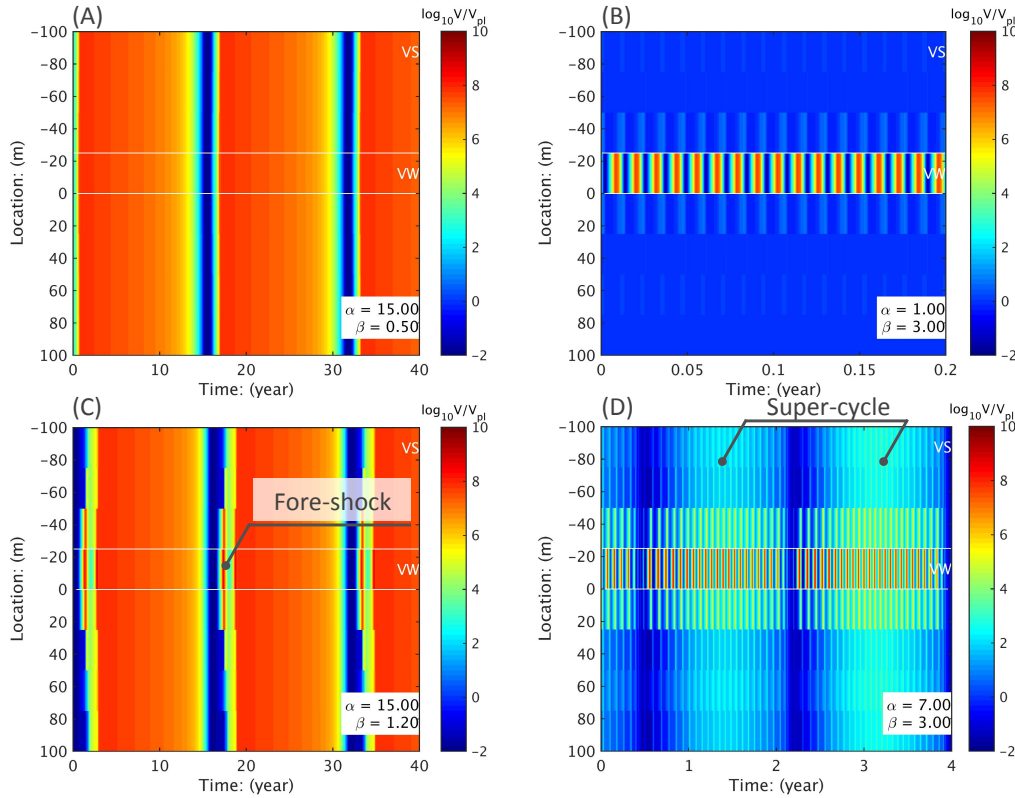


Figure 3.6: Slip patterns with various VW self-criticalness  $\beta$  and relative strength contrast  $\alpha$ . Color shows logarithmic slip rate normalized by loading rate  $V_{pl}$  as a function of time and location from selected rate-and-state simulations with  $f = 1/7$ . Boundary of the VW segment is marked with white lines in each plot. Please note the difference in time scale. (A) Typical T-instability, the whole fault ruptures with inter-event time in the order of years (controlled by fault width  $W$ ). (B) Typical P-instability, rupture is mainly confined in the VW segment, with inter-event time in the order of days (controlled by VW segment size  $L_w$ ). (C) T-instability with fore-shock(s), in which a large event ruptures the whole fault is preceded by smaller event(s) rupturing part of the fault. (D) "Hybrid" behavior of which long inter-event-time, whole-fault rupturing super-cycles are interspersed by clustered occurrences of rupture of the VW segment, with short intervals.

In a non-linear system, a steady state solution is linearly unstable if the linearization of the system in the vicinity of this solution is in the form of  $\frac{dx}{dt} = \bar{A}x$ , and at least one of the eigenvalues of the linear operator  $\bar{A}$  has a positive real part. In that case any small perturbation to the system diverges and the system deviates from steady-state. Otherwise if all of the eigenvalues of the linear operator  $\bar{A}$  have negative real parts, the system at the solution is linearly stable (Glendinning 1994). This method to study the stability of a system is called linear stability analysis (LSA).

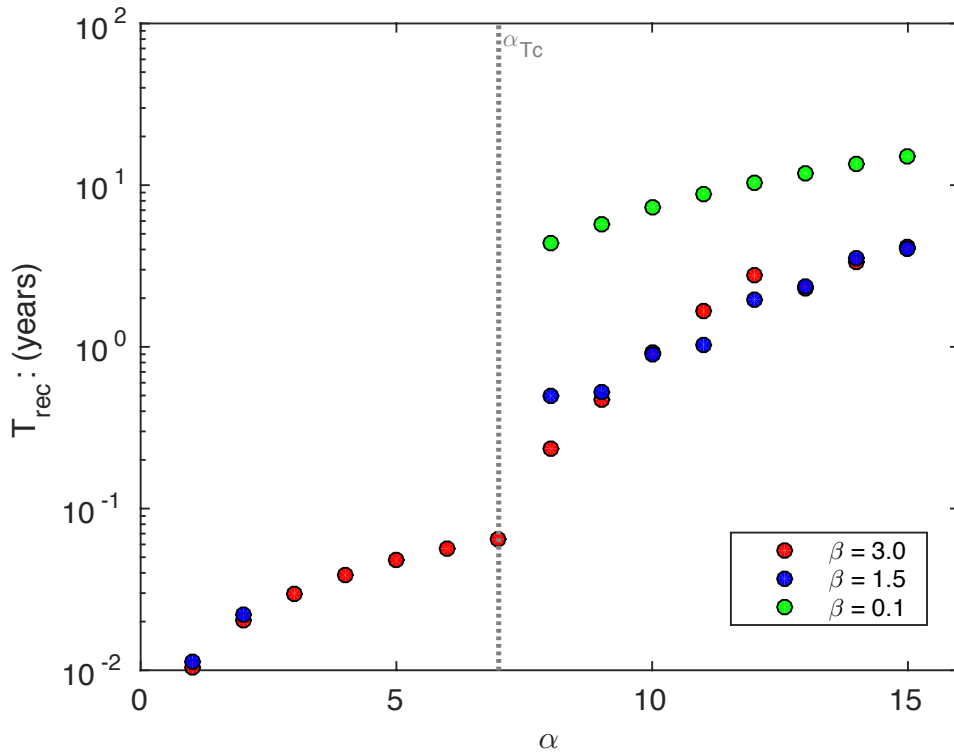


Figure 3.7: Measured average inter-event time of models with different VW self-criticalness  $\beta$  as a function of relative strength  $\alpha$ . Grey dotted line:  $\alpha_{Tc} = 1/f$ , which in general separates T-instability and P-instability. The inter-event time increase with increasing  $\alpha$ . When the relative strength is above  $\alpha_{Tc}$  the inter-event time is in the order of years, whereas below  $\alpha_{Tc}$  the inter-event time is in the order of days.

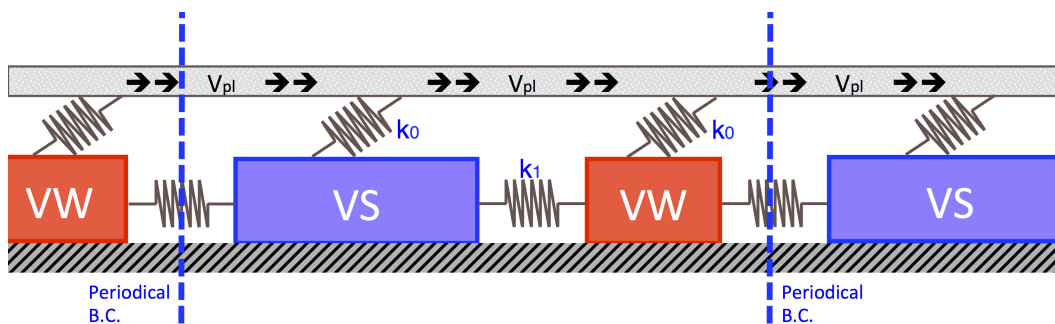


Figure 3.8: sketch for two-degree-of-freedom spring-block system. The system consists of two periodical VW and VS blocks inter-connected by a spring, and both loaded with side springs at constant speed.

### LSA derivation

With the aforementioned simplification, we utilize LSA to analyze the stability of the system, which can be summarized as three steps. Below we will only show the

essence of the LSA study and major results.

The first step is the derivation of the governing equations from the discrete stress transfer equations (and extension to arbitrary VW/VS ratio) in [appendix: 3.6](#):

$$\tau_w = K_I(v_{ss}t - \delta_w) + K_{II}(\delta_s - \delta_w) \quad (3.5)$$

$$\tau_s = K_I(v_{ss}t - \delta_s) + fK_{II}(\delta_w - \delta_s) \quad (3.6)$$

where  $\tau_w$  and  $\tau_s$  are the shear stresses of the VW and VS parts, respectively;  $K_I = K_w = \pi\mu W$  is the stiffness corresponding to plate loading;  $K_{II} = K_0 - K_w$  is the stiffness corresponding to inter-block interactions;  $K_0$  is the self-stiffness of a VW block.

The second step is to linearize the governing equations and apply the condition of stability (see [appendix: 3.6](#)). The final eigenvalue problem takes the form of:

$$\begin{aligned} Q(\lambda) = & \begin{pmatrix} a_w\sigma_w/v_{ss} & 0 \\ 0 & a_s\sigma_s/v_{ss} \end{pmatrix} \lambda^2 \\ & + \begin{pmatrix} (a_w - b_w)\sigma_w/D_{cw} + K_I + K_{II} & -K_{II} \\ -fK_{II} & (a_s - b_s)\sigma_s/D_{cs} + K_I + fK_{II} \end{pmatrix} \lambda \quad (3.7) \\ & + \begin{pmatrix} (K_I + K_{II})v_{ss}/D_{cw} & -K_{II}v_{ss}/D_{cw} \\ -fK_{II}v_{ss}/D_{cs} & (K_I + fK_{II})v_{ss}/D_{cs} \end{pmatrix} \end{aligned}$$

The eigenvalues are the roots  $\lambda$  of

$$\det(Q(\lambda)) = 0 \quad (3.8)$$

The system is unstable if the real part of at least one eigenvalue is positive.

The third step is to solve the instability condition to get the stability boundary. The stability condition from Equation 3.8 is a quartic equation:

$$\det(Q) = s_4\lambda^4 + s_3\lambda^3 + s_2\lambda^2 + s_1\lambda + s_0 = 0 \mid \exists Re(\lambda) > 0 \quad (3.9)$$

where

$$s_0 = K_I(K_I + (1 + f)K_{II}) \quad (3.10)$$

$$s_1 v_{ss} = K_I(K_I + (1 + f)K_{II})(D_{cw} + D_{cs}) \\ + (A_w - B_w)(K_I + fK_{II}) + (A_s - B_s)(K_I + K_{II}) \quad (3.11)$$

$$s_2 v_{ss}^2 = K_I(K_I + (1 + f)K_{II})D_{cw}D_{cs} + (A_w - B_w)(A_s - B_s) \\ + (A_w D_{cw} + (A_w - B_w)D_{cs})(K_I + fK_{II}) \\ + (A_s D_{cs} + (A_s - B_s)D_{cw})(K_I + K_{II}) \quad (3.12)$$

$$s_3 v_{ss}^3 = A_w A_s (D_{cw} + D_{cs}) - A_w B_s D_{cw} - A_s B_w D_{cs} \\ + A_s D_{cw} D_{cs} (K_I + K_{II}) + A_w D_{cw} D_{cs} (K_I + fK_{II}) \quad (3.13)$$

$$s_4 v_{ss}^4 = A_w A_s D_{cw} D_{cs} \quad (3.14)$$

$$(A_i = a_i \sigma_i, B_i = b_i \sigma_i) \quad (3.15)$$

The analytical solution of these roots is too complicated to provide useful insight. To make further progress we take two complementary approaches. In the first approach we solve Equation 3.9 numerically. In the second approach we try to simplify Equation 3.9 by looking for roots with zero real part. If it is a real root, then  $\lambda = 0$  and Equation 3.9 implies  $s_0 = 0$ , which is not possible. Hence  $\lambda$  is purely imaginary, and the real and imaginary parts of Equation 3.9 give two equations:

$$s_4 \lambda^4 + s_2 \lambda^2 + s_0 = 0 \quad (3.16)$$

$$s_3 \lambda^3 + s_1 \lambda = 0 \quad (3.17)$$

Equation 3.17 gives  $\lambda^2 = -s_1/s_3$ . Plugging that into the Equation 3.16 gives a simplified condition of instability boundary:

$$s_1(s_4 s_1 - s_2 s_3) + s_0 s_3^2 = 0 \quad (3.18)$$

Equation 3.18 can be put in the same form as [\(Skarbek et al. \(2012\) Supplementary Equation S22\)](#), but here we have instead derived the condition analytically rather than through a semi-empirical method. The simplified condition (Equation 3.18) is still too complicated to be solved analytically. However, it helped us develop further simplified approximations for the stability boundaries, which will be discussed in the next section 3.4. At this stage, a numerical method is used to solve for the system stability under the simplified condition (Equation 3.18). Both Equation 3.18 and Equation 3.9 yield same results, as expected. The results of linear stability analysis will be extensively discussed in the next subsection.

## LSA results

Similar to the QDYN rate-and-state simulations, we keep  $a_w$ ,  $a_s$ ,  $b_w$ ,  $b_s$ ,  $\sigma_s$  and  $D_{cs}$  fixed and vary the non-dimensional parameters  $\alpha$  and  $\beta$  systematically. We solved the full LSA condition Equation 3.9 to determine the stability of the simplified spring-block system. The LSA results are shown in Figure 3.3. Despite the approximations, the LSA results are in strikingly good agreement with the rate-and-state simulation results for both models of  $f = 1$  and  $f = 1/7$ . That agreement allows us extend our study to a much larger parametric space, for the reason that solving LSA is far more computational efficient than performing rate-and-state simulations. However LSA comes with limitations that it only predicts whether the system is stable or not, while provides no readily available details about instability, e.g. whether it is seismic or aseismic, or whether slip is uniform across the VS and VW segment or not (comparing to rate-and-state simulations in Figure 3.3).

With the aid of LSA, we first extend our study by varying the value of  $f$  (Figure 3.5), whereas we only examined three values in our rate-and-state simulations,  $f = 1/1$ ,  $1/3$  and  $1/7$ . We confirmed that (same as rate-and-state simulations) the asymptotic limits of critical of T-instability at large  $\alpha$  (horizontal boundary  $\alpha_{Tc}$ ) derived from LSA and measured from rate-and-state results are both nearly proportional to  $1/f$  (with many data points of various  $f$  from LSA in Figure 3.5).

We then relieve the constraint we placed on our previous rate-and-state simulation with fixed  $\frac{\alpha}{\beta\xi^2}$ . We allow  $D_{cw}$  to vary freely and study the system stability by varying  $\alpha$  and  $\xi^2 = D_{cw}/D_{cs}$  (Figure 3.9) (hereafter referred as the  $\alpha - \xi$  system). The result is similar to varying  $\alpha$  and  $\beta$  (thereafter referred as the  $\alpha - \beta$  system), except the horizontal axis is reversed as larger  $D_{cw}$  in principle maps to smaller  $\beta$  when other parameters are fixed:

1. At large  $\xi$ , the fault is stable only for small  $\alpha < \alpha_T(\xi)$ . When  $\alpha > \alpha_T(\xi)$ , the fault is unstable. The value of  $\alpha_T(\xi)$  decreases with decreasing  $\xi$ , at large  $\xi$ ,  $\alpha_T(\xi) \propto \xi^2$ , at intermediate  $\xi$ ,  $\alpha_T(\xi)$  converges to a near-constant value  $\alpha_{Tc}$ , as the case of "T-instability" in the  $\alpha - \beta$  system, and  $\alpha_{Tc} \approx 1/f$ .
2. At small  $\xi < \xi_{min}$  (to the left of Figure 3.9, below a certain value  $\xi_{min}$ ), another stability boundary appears and converge with the previous boundary at  $\xi_{min}$ . It is in fact same as the case of "P-instability" in the  $\alpha - \beta$  system, albeit we do not observe the unstable-stable-unstable transition discovered in the  $\alpha - \beta$

system with variation of  $\alpha$ , and the system behavior is monotone with respect to variation of  $\alpha$  or  $\xi$ .

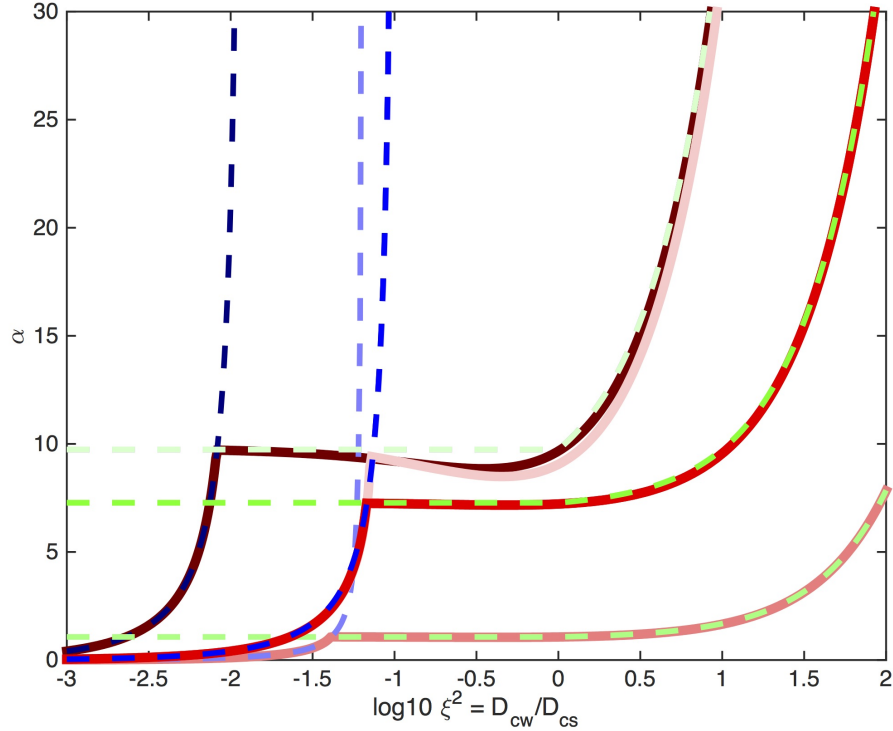


Figure 3.9: Instability boundary with respect to various  $\alpha$  and  $\xi$ ,  $f = 1/7$ , and simplified approximations. Red solid curve: full LSA results (Equation 3.9); blue dashed curve: approximation Equation 3.68 for the P-instability boundary; Green dashed curve: approximation Equation 3.50 for the T-instability boundary. Lighter colors represent cases with  $f = 1$ . Darker colors represent cases with  $f = 1/7$  and 10 times larger  $D_{cs}$ . Lightest colors represent cases with  $f = 1/7$  and 10 times smaller  $W'$ .

With the convenience of LSA we are able to study the other non-dimensional numbers as well. The effect of  $L_{cs}/L$  is studied by varying the value of  $D_{cs}$ . An example of 10 times larger  $D_{cs}$  is shown in Figure 3.9. Doing so both the P-instability and T-instability boundaries are affected, the value of  $\xi_{min}^2$  decreases by a factor of 10, as expected, while the value of  $\alpha_{Tc}$  is positively correlated to  $D_{cs}$ .

We also studied the effect of  $W'$  by varying the value of  $W$ . Figures 3.9 and 3.10 show that the T-instability boundary is largely affected by changing of  $W'$ , similar to a change of  $D_{cs}$ . The  $\beta$  value at the vertical asymptotic limit of the T-instability boundary (which only exists in the  $\alpha - \beta$  system),  $\beta_{min}$ , is proportional to  $1/W'$ .

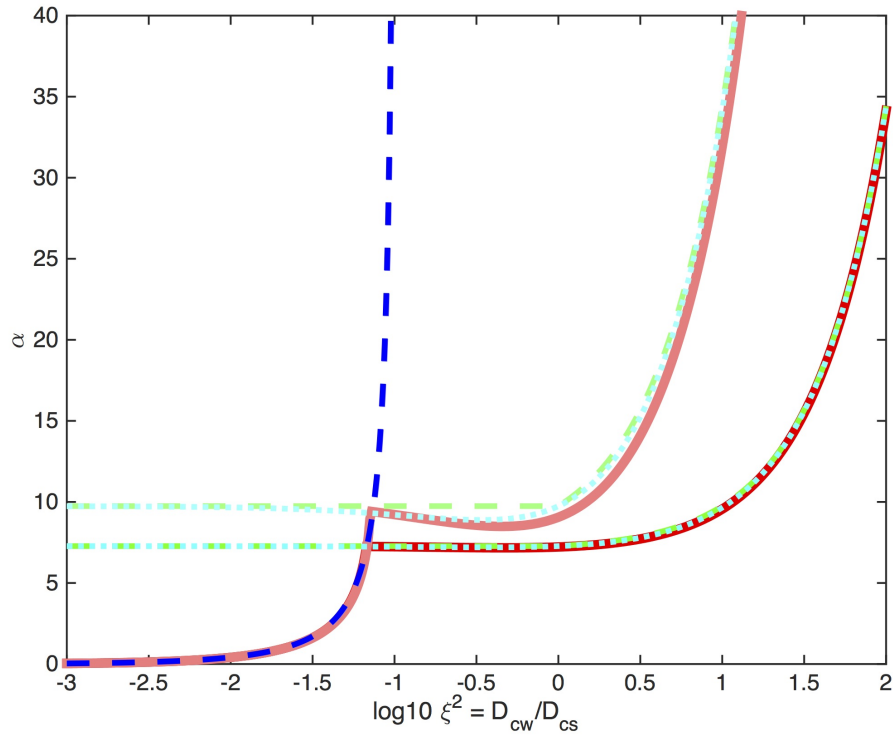


Figure 3.10: analogous to Figure 3.9. Instability boundary with respect to various  $\alpha$  and  $\xi$ ,  $f = 1/7$ , and simplified approximations. Red solid curve: full LSA results (Equation 3.9); blue dashed curve: approximation Equation 3.68 for the P-instability boundary; Aqua dotted curve: approximation Equation 3.29 for the T-instability boundary; Green dashed curve: approximation Equation 3.50 for the T-instability boundary. Lighter colors represent cases with 10 times smaller  $W'$ .

The value at the horizontal asymptotic limit of the T-instability boundary ( $\alpha_{Tc}$ ) for both  $\alpha - \beta$  system and  $\alpha - \xi$  system is positively related to  $1/W'$ . The boundary of P-instability does not change much with  $W'$ . This is expected as the P-instability boundary is mostly controlled by the self-stiffness of the VW segment, which is inversely proportional to its size  $L_w$ , and significantly larger than the fault bulk stiffness, which is inversely proportional to fault width  $W$ . Those effects will be derived analytically in section 3.4.

### 3.4 Prediction of instability boundaries

In the previous section 3.3 we have demonstrated that LSA accurately predicts the stability of the system. Yet the analysis is still too complicated to make any straightforward predictions on the stability of the heterogeneous fault model without solving the LSA equations numerically (Equations 3.9 or 3.18). In this section we

will utilize appropriate heuristic approximations to analyze the derived stability conditions Equation 3.18. We are able to simplify the stability conditions equation and derive both "T-instability" and "P-instability" boundaries in closed form. In the end we will also propose two compact formulas that accurately predict the instability conditions.

## T-instability boundary

### Derivation of the T-instability boundary

We observed that fault slips uniformly near the T-instability boundary, i.e. both the VW and VS part of the fault has same slip rate at any time:  $V_w = V_s$ . This allows us to make the approximation of  $K_{II} \rightarrow +\infty$ , an infinite rigid connection between the VW and VS blocks. For convenience, we use  $f_w = f/(1+f)$  and  $f_s = 1/(1+f)$  which is the portion of the VW and VS block, respectively. We also define the spatial average of any physical property as  $\langle X \rangle = f_w X_w + f_s X_s$ . Use  $K_{II} \rightarrow +\infty$  and divide the coefficient  $s_i$  of the instability boundary in Equation 3.9 by  $K_{II}(1+f)$  we have:

$$s_0 = K_I \quad (3.19)$$

$$s_1 = (\langle A - B \rangle + K_I(D_{cw} + D_{cs}))/v_{ss} \quad (3.20)$$

$$s_2 = (\langle AD_c \rangle + (\langle (A - B)/D_c \rangle + K_I)D_{cw}D_{cs})/v_{ss}^2 \quad (3.21)$$

$$s_3 = \langle A \rangle D_{cw}D_{cs}/v_{ss}^3 \quad (3.22)$$

$$s_4 = 0 \quad (3.23)$$

On the other hand,  $K_{II} \rightarrow +\infty$  and apparently  $s_3 \neq 0$ . That also reduced the instability boundary Equation 3.18 into:

$$s_1 s_2 = s_0 s_3 \quad (3.24)$$

Which is now a quadratic equation for  $K_I$ :

$$K_I^2 + C_1 K_I + C_2 = 0 \quad (3.25)$$

where

$$C_1 = \langle A \rangle \left( \frac{1}{D_{cw}} + \frac{1}{D_{cs}} \right) - \langle \frac{B}{D_c} \rangle - \frac{\langle B \rangle}{D_{cw} + D_{cs}} \quad (3.26)$$

$$C_2 = \frac{\langle A - B \rangle}{D_{cw} + D_{cs}} \left( \langle A \rangle \left( \frac{1}{D_{cw}} + \frac{1}{D_{cs}} \right) - \langle \frac{B}{D_c} \rangle \right) \quad (3.27)$$

Equation 3.25 has two solutions:

$$K_I = \frac{1}{2}(-C_1 \pm C_1 \sqrt{1 - \frac{4C_2}{C_1^2}}) \quad (3.28)$$

We analyzed in the homogeneous case and verified numerically in heterogeneous case, that only the "+" solution is physical:

$$K_I = \frac{1}{2}(-C_1 + C_1 \sqrt{1 - \frac{4C_2}{C_1^2}}) \quad (3.29)$$

Equation 3.29 precisely defines the T-instability boundary in closed form, and is in perfect match with the complete LSA solution (Figure 3.10), with the exception of relatively small  $W'$ , in that case there is a small mismatch between Equation 3.29 and the complete LSA (Equation 3.9) at intermediate  $\xi$ . Yet we think in practice the difference between Equation 3.9 and Equation 3.29 is negligible, since  $W'$  as the ratio between fault width and fault heterogeneity length scale, is always expected to be large.

### Asymptotic limits of the T-instability boundary

From Equation 3.29 we are able to analyze the observed asymptotic limits in our rate-and-state simulations and the LSA studies.

**a. Horizontal T-instability boundary asymptotic limit:** As discussed previously in section 3.2 and 3.3 (Figure 3.5), in both the  $\alpha - \beta$  system and  $\alpha - \xi$  system, horizontal asymptotic T-instability boundary of  $\alpha_{Tc} \approx 1/f$  is observed at large  $\beta$  or small  $\xi$  for both rate-and-state simulations and linear stability analysis. Here we will derive this horizontal asymptotic limit directly from Equation 3.29:

For the horizontal T-instability limit, it is  $\beta \rightarrow +\infty$  in the  $\alpha - \beta$  system, or  $\xi \rightarrow 0$  in the  $\alpha - \xi$  system, which corresponds to  $D_{cw} \rightarrow 0$ , plug that back to Equation 3.29 we get:

$$\langle (B - A) \rangle / D_{cs} = K_I = \frac{\pi G}{W} \quad (3.30)$$

That indicates the overall effective critical stiffness of the mixed VW and VS system, in most situation, is simply the spatial average of the  $(b - a)\sigma$  values of the whole system, divided by the  $D_c$  value of the VS segment.

On the other hand, Equation 3.30 can be written as

$$\frac{f_s(b_s - a_s)\sigma_s + f_w(b_w - a_w)\sigma_w}{D_{cs}} = \frac{\pi G}{W} \quad (3.31)$$

While by definition

$$\alpha = \frac{(b_w - a_w)\sigma_w}{(a_s - b_s)\sigma_s} \quad (3.32)$$

Plug back to the previous equation, eliminating  $(b_w - a_w)\sigma_w$  gives the asymptotic critical  $\alpha$  at the T-instability boundary:

$$\alpha_{Tc} = \frac{(b_w - a_w)\sigma_w}{(a_s - b_s)\sigma_s} = \frac{\pi G D_{cs}}{f_w W (a_s - b_s)\sigma_s} + \frac{f_s}{f_w} \quad (3.33)$$

We define the characteristic critical length of the VS block as:

$$L_{cs} = \frac{\pi G D_{cs}}{(a_s - b_s)\sigma_s} \quad (3.34)$$

Then horizontal T-instability boundary asymptotic limit Equation 3.31 can be write as

$$\alpha_{Tc} = \frac{1}{f} + \frac{f+1}{f} \cdot \frac{\pi L_{cs}}{W} \quad (3.35)$$

While  $W$  is large, it reduces into

$$\alpha_{Tc} \approx 1/f \quad (3.36)$$

Which is consistent with our findings with rate-and-state models and LSA results [Figure 3.5](#).

**b. Vertical T-instability boundary asymptotic limit in the  $\alpha-\beta$  system:** Vertical asymptotic limit of T-instability is observed in the  $\alpha-\beta$  system in both rate-and-state simulations and linear stability analysis: the system is unconditionally stable if  $\beta$  is small than the limit of  $\beta_{min}$ . And it appears that  $\beta_{min}$  is proportional to  $1/W'$ .

For the vertical boundary asymptotic limit in the  $\alpha-\beta$  system:

$$\sigma_w/\sigma_s = D_{cw}/D_{cs} \rightarrow +\infty \quad (3.37)$$

Plugging into Equation 3.29 gives

$$(f_w(a_w - b_w)\sigma_w + K_I D_{cw})(f_w \sigma_w a_w D_{cw}) + (-f_w b_w + K_I D_{cw})K_I D_{cw} D_{cs} = 0 \quad (3.38)$$

because  $D_{cs}/D_{cw} \rightarrow 0$ , previous Equation becomes

$$(f_w(a_w - b_w)\sigma_w + K_I D_{cw})(f_w \sigma_w a_w D_{cw}) = 0 \quad (3.39)$$

that is

$$\frac{f_w(b_w - a_w)\sigma_w}{D_{cw}} = K_I = \frac{\pi G}{W} \quad (3.40)$$

multiply by fault period  $L$

$$L f_w \frac{(b_w - a_w) \sigma_w}{G D_{cw}} = \frac{\pi L}{W} \quad (3.41)$$

that is

$$\beta_{min} = L_w / L_{cw} = \pi / W' \quad (3.42)$$

We thus derived that the vertical asymptotic limit of T-instability in the  $\alpha - \beta$  system is proportional to  $1/W'$ .

**c. Diagonal T-instability boundary asymptotic limit in the  $\alpha - \xi$  system:** There is no vertical asymptotic limit of T-instability for the  $\alpha - \xi$  system. Instead, the asymptotic limit is diagonal:

$$\sigma_w / \sigma_s \propto D_{cw} / D_{cs} \rightarrow +\infty \quad (3.43)$$

Similar to the vertical limit in the  $\alpha - \beta$  system, from Equation 3.29 we have

$$f_w(a_w - b_w) \sigma_w + K_I(D_{cw} + D_{cs}) = 0 \quad (3.44)$$

that is

$$\frac{f_w(b_w - a_w) \sigma_w}{D_{cw} + D_{cs}} = K_I = \frac{\pi G}{W} \quad (3.45)$$

If  $D_{cs}$  is fixed then Equation 3.45 defines the diagonal asymptotic limit:

$$D_{cw} \propto \sigma_w \quad (3.46)$$

### Simplified approximation of the T-instability boundary

Although Equation 3.29 precisely defines the T-instability boundary in closed form, it is still in a relative complicated form. We thus use heuristic approximation trying to further simplify the T-instability boundary equation Equation 3.29. Numerical evaluation of the coefficients in Equation 3.29 shows that heterogeneous faults with various parametric settings in our study, always satisfy:

$$C_1^2 \gg C_2 \quad (3.47)$$

Second-order Taylor expansion of Equation 3.29 with respect to  $4C_2/C_1^2$  gives

$$K_I \approx \frac{1}{2} \left( -C_1 + C_1 \left( 1 - \frac{2C_2}{C_1^2} \right) \right) = -C_2/C_1 \quad (3.48)$$

that is

$$K_I = \frac{\langle B - A \rangle}{D_{cw} + D_{cs}} \left( 1 + \frac{\langle B \rangle}{D_{cw} + D_{cs}} \left( \frac{1}{\langle A \rangle (1/D_{cw} + 1/D_{cs})} - \frac{\langle B \rangle}{D_c} - \frac{\langle B \rangle}{D_{cw} + D_{cs}} \right) \right) \quad (3.49)$$

This is a very good approximation to the T-boundary in most of our simulations. However, in homogeneous media the approximation Equation 3.49 is not valid in general, in which only when  $B \approx A$  we get  $K_I \approx (B - A)/D_c$ .

On the other hand, the asymptotic limits we derived in the previous section 3.4 also holds for the approximated Equation 3.49. Inspired by those asymptotic limits and the form of Equation 3.49, we propose an ultimately simplified equation for the T-instability boundary, which is in reasonably good approximation to the complete LSA results (Figure 3.9 and 3.10), and is also valid for homogeneous faults:

$$K_I = \frac{\langle B - A \rangle}{\max(D_{cw}, D_{cs})} \quad (3.50)$$

## **P-instability boundary**

### **Derivation of the P-instability boundary**

Intuitively, the P-instability boundary ought to be the stand-alone VW block stability limit if there is no interaction between the VW and VS block, i.e.  $K_{II} = (B_w - A_w)/D_{cw}$ . That defines a vertical limit at  $\beta = 1$  in the  $\alpha - \beta$  system, which does not match the rate-and-state simulation nor the LSA results. In the  $\alpha - \xi$  system, it only matches the LSA results while  $\xi$  ( $D_{cw}$ ) is very small. That means we cannot naively treat the P-instability boundary as the case of a stand-alone VW block and ignore the effect of the VS block.

On the other hand, the complete LSA result is in very good match with rate-and-state simulation, encourage us to extract P-instability boundary from the complete LSA Equation 3.9. Inspired by the the nature of partial failure, of the fact that in general only the VW block fails, i.e. The failure is responding to the stiffness of the VW block (which is proportional to the size of VW block,  $L_w = f_w L$ ), and it is much larger than the stiffness with respect to the infinite fault while it is acting uniformly (proportional to the fault width,  $W$ ). That allows us to simplify the complete LSA condition by setting  $K_I = 0$  ( $W \rightarrow +\infty$ ), in that case the coefficients in Equation 3.9

becomes:

$$s_0 = 0 \quad (3.51)$$

$$s_1 = K_{II}(f(A_w - B_w) + (A_s - B_s))/v_{ss} \quad (3.52)$$

$$s_2 = ((A_w - B_w)(A_s - B_s) + K_{II}(f(A_w D_{cw} + (A_w - B_w)D_{cs}) + (A_s D_{cs} + (A_s - B_s)D_{cw}))) / v_{ss}^2 \quad (3.53)$$

$$s_3 = (A_w A_s (D_{cw} + D_{cs}) - A_w B_s D_{cw} - A_s B_w D_{cs} + (A_s + f A_w) D_{cw} D_{cs} K_{II}) / v_{ss}^3 \quad (3.54)$$

$$s_4 = A_w A_s D_{cw} D_{cs} / v_{ss}^4 \quad (3.55)$$

Instability boundary Equation 3.18 becomes

$$s_1(s_4 s_1 - s_2 s_3) = 0 \quad (3.56)$$

Hence, either

$$s_1 = 0 \quad (3.57)$$

or

$$s_1 s_4 = s_2 s_3 \quad (3.58)$$

The first condition (Equation 3.57) defines the velocity-neutral limit of the T-instability boundary (when  $W \rightarrow +\infty$ ), while the latter condition (Equation 3.58) properly defines the P-instability boundary.

Putting back the coefficients with physical properties into Equation 3.58 yields a quadratic equation for  $K_{II}$ :

$$C_0 K_{II}^2 + C_1 K_{II} + C_2 = 0 \quad (3.59)$$

where

$$C_0 = (f(A_w D_{cw} + (A_w - B_w)D_{cs}) + (A_s D_{cs} + (A_s - B_s)D_{cw}))(A_s + f A_w) D_{cw} D_{cs} \quad (3.60)$$

$$C_1 = (A_w - B_w)(A_s - B_s)(A_s + f A_w) D_{cw} D_{cs} + (f(A_s D_{cw} + (A_w - B_w)D_{cs}) + (A_s D_{cs} + (A_s - B_s)D_{cw}))(A_w D_{cw}(A_s - B_s) + A_s D_{cs}(A_w - B_w)) - (f(A_w - B_w) + (A_s - B_s))A_w A_s D_{cw} D_{cs} \quad (3.61)$$

$$C_2 = (A_w - B_w)(A_s - B_s)(A_w D_{cw}(A_s - B_s) + A_s D_{cs}(A_w - B_w)) \quad (3.62)$$

Equation 3.59 has two solutions:

$$K_{II} = \frac{-C_1}{2C_0} \left( 1 \pm \sqrt{1 - \frac{4C_0 C_2}{C_1^2}} \right) \quad (3.63)$$

Numerical examination shows the physical solution is the one with "+" sign:

$$K_{II} = \frac{-C_1}{2C_0} \left( 1 + \sqrt{1 - \frac{4C_0C_2}{C_1^2}} \right) \quad (3.64)$$

Equation 3.64 precisely defines the P-instability boundary in closed form, and is in perfect match with the complete LSA solution.

### Simplified approximation of the P-instability boundary

Similar to how we derive the approximation for the T-instability boundary in the previous subsection, we manipulate Equation 3.64 to further simplify the P-instability boundary equation. Numerical evaluation shows that, heterogeneous faults with various parameter settings in our study, always satisfy:

$$C_1^2 \gg C_0C_2 \quad (3.65)$$

First-order Taylor expansion of Equation 3.64 with respect to  $4C_1^2/(C_0C_2)$  gives

$$K_{II} \approx -C_1/C_0 \quad (3.66)$$

that is

$$K_{II} \approx \frac{A_w(B_s - A_s)/D_{cs} + A_s(B_w - A_w)/D_{cw}}{A_s + fA_w} - \frac{(A_w - B_w)(A_s - B_s)(A_s + fA_w) - (f(A_w - B_w) + (A_s - B_s))A_wA_s}{(f(A_wD_{cw} + (A_w - B_w)D_{cs})/D_{cw}D_{cs} + (A_sD_{cs} + (A_s - B_s)D_{cw}))(A_s + fA_w)} \quad (3.67)$$

Numerical study shows that the 1<sup>st</sup> term in Equation 3.67 is at least one order of magnitude larger than the 2<sup>nd</sup> term, so we can approximate and further simplify the P-instability boundary equation by ignoring the 2<sup>nd</sup> term:

$$K_{II} \approx \frac{A_w(B_s - A_s)/D_{cs} + A_s(B_w - A_w)/D_{cw}}{A_s + fA_w} \quad (3.68)$$

The P-instability boundary approximated by Equation 3.68 matches surprisingly good with the complete LSA results with all parameter settings we have explored (Figure 3.9 and 3.10).

Equation 3.68 is in the form simple enough that we can examine the P-instability boundary directly. It is clear that when  $D_{cw}$  is small, Equation 3.68 reduces into

$$K_{II} \approx \frac{B_w - A_w}{D_{cw}} \frac{A_s}{A_s + fA_w} \quad (3.69)$$

the 1<sup>st</sup> term in Equation 3.69 is exactly the critical stiffness of an isolated VW block, while the 2<sup>nd</sup> term approximates how the existence of VS block affects the VW block. This explains why the P-boundary is not vertical  $\beta = 1$  in the  $\alpha - \beta$  system.

### 3.5 Discussion and conclusions

We have presented a systematic numerical and theoretical study on the stability of slip on faults with regular alternation of frictional properties, with contrasting material competences and effective normal stress. Our results paint a comprehensive picture of how the stability of a heterogeneous fault is affected by the relative proportion of strong and weak materials, and by their relative strength and other frictional properties. These results help us gain insight on natural slip processes over a wide range of spatial-temporal scales and have implications for earthquake hazard estimation. In particular, a fault composed in its majority of material with stable properties can actually be unstable, and a stable fault can become unstable due to time-dependent changes of asperity/matrix strength contrast.

The proportion of strong and weak materials in a fault zone is controlled by structural and geometrical properties such as the distribution of asperity sizes and the spacing between asperities. These properties may evolve through mechanical processes like asperity fragmentation and dispersion driven by fault zone shearing, and physico-chemical processes like alteration assisted by fault zone fluids. These processes typically operate on time scales much longer than an earthquake cycle and on length scales comparable to the seismogenic width. An evolution of asperities controlled by the irreversible process of fragmentation and shearing would lead to monotonically decreasing asperity sizes and increasing asperity spacing as a function of depth. This would be inconsistent with the fact that seismic slip events within otherwise aseismic slip areas, such as (Very) Low Frequency Earthquakes in Japan, are observed both in shallow and deep environments in subduction zones. Furthermore, it is not a viable candidate mechanism for depth-dependent slip behavior on strike-slip faults.

In contrast, the relative strength between asperities and matrix may change over short spatial-temporal scales and non-monotonically with depth. Depth-dependent changes of temperature and effective normal stress are obvious factors that can affect the strong and weak materials differently. Another plausible factor, which can further introduce heterogeneity along-trike and over shorter scales, are changes of the fluid pressure difference between matrix and asperities in a fault zone with hydraulically sealed asperities. Pressure in the permeable matrix can increase with

depth due to dehydration, without affecting the pressure inside hydraulically sealed asperities. On the other hand, laboratory experiments of VW/VS spring block, e.g. [Saffer and Marone \(2003\)](#) find that natural illite shale exhibits only VS behavior and no strong velocity-dependent friction over a large range of normal stress and loading velocity. Thus the smectite-illite transition alone does not support the seismic-aseismic transition in subduction zones, and an additional mechanism is required. Our model of depth-dependent asperity/matrix fluid pressure contrast is a mechanism to consider.

In cases when differential pore pressure is already present, a uniform change in normal stress or pore pressure can cause a large change in the asperity/matrix strength contrast. Possible scenarios of temporal relative strength change include: transient surface or tidal loadings that affects normal stress; slow pressure build-up in the matrix; fluid injection may also directly affect pore pressure conditions; sudden decrease of fluid pressure in asperities due to seal breaking; fault valving mechanism during earthquakes changes the local permeability of fault materials and ultimately results in fluctuation of pore pressure over times scale of earthquake cycles. In particular, since the depths at which slow slip and tremor occur have been inferred to have very high pore pressure, a small uniform increase of pore pressure can lead to large fluctuation in asperity/matrix relative strength. In addition, if the change of relative strength destabilizes the slow slip zone it could facilitate the nucleation of regular earthquakes ([Figure 3.3](#)).

We found that a monotonic increase of pore pressure can lead a fault with micro-seismic activity to a large rupture with an intermediate period of stable slip ([Figure 3.3](#) at intermediate  $\beta$ ). This is reminiscent of the seismic quiescence, i.e. a period of greatly reduced seismicity, observed before certain large earthquakes ([Habermann 1988](#); [Kanamori 1981](#); [Sobolev 2011](#)).

The model presented here is a promising framework to understand the full spectrum of slow-to-fast earthquakes. [Figure 3.11](#) shows the conceptually the transitions of fault behavior of a subduction fault as a function of depth (orange curve in the left figure). Near the surface the relative strength between VW and VS segments is low, so the fault is stable. The relative strength increases with increasing depth and the fault transits into unstable and slow events like shallow SSE, LFE and tremors. The relative strength keeps increasing at seismogenic depth and the fault transits from slow earthquakes to fast earthquakes, including regular earthquakes with various magnitude and megathrust earthquakes rupturing the whole seismogenic zone.

Then the relative strength starts to decrease and the fault behavior transits back to slow earthquakes again, producing deep episodic tremor and slow-slip event. The relative strength continues decreasing with depth and the fault eventually transit into steady-slip (stable). Alternatively if the individual criticalness of the VW asperity increases (possible mechanism includes decrease of  $D_c$  or increase of effective normal stress of the VW asperity) it may enter the regime of background tremor activities (spontaneous failure of individual VW asperities), as indicated by the dotted orange curve in [Figure 3.11](#).

Our study serves as a building block for models of episodic tremor and slow-slip that emphasize the role of fault heterogeneity. In particular, results reported here of the conditions required for "T-instabilities" provided guidance on how to set the asperity/matrix relative strength in the models of slow slip and tremor developed in [Luo and Ampuero \(2017\)](#). Such models quantitatively reproduced observations of slow slip and tremor migration patterns in Cascadia and led to a new mechanism of slow slip driven by tremors.

### 3.6 Appendices

#### Derivation of governing equations

In this section we will derive the stress balance governing equations in discrete media with VS/VW ratio of integer values, and extend it to any arbitrary VW and VS ratio.

The VW/VS mixed material in QDYN are arranged in a periodical pattern, with one (1) VW block (#0, thereafter referred with foot note  $x_0$ ) and  $m$  (# $i = 1, 2, \dots, m$ , thereafter referred with foot note  $x_i$ ) VS blocks.

We define the slip deficit  $\delta_i$  of the  $i$ -th block as:

$$\delta_i = v_{ss}t - d_i \quad (\text{A.1})$$

where  $v_{ss}$  is the plate velocity, and  $d_i$  is the slip of the  $i$ -th block. Under static approximation, the stress ( $\tau$ ) of each block is determined by the slip deficit of every block in the system (stress balance):

$$\tau_i = K_{ij}\delta_j \quad (\text{A.2})$$

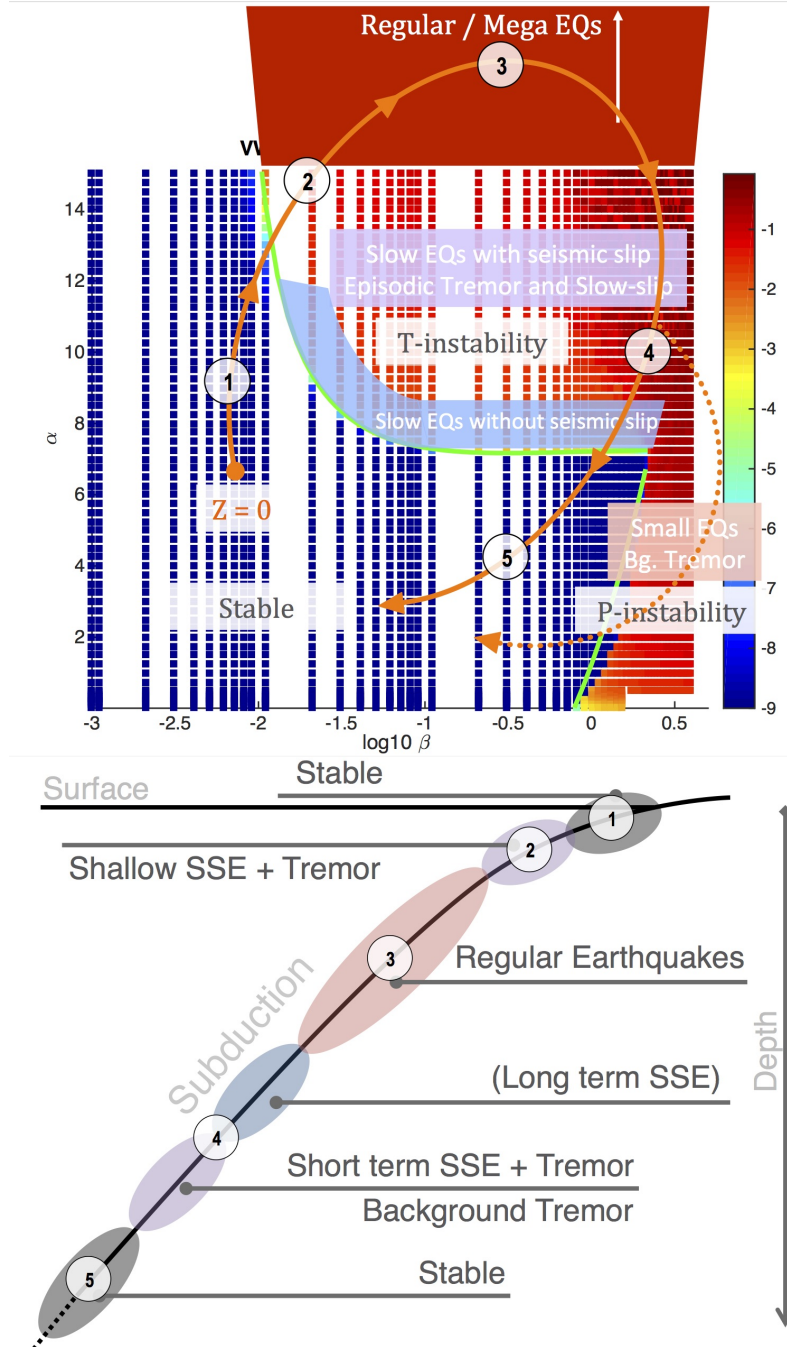


Figure 3.11: Concept of fast-to-slow earthquakes transition of subduction zone.

$K_{ij}$  is the stress transfer coefficient matrix (stress kernel) of the system.

With periodic boundary condition, it has the following properties:

$$K_{ij} = K_{|i-j|} \quad \text{symmetric Toeplitz structure.} \quad (\text{A.3})$$

$$\sum_{i=0}^m K_i = K_w \quad \text{stiffness of uniform slip.} \quad (\text{A.4})$$

$$K_{m+1-i} = K_i \quad \text{periodicity, i.e. } K_1 = K_m, K_2 = K_{m-1} \dots \quad (\text{A.5})$$

where  $K_w$  is the fault stiffness with width  $W$ .

then Equation (A.1) gives:

$$\tau_0 = K_0\delta_0 + K_1\delta_1 + K_2\delta_2 + \dots + K_3\delta_{m-2} + K_2\delta_{m-1} + K_1\delta_m \quad (\text{A.6})$$

$$\tau_1 = K_1\delta_0 + K_0\delta_1 + K_1\delta_2 + \dots + K_4\delta_{m-2} + K_3\delta_{m-1} + K_2\delta_m \quad (\text{A.7})$$

$$\tau_2 = K_2\delta_0 + K_1\delta_1 + K_0\delta_2 + \dots + K_5\delta_{m-2} + K_4\delta_{m-1} + K_3\delta_m \quad (\text{A.8})$$

...

$$\tau_{m-1} = K_2\delta_0 + K_3\delta_1 + K_4\delta_2 + \dots + K_1\delta_{m-2} + K_0\delta_{m-1} + K_1\delta_m \quad (\text{A.9})$$

$$\tau_m = K_1\delta_0 + K_2\delta_1 + K_3\delta_2 + \dots + K_2\delta_{m-2} + K_1\delta_{m-1} + K_0\delta_m \quad (\text{A.10})$$

If we assume uniform slip  $\delta_{v_s}$  in the VS part:

$$\delta_1 = \delta_2 = \dots = \delta_m = v_{ss}t - \delta_{v_s} \quad (\text{A.11})$$

then stress in the VW segment is

$$\tau_{vw} = \tau_0 = K_0(v_{ss}t - \delta_{vw}) + (K_w - K_0)(v_{ss}t - \delta_{v_s}) \quad (\text{A.12})$$

Rearrange into

$$\tau_{vw} = K_w(v_{ss}t - \delta_{vw}) + (K_w - K_0)(\delta_{vw} - \delta_{v_s}) \quad (\text{A.13})$$

On the other hand, we define average stress  $\tau_{v_s}$  in VS region as

$$\tau_{v_s} = (\tau_1 + \tau_2 + \tau_3 + \dots + \tau_m)/m \quad (\text{A.14})$$

Using the following property of periodic kernels Equation (A.4), we have

$$\sum_{i=0}^m \tau_i = \sum_{i=0}^m K_i \delta_i = K_w \sum_{i=0}^m \delta_i \quad (\text{A.15})$$

that is

$$\tau_{vw} + m\tau_{v_s} = K_w(v_{ss}t - \delta_{vw} + m(v_{ss}t - \delta_{v_s})) \quad (\text{A.16})$$

Combining this Equation (A.16) and Equation (A.13) we get:

$$\tau_{v_s} = K_w(v_{ss}t - \delta_{v_s}) + (K_w - K_0)/m \cdot (\delta_{v_s} - \delta_{vw}) \quad (\text{A.17})$$

Equation (A.13) and Equation (A.17) defines the stress balance governing equations in discrete media, with VS/VW ratio of integer values.

Further more, we make the assumption that the governing equation Equation (A.13)

and Equation (A.17) can be extended into any arbitrary VW and VS area ratio  $1/m = f$ . Then Equation (A.13) and Equation (A.17) become

$$\tau_w = K_I(v_{sst} - \delta_w) + K_{II}(\delta_s - \delta_w) \quad (\text{A.18})$$

$$\tau_s = K_I(v_{sst} - \delta_s) + fK_{II}(\delta_w - \delta_s) \quad (\text{A.19})$$

where

$f$  is the area ratio between the VW and VS block.

$K_I = K_w = \pi GW$  is stiffness of plate loading

$K_{II} = K_0 - K_w$  is stiffness of block interaction

$K_0$  is self-stiffness of VW block in space domain

Equation (A.18) and Equation (A.19) then defines the stress balance governing equations in discrete media, of any arbitrary VW/VS ratio.

### Approximate account for fault width via a 2.5D model

In the previous section of Appendix we have discussed about the stress transfer equation Equation (A.2). (Ampuero (2002), Chapter 2, Appendix 2C) had discussed about the numerical recipe for a infinite 1D fault embedded in 2D homogeneous media. The stress transfer kernel for such a fault with period  $L$  in Mode II anti-plane deformation and in space domain, after discretization with even spacing (uniform cell size  $\Delta x$ ), take the form of:

$$K_i = \frac{\pi G}{L} \frac{\sin(\pi/N)}{\sin(\frac{i-1/2}{N}) \cdot \sin(\frac{i+1/2}{N})} \quad (\text{A.20})$$

where  $K_i$  is the stress transfer kernel of fault cells with normalized distance  $i$ ,  $i$  is the distance between two fault cells normalized by cell size  $\Delta x$ ,  $N$  is total number of fault cells  $N = L/\Delta x$ .

On the other hand, in spectral domain, Equation (A.20) becomes :

$$k_j = \frac{\pi G}{L} \cdot j \quad (\text{A.21})$$

where  $j$  is the wave number.

To mimic the effect of finite fault width  $W$ , as if the fault is loaded by steady displacement at distance  $W$  from the fault, we replace Equation (A.21) with approximation:

$$k_j = \frac{\pi G}{L} \cdot \sqrt{j^2 + (\frac{L}{W})^2} \quad (\text{A.22})$$

Equation (A.22) reduces into Equation (A.21) while  $W \gg L$ .

### Linear stability analysis of two-degree-of-freedom periodic spring-block system

Continuing from the governing equations Equation (A.18) and Equation (A.19), define  $\sigma_i$  as effective normal stress,  $F$  as friction coefficient,  $E$  as the evolutionary law of the rate-and-state friction,  $\theta$  as the state variables of the rate-and-state friction:

$$\tau_i = \sigma_i F(\theta_i, v_i) = \sigma_i F_i \quad (\text{A.23})$$

$$\dot{\theta}_i = E(\theta_i, v_i) = E_i \quad (\text{A.24})$$

Small perturbation near steady-state (marked with \*) yields:

$$\tau_i^* = \sigma_i (F_{iv} v_i^* + F_{i\theta} \theta_i^*) \quad (\text{A.25})$$

$$\dot{\theta}_i = E_{iv} v_i^* + E_{i\theta} \theta_i^* \quad (\text{A.26})$$

Equation (A.25) Can also be written as

$$\theta_i^* = (\tau_i^* / \sigma_i - F_{iv} v_i^*) / F_{i\theta} \quad (\text{A.27})$$

Take time derivative of Equation (A.27) and combine with Equation (A.26) yields

$$\dot{\tau}_i^* = \sigma_i F_{iv} \dot{v}_i^* + \sigma_i F_{i\theta} (E_{iv} v_i^* + E_{i\theta} \theta_i^*) \quad (\text{A.28})$$

Substitute  $\theta_i^*$  in Equation (A.28) with Equation (A.27) gives

$$\dot{\tau}_i^* = \sigma_i F_{iv} \dot{v}_i^* + \sigma_i (F_{i\theta} E_{iv} - F_{iv} E_{i\theta}) v_i^* + E_{i\theta} \tau_i^* \quad (\text{A.29})$$

Take time derivative of Equation (A.29) yields

$$\ddot{\tau}_i^* = \sigma_i F_{iv} \ddot{v}_i^* + \sigma_i (F_{i\theta} E_{iv} - F_{iv} E_{i\theta}) \dot{v}_i^* + E_{i\theta} \dot{\tau}_i^* \quad (\text{A.30})$$

On the other hand, take time derivative and small perturbation near steady-state of Equation (A.18) gives

$$\dot{\tau}_w^* = -K_I v_w^* + K_{II} (v_s^* - v_w^*) \quad (\text{A.31})$$

Take time derivative of Equation (A.31):

$$\ddot{\tau}_w^* = -K_I \dot{v}_w^* + K_{II} (\dot{v}_s^* - \dot{v}_w^*) \quad (\text{A.32})$$

Take  $i = w$  (for VW block), substitute  $\dot{\tau}_w^*$  and  $\ddot{\tau}_w^*$  in Equation (A.30) with Equation (A.31) and Equation (A.32) gives

$$\sigma_w F_{wv} \ddot{v}_w^* + (\sigma_w F_{w\theta} E_{wv} - \sigma_w F_{wv} E_{w\theta} + K_I + K_{II}) \dot{v}_w^* - K_{II} \dot{v}_s^* - (K_I + K_{II}) E_{w\theta} v_w^* + K_{II} E_{w\theta} v_s^* = 0 \quad (\text{A.33})$$

Similarly for  $i = s$  (for VS block),

$$\dot{\tau}_s^* = -K_I v_s^* + f K_{II} (v_w^* - v_s^*) \quad (\text{A.34})$$

$$\ddot{\tau}_s^* = -K_I \dot{v}_s^* + f K_{II} (\dot{v}_w^* - \dot{v}_s^*) \quad (\text{A.35})$$

$$\sigma_s F_{sv} \ddot{v}_s^* + (\sigma_s F_{s\theta} E_{sv} - \sigma_s F_{sv} E_{s\theta} + K_I + f K_{II}) \dot{v}_s^* - f K_{II} \dot{v}_w^* - (K_I + f K_{II}) E_{s\theta} v_s^* + f K_{II} E_{s\theta} v_w^* = 0 \quad (\text{A.36})$$

Equation (A.33) and Equation (A.36) are second order coupled ODE with general form:

$$\bar{M}_2 \ddot{\vec{v}} + \bar{M}_1 \dot{\vec{v}} + \bar{M}_0 \vec{v} = \vec{0} \quad (\text{A.37})$$

Attempt solution

$$\vec{v} = \vec{v}_c e^{\lambda t} \quad (\text{A.38})$$

then Equation (A.37) becomes

$$\begin{aligned} Q(\lambda) = & \begin{pmatrix} F_{wv} \sigma_w & 0 \\ 0 & F_{sv} \sigma_s \end{pmatrix} \lambda^2 \\ & + \begin{pmatrix} \sigma_w F_{w\theta} E_{wv} - \sigma_w F_{wv} E_{w\theta} + K_I + K_{II} & -K_{II} \\ -f K_{II} & \sigma_s F_{s\theta} E_{sv} - \sigma_s F_{sv} E_{s\theta} + K_I + f K_{II} \end{pmatrix} \lambda \\ & + \begin{pmatrix} -(K_I + K_{II}) E_{w\theta} v_w^* & K_{II} E_{w\theta} \\ f K_{II} E_{s\theta} & -(K_I + f K_{II}) E_{s\theta} \end{pmatrix} \end{aligned} \quad (\text{A.39})$$

On the one hand, with rate-and-state friction:

$$F = \mu_0 + a \ln \frac{v}{v_{ss}} + b \ln \frac{v_{ss} \theta}{D_c} \quad (\text{A.40})$$

take the derivatives of  $v$  and  $\theta$  of Equation (A.40) at steady-state:

$$F_{iv} = \frac{a_i}{v_{ss}} \quad (\text{A.41})$$

$$F_{i\theta} = \frac{b_i v_{ss}}{D_{ci}} \quad (\text{A.42})$$

On the other hand, with state evolution laws:

Slip law:

$$\dot{\theta} = -\frac{v\theta}{D_c} \ln \frac{v\theta}{D_c} \quad (\text{A.43})$$

Aging law:

$$\dot{\theta} = 1 - \frac{v\theta}{D_c} \quad (\text{A.44})$$

Under both laws, derivatives of  $v$  and  $\theta$  at steady-state gives:

$$E_{iv} = -\frac{1}{v_{ss}} \quad (\text{A.45})$$

$$E_{i\theta} = -\frac{v_{ss}}{D_{ci}} \quad (\text{A.46})$$

Substitute  $F$ ,  $E$  expressions in Equation (A.39) with Equation (A.41), (A.42), (A.45) and (A.46) we have:

$$\begin{aligned} Q(\lambda) = & \begin{pmatrix} a_w \sigma_w / v_{ss} & 0 \\ 0 & a_s \sigma_s / v_{ss} \end{pmatrix} \lambda^2 \\ & + \begin{pmatrix} (a_w - b_w) \sigma_w / D_{cw} + K_I + K_{II} & -K_{II} \\ -f K_{II} & (a_s - b_s) \sigma_s / D_{cs} + K_I + f K_{II} \end{pmatrix} \lambda \\ & + \begin{pmatrix} (K_I + K_{II}) v_{ss} / D_{cw} & -K_{II} v_{ss} / D_{cw} \\ -f K_{II} v_{ss} / D_{cs} & (K_I + f K_{II}) v_{ss} / D_{cs} \end{pmatrix} \end{aligned} \quad (\text{A.47})$$

System is unstable (evolves under smaller perturbation at steady-state) if the real part of at least one  $\lambda$  is positive of the determinant of Equation (A.47):

$$\det(Q(\lambda)) = 0 \mid \exists \operatorname{Re}(\lambda) > 0 \quad (\text{A.48})$$

Solving for condition Equation (A.48) gives the linear stability of any given system.

## References

- Ampuero, J. P. (2002), “Etude physique et numérique de la nucléation des séismes”. *PhD Thesis, University of Paris VII, France.*
- Ampuero, J. P. and A. M. Rubin (2008), “Earthquake nucleation on rate and state faults—Aging and slip laws”. *Journal of Geophysical Research: Solid Earth*, 113 (B1).
- Avouac, J. P., L. Meng, S. Wei, T. Wang, and J. P. Ampuero (2015), “Lower edge of locked Main Himalayan Thrust unzipped by the 2015 Gorkha earthquake”. *Nature Geoscience*, 8 (9), pp. 708–711.
- Bebout, G. E. and M. D. Barton (2002), “Tectonic and metasomatic mixing in a high-T, subduction-zone mélange—insights into the geochemical evolution of the slab–mantle interface”. *Chemical Geology*, 187 (1), pp. 79–106.
- Bhattacharya, P., A. M. Rubin, E. Bayart, H. M. Savage, and C. Marone (2015), “Critical evaluation of state evolution laws in rate and state friction: Fitting large velocity steps in simulated fault gouge with time-, slip-, and stress-dependent constitutive laws”. *Journal of Geophysical Research: Solid Earth*, 120 (9), pp. 6365–6385.
- Chen, T. and N. Lapusta (2009), “Scaling of small repeating earthquakes explained by interaction of seismic and aseismic slip in a rate and state fault model”. *Journal of Geophysical Research: Solid Earth*, 114 (B1).
- Dieterich, J. H. (1979), “Modeling of rock friction: 1. Experimental results and constitutive equations”. *Journal of Geophysical Research: Solid Earth*, 84 (B5), pp. 2161–2168.
- Dublanchet, P., P. Bernard, and P. Favreau (2013), “Interactions and triggering in a 3-D rate-and-state asperity model”. *Journal of Geophysical Research: Solid Earth*, 118 (5), pp. 2225–2245.
- Fagereng, Å. (2011), “Fractal vein distributions within a fault-fracture mesh in an exhumed accretionary mélange, Chrystalls Beach Complex, New Zealand”. *Journal of Structural Geology*, 33 (5), pp. 918–927.
- Fagereng, Å. and A. F. Cooper (2010), “The metamorphic history of rocks buried, accreted and exhumed in an accretionary prism: an example from the Otago Schist, New Zealand”. *Journal of Metamorphic Geology*, 28 (9), pp. 935–954.
- Fagereng, Å. and R. H. Sibson (2010), “Mélange rheology and seismic style”. *Geology*, 38 (8), pp. 751–754.
- Fagereng, Å. and S. A. den Hartog (2017), “Subduction megathrust creep governed by pressure solution and frictional-viscous flow”. *Nature Geoscience*, 10 (1), pp. 51–57.
- Glendinning, P. (1994), *Stability, instability and chaos: an introduction to the theory of nonlinear differential equations*. Vol. 11. Cambridge university press.

- Gu, Y. and T. Wong (1994), “Nonlinear Dynamics of the Transition from Stable Sliding to Cyclic Stick-Slip in Rock”. *Nonlinear Dynamics and Predictability of Geophysical Phenomena*, pp. 15–35.
- Habermann, R. E. (1988), “Precursory seismic quiescence: past, present, and future”. *Pure and applied Geophysics*, 126 (2), pp. 279–318.
- Hawthorne, J. C. and A. M. Rubin (2013), “Laterally propagating slow slip events in a rate and state friction model with a velocity-weakening to velocity-strengthening transition”. *Journal of Geophysical Research: Solid Earth*, 118 (7), pp. 3785–3808.
- Healy, J. H., W. W. Rubey, D. T. Griggs, and C. B. Raleigh (1968), “The denver earthquakes”. *Science*, 161 (3848), pp. 1301–1310.
- Hillers, G. and S. A. Miller (2007), “Dilatancy controlled spatiotemporal slip evolution of a sealed fault with spatial variations of the pore pressure”. *Geophysical Journal International*, 168 (1), pp. 431–445.
- Hillers, G., Y. Ben-Zion, and P. M. Mai (2006), “Seismicity on a fault controlled by rate-and state-dependent friction with spatial variations of the critical slip distance”. *Journal of Geophysical Research: Solid Earth*, 111 (B1).
- Hillers, G., P. M. Mai, Y. Ben-Zion, and J. P. Ampuero (2007), “Statistical properties of seismicity of fault zones at different evolutionary stages”. *Geophysical Journal International*, 169 (2), pp. 515–533.
- Ide, S., G. C. Beroza, D. R. Shelly, and T. Uchide (2007), “A scaling law for slow earthquakes”. *Nature*, 447 (7140), p. 76.
- Kanamori, H. (1981), “The nature of seismicity patterns before large earthquakes”. *Earthquake Prediction*, pp. 1–19.
- Kocharyan, G. G., V. A. Novikov, A. A. Ostapchuk, and D. V. Pavlov (2016), “A study of different fault slip modes governed by the gouge material composition in laboratory experiments”. *Geophysical Journal International*, ggw409.
- Lay, T., H. Kanamori, C. J. Ammon, K. D. Koper, A. R. Hutko, L. Ye, H. Yue, and T. M. Rushing (2012), “Depth-varying rupture properties of subduction zone megathrust faults”. *Journal of Geophysical Research: Solid Earth*, 117 (B4).
- Luo, X. and G. Vasseur (2002), “Natural hydraulic cracking: numerical model and sensitivity study”. *Earth and Planetary Science Letters*, 201 (2), pp. 431–446.
- Luo, Y. and J. P. Ampuero (2017), “Tremor migration patterns and the collective behavior of deep asperities mediated by creep”.
- Luo, Y., J. P. Ampuero, P. Galvez, M. Ende, and B. Idini (2017a), *QDYN: a Quasi-DYNAMIC earthquake simulator (v1.1)*. DOI: 10.5281/zenodo.322459. URL: <https://doi.org/10.5281/zenodo.322459>.

- Luo, Y., J. P. Ampuero, K. Miyakoshi, and K. Irikura (2017b), “Surface Rupture Effects on Earthquake Moment-Area Scaling Relations”. *Pure and Applied Geophysics*, pp. 1–12.
- Ma, S. and C. He (2001), “Period doubling as a result of slip complexities in sliding surfaces with strength heterogeneity”. *Tectonophysics*, 337 (1), pp. 135–145.
- Marone, C. (1998), “Laboratory-derived friction laws and their application to seismic faulting”. *Annual Review of Earth and Planetary Sciences*, 26 (1), pp. 643–696.
- Marone, C. and B. Kilgore (1993), “Scaling of the critical slip distance for seismic faulting with shear strain in fault zones”. *Nature*, 362 (6421), pp. 618–621.
- Meneghini, F., G. Di Toro, C. D. Rowe, J. C. Moore, A. Tsutsumi, and A. Yamaguchi (2010), “Record of mega-earthquakes in subduction thrusts: the black fault rocks of Pasagshak Point (Kodiak Island, Alaska)”. *Geological Society of America Bulletin*, 122 (7-8), pp. 1280–1297.
- Meng, L., A. Inbal, and J. P. Ampuero (2011), “A window into the complexity of the dynamic rupture of the 2011 Mw 9 Tohoku-Oki earthquake”. *Geophysical Research Letters*, 38 (7).
- Osborne, M. J. and R. E Swarbrick (1997), “Mechanisms for generating overpressure in sedimentary basins: a reevaluation”. *AAPG bulletin*, 81 (6), pp. 1023–1041.
- Parsons, T. (2005), “A hypothesis for delayed dynamic earthquake triggering”. *Geophysical Research Letters*, 32 (4).
- Perfettini, H. and J. P. Ampuero (2008), “Dynamics of a velocity strengthening fault region: Implications for slow earthquakes and postseismic slip”. *Journal of Geophysical Research: Solid Earth*, 113 (B9).
- Perfettini, H., M. Campillo, and I. Ionescu (2003), “On the scaling of the slip weakening rate of heterogeneous faults”. *Journal of Geophysical Research: Solid Earth*, 108 (B9).
- Rice, J. R. (1993), “Spatio-temporal complexity of slip on a fault”. *Journal of Geophysical Research: Solid Earth*, 98 (B6), pp. 9885–9907.
- Rittenhouse, G. (1971), “Mechanical compaction of sands containing different percentages of ductile grains: a theoretical approach”. *Bulletin - American Association of Petroleum Geologists*, 55 (1), pp. 92–96.
- Roberts, S. J. and J. A. Nunn (1995), “Episodic fluid expulsion from geopressed sediments”. *Marine and Petroleum Geology*, 12 (2), 195IN1203–202IN3204.
- Rubin, A. M. and J. P. Ampuero (2005), “Earthquake nucleation on (aging) rate and state faults”. *Journal of Geophysical Research: Solid Earth*, 110 (B11).
- Ruina, A. (1983), “Slip instability and state variable friction laws”. *Journal of Geophysical Research: Solid Earth*, 88 (B12), pp. 10359–10370.

- Saffer, D. M. and C. Marone (2003), “Comparison of smectite-and illite-rich gouge frictional properties: application to the updip limit of the seismogenic zone along subduction megathrusts”. *Earth and Planetary Science Letters*, 215 (1), pp. 219–235.
- Scuderi, M. M. and C. Collettini (2016), “The role of fluid pressure in induced vs. triggered seismicity: Insights from rock deformation experiments on carbonates”. *Scientific reports*, 6, p. 24852.
- Sibson, R. (1992), “Implications of fault-valve behaviour for rupture nucleation and recurrence”. *Tectonophysics*, 211 (1-4), pp. 283–293.
- (2014), “Earthquake rupturing in fluid-overpressured crust: how common?” *Pure and Applied Geophysics*, 171 (11), pp. 2867–2885.
- Sibson, R., F. Robert, and K. H. Poulsen (1988), “High-angle reverse faults, fluid-pressure cycling, and mesothermal gold-quartz deposits”. *Geology*, 16 (6), pp. 551–555.
- Skarbak, R. M., A. W. Rempel, and D. A. Schmidt (2012), “Geologic heterogeneity can produce aseismic slip transients”. *Geophysical Research Letters*, 39 (21).
- Sobolev, G. (2011), “Seismic Quiescence and Activation”. *Encyclopedia of Solid Earth Geophysics*. Springer, pp. 1178–1184.
- Tse, S. T. and J. R. Rice (1986), “Crustal earthquake instability in relation to the depth variation of frictional slip properties”. *Journal of Geophysical Research: Solid Earth*, 91 (B9), pp. 9452–9472.
- Venkataraman, A. and H. Kanamori (2004), “Observational constraints on the fracture energy of subduction zone earthquakes”. *Journal of Geophysical Research: Solid Earth*, 109 (B5).
- Viesca, R. C. (2016), “Stable and unstable development of an interfacial sliding instability”. *Physical Review E*, 93 (6), p. 060202.
- Wech, A. G. and K. C. Creager (2011), “A continuum of stress, strength and slip in the Cascadia subduction zone”. *Nature Geoscience*, 4 (9), p. 624.
- Yabe, S. and S. Ide (2017), “Slip-behavior transitions of a heterogeneous linear fault”. *Journal of Geophysical Research: Solid Earth*, 122 (1), pp. 387–410.

*Chapter 4***TREMOR MIGRATION PATTERNS AND THE COLLECTIVE BEHAVIOR OF DEEP ASPERITIES MEDIATED BY CREEP****Abstract**

Slow-slip events (SSE) and non-volcanic tremors have revealed a broad spectrum of earthquake behavior, involving entangled seismic and aseismic slip, and offer a unique window into fault mechanics at the bottom of seismogenic zones. A hierarchy of migration patterns of tremors has been observed in the Cascadia subduction zone, including large-scale along-strike tremor propagation and Rapid Tremor Reversals (RTR) migrating in opposite directions with much higher propagation speeds. Here we show that these tremor migration patterns can be reproduced by two end-member models of a fault with heterogeneous mechanical properties, composed of competent asperities embedded in a more frictionally stable, incompetent matrix. In the SSE-driven-tremor model, SSEs are spontaneously generated by the matrix, even in absence of seismic asperities, and drive tremor. In the tremor-driven-SSE model the matrix is stable, it slips steadily in absence of asperities, and SSEs result from the collective behavior of tremor asperities interacting via transient creep in the form of local afterslip fronts. We study these two end-member models through 2D quasi-dynamic multi-cycle simulations of faults governed by rate-and-state friction with heterogeneous frictional properties and effective normal stress, using the earthquake simulation software QDYN (Luo et al. 2017). In both models, tremor migration patterns emerge from interactions between asperities mediated by creep transients. The models successfully reproduce forward tremor propagation and RTRs, as well as various other observed tremor migration patterns, without the need to finely tune model parameters. Our modeling results suggest that, in contrast to a common view, SSE could be a result of tremor activity. Also, the hierarchical pattern of tremor migrations provides general constraints on fault zone rheology, and the location of RTRs and other tremor patterns might shed light on the finer scale spatial variability of fault properties. We also find that, despite important interactions between asperities, tremor activity rates are proportional to the underlying aseismic slip rate, supporting an approach to estimate SSE properties with high spatial-temporal resolutions via tremor activity.

## 4.1 Introduction

Slow-slip events (SSEs) and non-volcanic tremors (NVTs) discovered in the last decade (Rogers and Dragert 2003) have greatly expanded the spectrum of observed earthquake behavior (Beroza and Ide 2011; Gomberg 2010; Hawthorne and Rubin 2010; Ide et al. 2007a; Peng and Gomberg 2010). SSEs are aseismic slip transients with a small slip rate (few orders of magnitude larger than the plate loading rate, well below seismic slip rate), they evolve more slowly and have a much longer duration than regular earthquakes, and have been mostly observed near the deep seismic-aseismic transition (30 to 50 km) below the conventional seismogenic zone depth. Tremors are emergent and continuous seismic signals, with relatively small amplitude and energy concentrated at frequencies between 1 and 10 Hz, lower than regular earthquakes of comparable magnitudes (whose energy extends above 10 Hz). Tremors are often composed of multiple Low Frequency Earthquakes (LFEs), apparently repeated failures of a same (or closely located) fault asperity (e.g. Shelly et al. 2007). Tremors are often organized in swarms that migrate. An imbricated hierarchy of tremor migration patterns has been observed in the Cascadia subduction zone (Figure 4.1) during each recurring episodic tremor and slow-slip event (ETS): large-scale forward tremor propagation along the fault strike direction at about 5-10 km/day, sparsely distributed swarms that propagate about 5 to 50 times faster in the opposite direction ("rapid tremor reversals" or RTRs) (Houston et al. 2011), and tremor swarms that propagate even faster along-dip in the vicinity of the main SSE front (Ghosh et al. 2010; Peng et al. 2015). Bletery et al. (2017) found that secondary tremor fronts slow down as they propagate. Other tremor migration patterns have also been observed, such as tremor halting and branching, acceleration and deceleration (Kao et al. 2009). Hierarchical tremor migration patterns have also been observed in other subduction zones, such as in Shikoku, Japan (Shelly et al. 2006, 2007). Lengline et al. (2017) studied the inter-event times between LFE repeats in the Cascadia and Mexico subduction zones and found they decay inversely proportional to time after their first occurrence.

The study of SSE and tremor is significant for fundamental and practical reasons. It offers a unique window into the mechanics of the bottom of the seismogenic zone, and may contribute to earthquake hazard assessment. The location of tremor and SSE constrains the deep transition from seismogenic to aseismic slip; it may provide bounds on seismogenic width and on the maximum depth extent of large earthquake ruptures. Such information is critical in subduction regions: it controls the proximity of the source to dense urban areas, hence the potential impact of

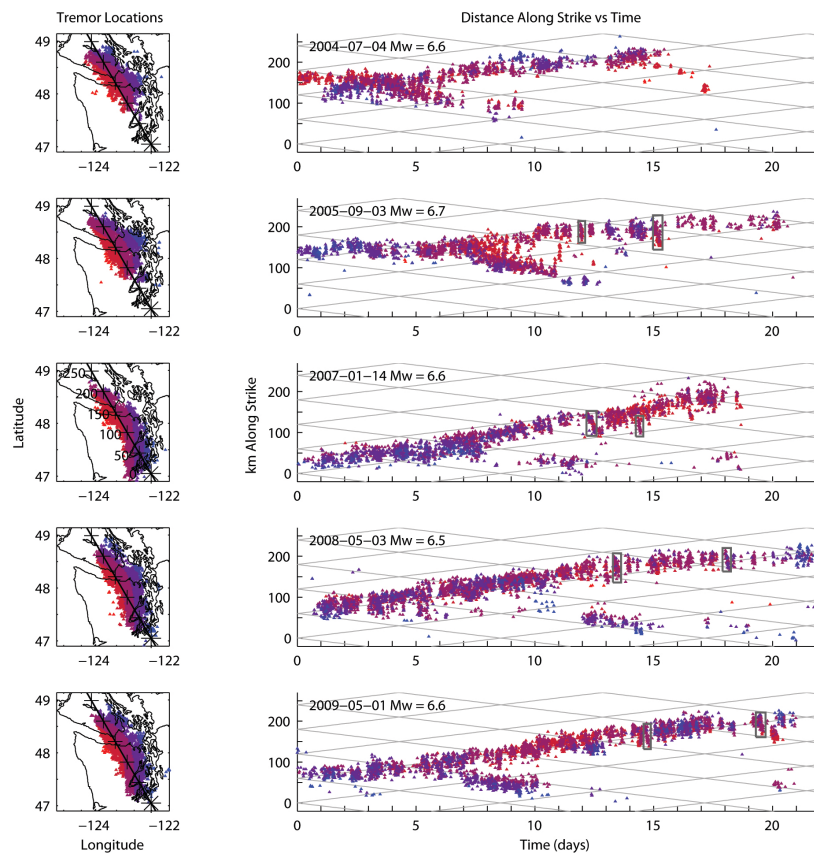


Figure 4.1: Observations of tremor migration patterns, courtesy of H. Houston. Right: spatial-temporal distribution of tremors during each ETS, projected along-strike, showing large-scale forward tremor migration and sparsely distributed rapid tremor reversals (selected RTRs marked with gray rectangles). Left: map view.

ground motions. Despite various modeling efforts (e.g. Ariyoshi et al. 2009, 2012; Ben-Zion 2012; Colella et al. 2011, 2013; Daub et al. 2011; Gershenzon et al. 2011; Hawthorne and Rubin 2013a,b; Ide et al. 2008; Rubin 2011), the nature of tremor and SSE phenomena is still incompletely understood. Most existing models reproduce subsets of the observed phenomena, some operate successfully only within a narrow range of model parameter values and, most importantly, none of those models are general enough to reproduce quantitatively the observed patterns of both SSE and tremors (see section 4.4). Thus a study of imbricated tremor and SSE processes can help understand fundamental aspects of fault mechanics, for instance by providing constraints on the rheology of the seismic-aseismic transition zones of major faults. The study of SSE and tremors might also help understanding

large earthquakes. ETS in Cascadia and Shikoku are clearly segmented along strike. Several ETS cycles have been observed on each segment, including events that span multiple segments. Accounting for multi-segment ruptures is an important recent development in earthquake hazard assessment (Field et al. 2017). The study of ETS segmentation may help constrain mechanical and statistical models of multi-segment interactions. Observing and modeling ETS may also shed light on the slow slip and foreshock activity that has been observed or inferred to precede some recent large subduction earthquakes, such as the 2014 Iquique, Chile earthquake (Ampuero et al. 2014; Ruiz et al. 2014) and the 2011 Tohoku, Japan earthquake (Kato et al. 2012)). Tremor activity during the initiation of large SSEs also deserves focused studies, as it may be a slow-motion version of the nucleation process of large earthquakes.

Studying the relation between SSE and tremor may reveal new approaches to monitor SSE through tremor activity. SSEs are conventionally monitored by geodetic methods, such as GPS, which have limited spatial resolution on deep slip (tens of kilometers) and limited detection capability for very slow slip rates (microns per second). The coupling between SSEs and tremors provides observations with higher resolution. Advances in data analysis techniques, including beam-forming of multiple arrays (Ghosh et al. 2010), waveform matched filter LFE detection (Shelly et al. 2007) and detection algorithms utilizing current developments such as machine learning (Rouet-Leduc et al. 2017), are allowing the characterization of tremor activity with increasing resolution. Thus it is timely to study the mechanical relations between the spatial-temporal behavior of non-volcanic tremors and the underlying slow slip transients. We will show (in section 4.4) that in our model the tremor rate is proportional to local slip rates. Such a relation is straightforward to conceive for isolated asperities producing repeating earthquakes, and it has been commonly assumed or inferred that the seismicity rate of repeating earthquakes is proportional to the slip rate of the driving aseismic slip (e.g. Chen et al. 2007). However, in a fault containing multiple closely located asperities, such as in the tremor environment, it is uncertain to what degree the interactions between asperities complicate the relation between seismic and aseismic activity. Our models allow us to investigate the relation between tremor rate and slip rate under strong interactions, to understand how to constrain SSE slip rate through tremor observations.

Here, we will address four key open questions about tremor and SSE processes:

1. **Is SSE a cause or a result of tremor?** In other words, do tremors just ride the wave of a slow slip event, or do they contribute to, or even generate slow slip?

To what extent are tremors and slow slip two inextricable manifestations of a single mechanical process? To address this fundamental question, we design two end-member models: in the first model tremor activities are driven by slow slip, while in the second model slow slip is driven by tremor. We aim at identifying differences that can distinguish these two models in current or future observational studies. While currently the common view is that tremors are the byproduct of SSEs, we will show that some observed characteristics of tremor migration patterns actually favor the tremor-driven-SSE model.

2. **What do tremor migration patterns tell us about fault rheology?** Migrating tremor swarms display intriguing hierarchical patterns. We will find that the imbricated patterns of forward tremor migration and RTR shed light on the rheology of the fault zone matrix. For instance, we will find that linear viscosity is insufficient to generate hierarchical tremor migration patterns.
3. **Can a heterogeneous rate-and-state fault generate SSEs robustly, without fine tuning of model parameters?** Previous studies show that a homogeneous fault governed by the classical, laboratory-motivated rate-and-state friction law (defined in section 4.2) can generate SSEs only within a narrow range of model parameters (Rubin 2008). The range is especially narrow with the “slip law”, the state evolution law that is most consistent with laboratory experiments with large velocity steps. This fine tuning issue has motivated the study of other physical ingredients to explain the generation of SSE, including more sophisticated friction laws with transitions from velocity-weakening to velocity-strengthening at increasing slip rate (Hawthorne and Rubin 2013a) and the hardening effect of fault gouge dilatancy in fluid-saturated fault zones (Segall et al. 2010). Here we will investigate if fault heterogeneity can lead to robust SSEs under classical rate-and-state friction with the slip law.
4. **Can SSE properties be inferred from tremor activity?** We will demonstrate that the SSE slip rate and tremor activity rate are closely related. Thus, observed tremor activity rates can be used to estimate, with high spatial-temporal resolution, slip rates of the underlying SSE.

The remainder of this paper is organized as follows. In section **4.2 Modeling**, we present the basic ingredients of our heterogeneous fault models, our conceptual explanation of the origin of hierarchical tremor migration patterns and general aspects of rate-and-state friction. We then introduce the two end-member models

of SSE-driven-tremor and tremor-driven-SSE. In section **4.3 Results**, we present 2D numerical rate-and-state simulation results to demonstrate that both models produce quantitative agreement with observations of SSE and tremor migration. We then analyze the effects of model parameters, such as the strength contrast and distribution of asperities, on observable tremor properties. In section **4.4 Discussion**, we compare the two models and identify observable characteristics of tremor that might be used to distinguish them. We then establish links between RTR propagation speed and distance, and the underlying slow slip rate. We also discuss previously proposed models in light of our modeling results, review the limitations of our models, propose directions for future work, and present preliminary results of 3D modeling. Finally, in section **4.5 Conclusion**, we summarize our results in relation to the key questions formulated above.

## 4.2 Modeling

### Conceptual models

In a view that has emerged from tremor and slow slip observations (e.g. Ito et al. 2009), tremor results from dynamic shear failure of competent asperities on an otherwise creeping fault zone. The seismic-aseismic transition region has heterogeneous frictional properties, and is composed of frictionally unstable patches ("competent asperities") embedded in a frictionally more stable fault matrix. Whereas tremors are commonly viewed as swarms of LFEs driven by an underlying, larger scale slow slip transient, here we also explore how tremor swarms can emerge from the collective response of asperities that trigger aseismic slip in their surroundings and interact via these aseismic transients (Figure 4.2 and 4.3, see also Ariyoshi et al. (2009, 2012)).

The existence of deep asperities is supported by seismological and geological observations. Seismological evidence includes the observation that tremors are composed of LFEs (Ide et al. 2007b; Shelly et al. 2006, 2007) and occasionally Very Low Frequency Earthquakes with double couple focal mechanism consistent with shear failure on the megathrust. The existence of deep asperities is also supported by the deepening of seismicity following the M7.3 Landers earthquake (Rolandone et al. 2004) and by high frequency radiation from the deeper parts of the fault during the 2010 Tohoku and other subduction earthquakes (Lay et al. 2012; Meng et al. 2011). Geological observations of exhumed subduction faults show a mélangé structure with competent lenses embedded in a incompetent matrix (Bebout and Barton 2002; Fagereng 2011; Fagereng and Cooper 2010; Fagereng and Sibson

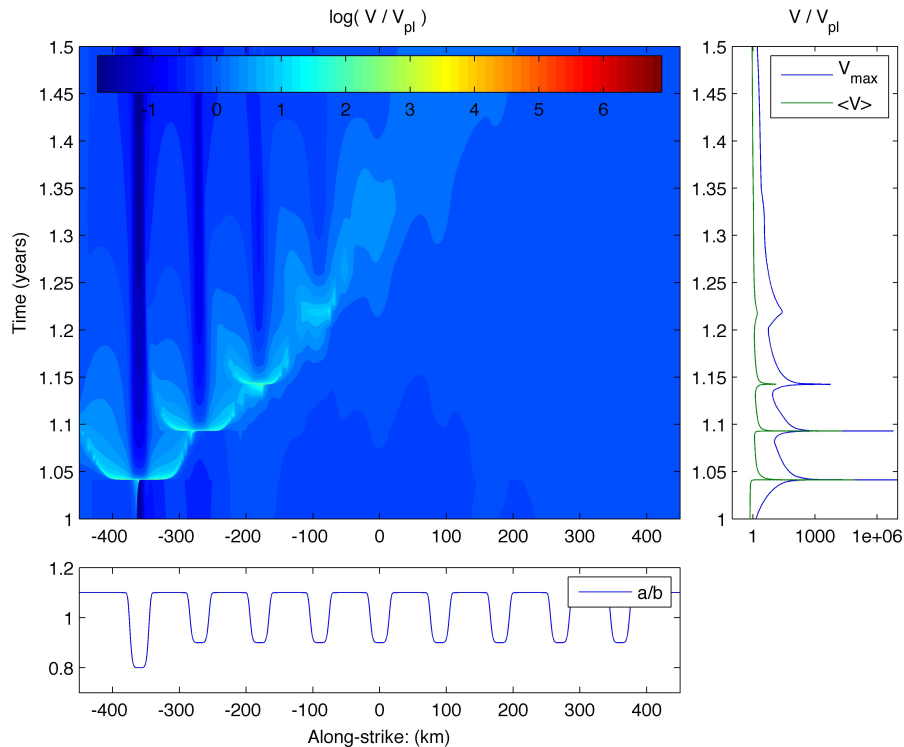


Figure 4.2: An example of asperity triggering cascade on a 1D fault. The main plot shows the logarithm of slip rate normalized by plate velocity as a function of space and time. Right: maximum slip rate (blue) and average slip rate over the fault (green) as a function of time. Bottom: spatial distribution of  $a/b$  ratio. Velocity strengthening regions have  $a > b$ , velocity weakening asperities have  $a < b$ . When the leftmost asperity fails, it produces a migrating post-seismic slip perturbation that triggers the adjacent asperity. This process repeats in a cascade.

2010; Meneghini et al. 2010).

In our conceptual model, seismic failure of a competent asperity induces post-seismic slip that propagates outwards from the asperity. Propagating afterslip is typically obtained in numerical simulations (Figure 4.4, see also Ariyoshi et al. (2012) and Kato (2007)) and is supported by observations of expanding aftershock zones (Kato 2007; Peng and Gomberg 2010). An afterslip front approaching another asperity loads it and can trigger its rupture (Lui and Lapusta 2016). The process can repeat, leading to a cascade of asperity ruptures mediated by afterslip and taking the appearance of a tremor swarm (Figure 4.2; see also Ando et al. (2010, 2012) and Ariyoshi et al. (2009, 2012)). If asperities are triggered at the arrival of afterslip fronts, without significant delay, then the migration speed of the swarm is controlled

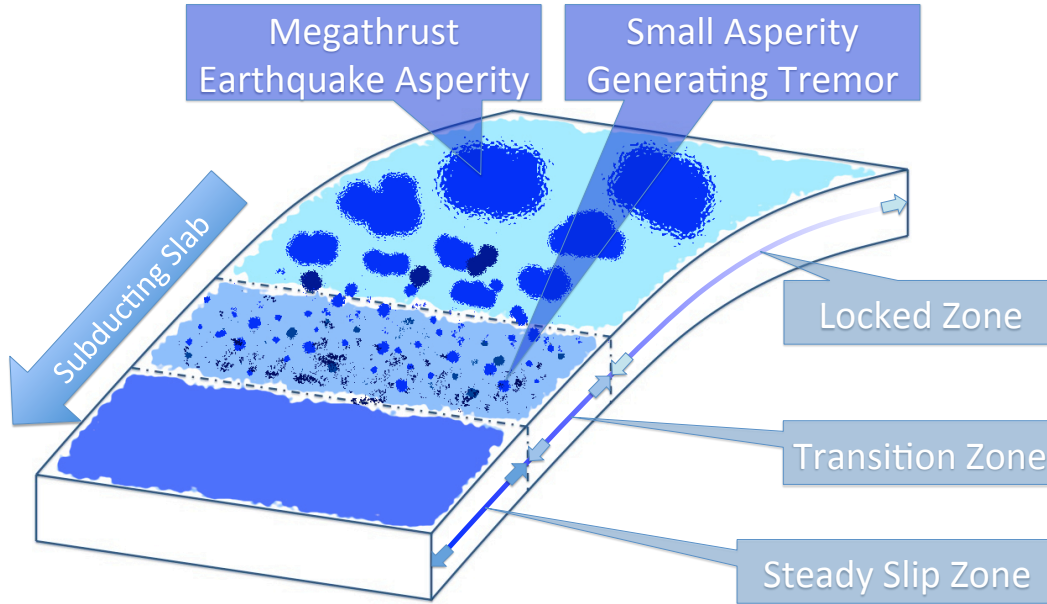


Figure 4.3: Conceptual model of heterogeneous seismic/aseismic transition zone of a subduction fault. Numerous small, competent asperities (darker dots) are embedded in the transition zone with more incompetent background matrix, interactions of these asperities form imbricated tremor migration patterns.

by the propagation speed of the afterslip front,  $V_{prop}$ . On the one hand, a relation between the propagation speed of a slip front  $V_{prop}$  and its peak slip velocity  $V_{max}$ , valid for any friction law that features weakening within a small process zone near the slip front, is (Ampuero and Rubin 2008):

$$V_{prop} \propto \frac{GV_{max}}{\Delta\tau_{p-r}} \quad (4.1)$$

where  $G$  is the shear modulus and  $\Delta\tau_{p-r}$  is the peak to residual strength drop due to frictional weakening. In rate-and-state friction laws derived from laboratory experiments at low slip rate,  $\Delta\tau_{p-r}$  depends only weakly (logarithmically) on  $V_{max}$ , hence a key outcome of Equation 4.1 is:

$$V_{prop} \propto V_{max} \quad (4.2)$$

On the other hand, if  $V_{max}$  correlates with the background slip rate  $V_{bg}$  that prevails before the arrival of a slip front, then  $V_{prop}$  correlates with  $V_{bg}$ . We will show in section 4.2 that such a correlation is satisfied by rate-and-state friction (Figure 4.4), but it is not satisfied by other fault zone rheologies such as the Newtonian viscosity assumed by Ando et al. (2010, 2012) (see more in section 4.4). For rate-and-state

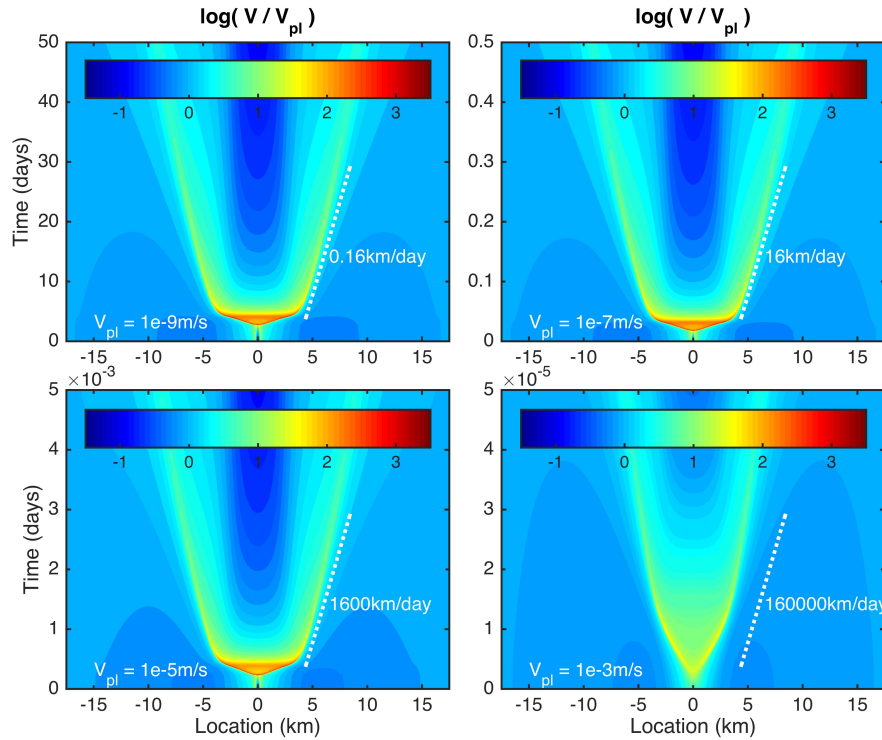


Figure 4.4: Comparison of the propagating velocity  $V_{prop}$  of the afterslip front induced by a VW asperity surrounded by VS material, for different values of the background slip rate  $V_{pl}$  labeled at the bottom left corner of each plot. The overall propagation speed is indicated in each plot by a white dashed line and a label. The results for  $V_{pl} = 10^{-9}$  m/s to  $10^{-5}$  m/s indicate  $V_{prop} \propto V_{pl}$ . The proportionality relation degrades when inertial effects become significant, if  $V_{pl}$  approaches dynamic slip rate  $V_{dyn}$  and  $V_{prop}$  approaches shear wave velocity (bottom-right plot).

friction we will indeed find a nearly proportional relation, thus

$$V_{prop} \propto V_{bg} \quad (4.3)$$

The slip rate within an SSE pulse is the background slip rate  $V_{bg}$  that prevails around the tremor asperities and, according to the relation above, controls the propagation speed  $V_{prop}$ . The spatial distribution of slip rate within an SSE pulse is expected, from fracture mechanics, to have high values near the front and low values at the tail. These features are illustrated in Figure 4.5, which shows the slip rate distribution as a function of time and distance of a sample SSE from our rate-and-state simulations (See also figure 3 and figure 4 in Hawthorne and Rubin 2013a). Thus we interpret the very fast (mostly) along-dip tremor swarms as running along the front of the SSE pulse, where the highest  $V_{bg}$  values are concentrated, and RTRs as swarms running

into the tail of the SSE pulse, where  $V_{bg}$  is lower. The slowdown of RTRs (Bletery et al. 2017) and tremor branching are interpreted as swarms running further into the SSE pulse tail where  $V_{bg}$  gradually decreases.

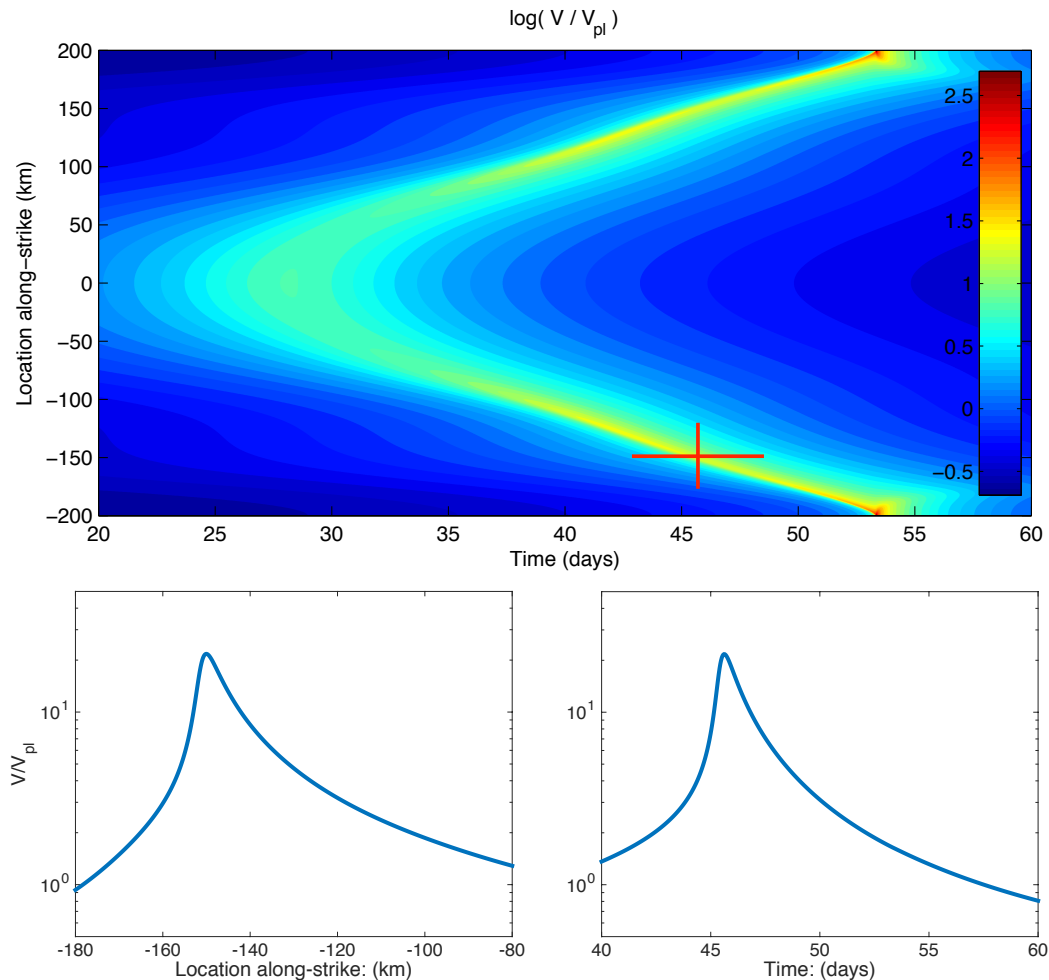


Figure 4.5: Example of modeled slow-slip event (SSE). Top: logarithmic slip rate normalized by plate loading rate  $V_{pl}$  (colors) as a function of time and location along the fault. The SSE propagates bilaterally with a propagation velocity of about 7 km/day. Bottom-left: logarithmic slip rate normalized by plate velocity as a function of distance at  $t = 45.6$  days, marked as red cross in the upper figure. Bottom-right: logarithmic slip rate normalized by plate velocity as a function of time at  $x = -150$  km, marked as red cross in the upper figure.

In this conceptual model, the qualitative connection between tremor migration speed and the underlying slow slip rate leads naturally to the whole hierarchy of tremor migration patterns (Figure 4.6). To make quantitative comparisons between theory and observations, we next develop specific computational realizations of the conceptual model based on rate-and-state friction.

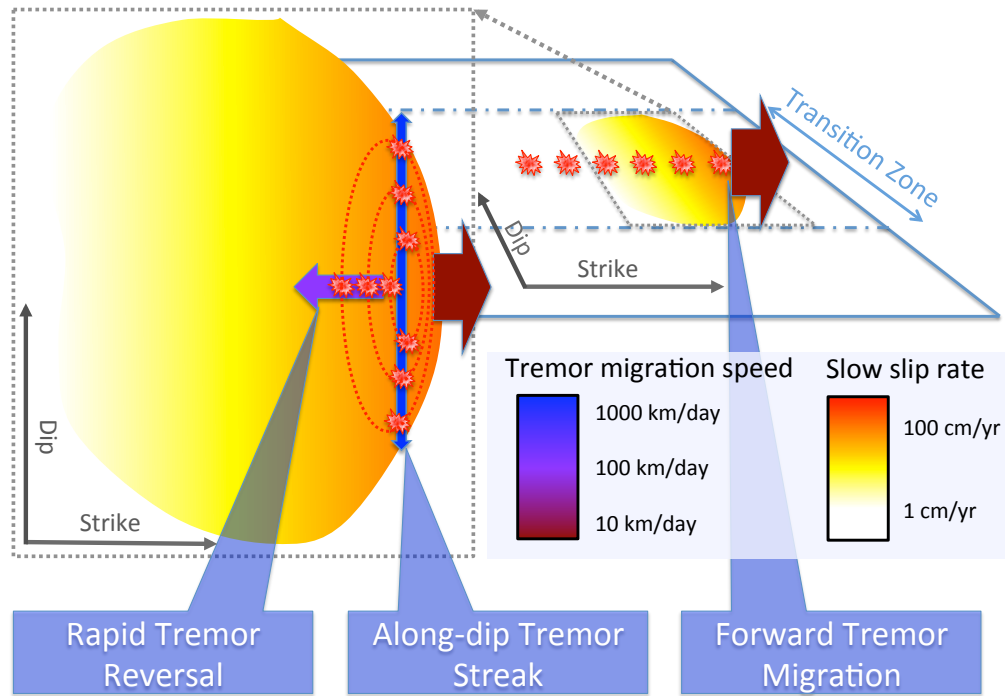


Figure 4.6: Conceptual model of hierarchical tremor migration patterns. Right: forward tremor migration is triggered by the on-going SSE front; yellow gradient shows the approximate slip rate distribution of SSE; red stars indicate the tremors. Left: zoom-in view. The interaction of asperities produces rapid tremor reversals and faster tremor swarms along-dip due to the mechanical correlation between migration speed and the spatial distribution of slip rate of the SSE front. Red dashed contours are isochrone contours of the post-seismic slip front induced by a breaking asperity, which propagates faster if the local background slip rate is higher.

### Rate-and-state friction models

We consider laboratory-motivated rate-and-state friction laws (Dieterich 1979; Marone 1998; Ruina 1983). The friction coefficient  $\mu$  is a function of slip velocity  $V$  and a state variable  $\theta$ :

$$\mu = \mu^* + a \ln \frac{V}{V^*} + b \ln \frac{V^* \theta}{D_c} \quad (4.4)$$

where  $\mu^*$  is the reference steady-state friction coefficient at the arbitrary reference velocity  $V^*$ ,  $D_c$  is the characteristic slip distance for state evolution,  $a$  and  $b$  are constitutive parameters quantifying the direct and evolution effects, respectively. The evolution of the state variable  $\theta$  is determined by an empirical law. We adopt here the so-called "slip law", the state evolution law that is most consistent with

laboratory experiments with large velocity steps representative of the sharp slip acceleration at an SSE front (Bhattacharya and Rubin 2014):

$$\dot{\theta} = \frac{V\theta}{D_c} \ln \frac{V\theta}{D_c} \quad (4.5)$$

When  $a - b > 0$ , the fault is velocity-strengthening at steady state (VS), i.e. fault friction increases as slip rate increases. On a VS fault, slip transients do not occur spontaneously, but they can be induced by external perturbations (Perfettini and Ampuero 2008). When  $a - b < 0$ , the fault is velocity-weakening at steady state (VW), i.e. friction decreases as slip rate increases. On VW faults, spontaneous slip transients can occur if the fault stiffness is below a certain critical stiffness, e.g. a VW asperity driven by surrounding creep fails repeatedly, generating seismic events, if its size exceeds the critical size defined by:

$$L_c = \frac{GD_c}{(b - a)\sigma} \quad (4.6)$$

where  $\sigma$  is the effective normal stress (normal stress minus pore fluid pressure). We refer to such asperities as *supercritical*. Under the slip law, if an asperity is *subcritical*, i.e. its size is smaller than the critical size  $L_c$ , it can still be triggered by a strong enough external perturbation.

The conceptual model introduced in the previous subsection relied on a correlation between peak slip rate  $V_{max}$  and background slip rate  $V_{bg}$ . We can justify that assumption under the rate-and-state framework. A location on the VS fault matrix, in the vicinity of a VW asperity that just broke, experiences a positive stress perturbation  $\Delta\tau$  induced by the sudden asperity slip. This perturbation is proportional to the stress drop in the asperity and decays as a function of distance from the asperity. As a result, slip in the VS area accelerates. Evaluating Equation 4.4, before the arrival of the afterslip front:

$$\tau_{bg} = \sigma \left( \mu^* + a \ln \frac{V_{bg}}{V^*} + b \ln \frac{V^*\theta_{bg}}{D_c} \right) \quad (4.7)$$

During the passage of the afterslip front, the slip first rapidly accelerates and then decelerates. The shear stress when slip rate reaches its peak  $V_{max}$  is

$$\tau_{max} = \sigma \left( \mu^* + a \ln \frac{V_{max}}{V^*} + b \ln \frac{V^*\theta_{bg}}{D_c} \right) \quad (4.8)$$

Here we have made the approximation  $\theta \approx \theta_{bg}$ , because the state variable has little time to evolve during the acceleration stage at the arrival of the afterslip front.

Subtracting Equations 4.7 and 4.8 yields the stress change

$$\Delta\tau = \tau_{max} - \tau_{bg} = a\sigma \ln \frac{V_{max}}{V_{bg}} \quad (4.9)$$

We can rewrite this as

$$V_{max} \approx e^{\frac{\Delta\tau}{a\sigma}} V_{bg} \quad (4.10)$$

Combining this relation with Equation 4.2, we get

$$V_{prop} \propto e^{\frac{\Delta\tau}{a\sigma}} V_{bg} \quad (4.11)$$

This equation indicates that, given a spatial distribution of stress increment  $\Delta\tau$  imposed by an asperity failure, the propagation speed  $V_{prop}$  of the induced afterslip is proportional to the background slip velocity  $V_{bg}$ .

In our simulations, we adopt the quasi-dynamic approximation:

$$\tau(x, t) = \tau^\infty + \frac{G}{2}H(\delta) - \frac{G}{2C_s}V \quad (4.12)$$

The first term on the right hand side ( $\tau^\infty$ ) is the external shear loading. The second term  $H(\delta)$  is a linear functional representing the static stress transfer due to slip  $\delta$ . The inertial effects are approximated by considering the stress reduction due to the radiation of seismic waves in the direction normal to the fault plane, represented by the radiation damping term (Rice 1993), the third term (where  $C_s$  is the shear wave velocity). These equations are solved by a numerical code based on the Boundary Element Method, QDYN (Luo et al. 2017)

In this study we consider a simplified 1.5D fault model with periodic boundary conditions. The original problem involves transient slip on a 2D fault region of finite width  $W$ , loaded by steady slip on the rest of the fault. The dimensionality of the problem is reduced by assuming the along-dip distribution of slip is fixed, so that the only remaining unknowns are the fluctuations of slip along-strike (Luo and Ampuero 2017). Other model settings are provided in section 4.2 and in appendix A2 of Luo and Ampuero (2017). We set the cell size much smaller than the process-zone size,  $L_b = D_c G / b\sigma$ , so that the cohesive zone near slip fronts and the minimum nucleation size are well-resolved in the fault matrix (Perfettini and Ampuero 2008). As our models emphasize the collective effect of interactions between asperities, the details of the spatial distribution of slip inside asperities are not essential and, to save computational resources, we represent each asperity by a single computational cell.

### SSE-driven-tremor model

In the SSE-driven-tremor model, tremors are driven by spontaneous SSEs. The fault matrix is an unstable but aseismic material that generates SSEs spontaneously, which then drive the seismic failure of asperities (Figure 4.6). In order to study the multi-scale problem of SSE and RTR efficiently, in this section we first study the generation of SSEs, then the response of isolated asperities to transient loads, and finally we combine SSEs and asperities to simulate ETS.

### Generation of slow slip events

SSEs can be generated by various mechanisms. Under classical rate-and-state friction, SSEs can occur in a VW strip, sandwiched between a deeper steady creep fault region and a shallower coupled seismic zone, if its along-dip width is near a critical length (e.g. Liu and Rice 2005; Rubín 2008). Another mechanism to limit slip velocity is the fault strengthening effect of gouge dilatancy in a fluid saturated fault zone (e.g. Segall et al. 2010). Slow slip can also be obtained under friction laws with two state variables (e.g. Rubín 2011) or with a transition from velocity-weakening to velocity-strengthening at increasing slip rate (e.g. Hawthorne and Rubín 2013a; Shibasaki and Iio 2003). Some of these mechanisms require tuning model parameters within a very narrow range of values, which is problematic. Because our focus is on modeling tremor migration, we conveniently adopt the SSE generation model based on friction with VW-to-VS transition. The friction coefficient  $\mu$  is given by

$$\mu(V, \theta) = \mu^* - a \ln \left( \frac{V_1}{V} + 1 \right) + b \ln \left( \frac{V_2 \theta}{D_c + 1} \right) \quad (4.13)$$

where  $V_1$  and  $V_2$  are cut-off velocities of the direct effect and the evolution effect, respectively. Figure 4.7 shows the steady-state friction coefficient,  $\mu(V, D_c/V)$ , as a function of slip velocity, for different values of  $V_2$ . The VW-VS transition is governed by  $V_2$  and friction properties  $a$  and  $b$ : it occurs at  $V_t = V_2 \frac{b-a}{a}$  (Hawthorne and Rubín 2013a). Strengthening effectively sets a soft limit to the maximum slip rate.

Current observations of SSE in North Cascadia provide the following constraints to our model: recurrence time is on the order of 1 year, duration is a few weeks, stress drop tens of kPa, propagation speed about 5-10 km/day, and slip velocity about 10 to 100 times the plate velocity (Houston et al. 2011). Fault size and plate loading rate are also well constrained. Here we build up on a comprehensive study

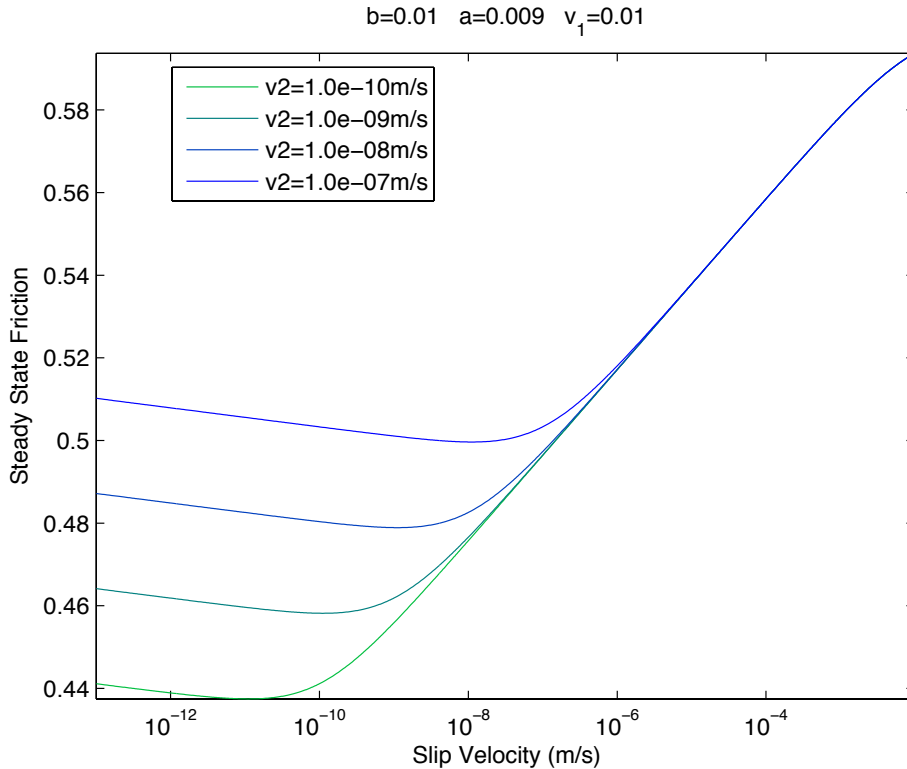


Figure 4.7: Steady-state friction of the rate-and state law with cut-off velocity, as a function of slip velocity, for different values of the cut-off velocity of the evolution effect ( $V_2$ ). The transition from VW to VS is controlled by  $V_2$  if  $a$  and  $b$  are fixed.

by Hawthorne and Rubin (2013a) that identified model parameters that reproduce observed SSE properties. The value of  $D_c$  spans a relatively wide range in laboratory results and contributes to stress drop, but its effect trades off with  $b$  and  $\sigma$ . Here, we adopt a representative laboratory value of 0.4 mm. We explored the effect of effective normal stress  $\sigma$  and cut-off velocity  $V_2$ . Figure 4.8 shows the peak slip rate  $V_{max\_SSE}$  and propagation velocity  $V_{SSE}$  measured in our simulations with various values of  $\sigma$  and  $V_2$ , during periods of relatively steady SSE propagation. We exclude periods of acceleration at the end of SSEs caused by the periodic boundary conditions assumed along-strike. We find a range of parameters that reproduce the key observations quantitatively, and finally adopt a set of model parameters (Table 4.1) that yields SSEs with recurrence time of about 6 months, duration of about 3 weeks, propagation speed of about 7 km/day, slip velocity lower than  $10^{-7}$  m/s (100 times plate velocity), and stress drop of about 10 kPa (Figure 4.5).

In the model, parameter settings and resulting SSE are similar to those in the work by Hawthorne and Rubin (2013a), but there are two notable differences. We generate

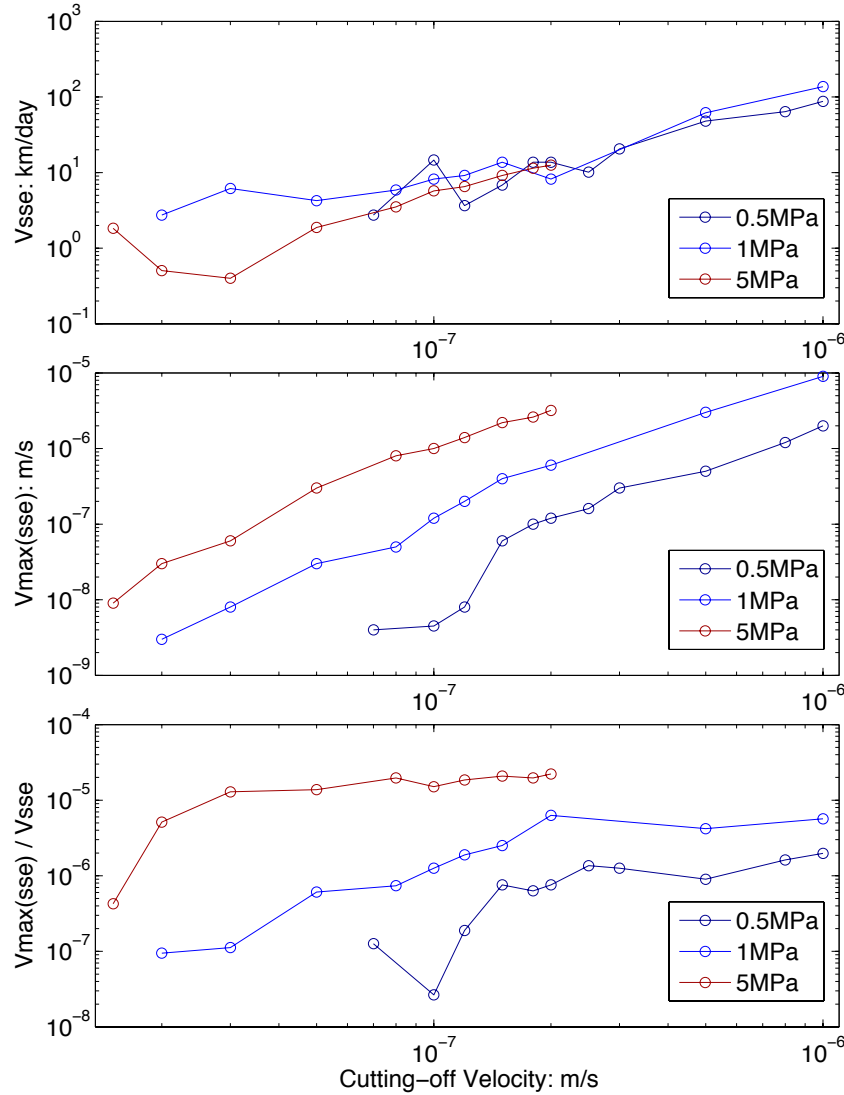


Figure 4.8: Propagation velocity of SSE ( $V_{SSE}$ ) and peak slip rate inside the SSE front ( $V_{max\_SSE}$ ) as a function of the cut-off velocity  $V_2$ , for three different values of effective normal stress  $\sigma$ . Within a certain range of  $V_2$ , both  $V_{SSE}$  and  $V_{max\_SSE}$  increase with increasing  $V_2$ . However,  $V_{max\_SSE}$  increases faster, leading to large  $V_{max\_SSE}/V_{SSE}$  ratios and ultimately larger  $V_{RTR}/V_{SSE}$  ratio.

SSE on a fault with homogeneous friction properties. Both [Hawthorne and Rubin \(2013a\)](#)'s and our models have periodic boundary conditions. A trivial solution under periodic boundary condition and uniform friction properties is uniform slip, without SSE front propagation. [Hawthorne and Rubin \(2013a\)](#) introduced material heterogeneity, a small VS patch, to avoid convergence to the trivial uniform slip solution. Here, we obtained episodic steady-propagating SSEs in a homogeneous fault by considering heterogeneous initial conditions. In most cases, this episodic

Physical properties	Value
fault period $L$	400km
fault width $W$	110km
shear modulus $G$	30GPa
shear wave velocity $C_s$	3000m/s
reference friction coefficient $\mu^*$	0.6
tectonic loading rate $V_{pl}$	$10^{-9}$ m/s
asperity actual size $L_{asp}$	100m (typical)
	31.25m to 400m (various)
$b\sigma_{bg}$	10KPa (typical)
	5 to 50KPa (various)
$b\sigma_{asp}$	100 to 500KPa (typical)
	10 to 1000KPa (various)
$a\sigma_{bg}$ @ SSE-driven model	9KPa (typical)
	4.5 to 45KPa (various)
$a\sigma_{bg}$ @ tremor-driven model	12KPa (typical)
	6 to 60KPa (various)
$a\sigma_{asp}$	90 to 450KPa (typical)
	9 to 900KPa (various)
background characteristic slip distance $D_{c\_bg}$	$4 \times 10^{-4}$ m
asperity characteristic slip distance $D_{c\_asp}$	$1 \times 10^{-4}$ to $1 \times 10^{-3}$ m (typical)
	$4 \times 10^{-5}$ to $4 \times 10^{-3}$ m (various)
cut-off velocity (direct effect) $V_1$ @ SSE-driven model	0.01m/s
cut-off velocity (indirect effect) $V_2$ @ SSE-driven model	$10^{-8}$ to $10^{-5}$ m/s (various)
asperity density	10 to 20% (typical)
	5 to 50% (various)

Table 4.1: Typical parametric settings of rate-and-state simulation

SSE behavior is a strong attractor: the fault approaches a limit cycle after a few cycles. Transient non-uniform slip solutions on homogeneous faults were previously identified in rate-and-state models by [Horowitz and Ruina \(1989\)](#). The second notable difference is that we obtain a higher ratio between peak slip velocity and propagation speed,  $V_{max\_SSE}/V_{SSE}$ , than [Hawthorne and Rubin \(2013a\)](#). We find that increasing  $V_2$  increases both  $V_{max\_SSE}$  and  $V_{SSE}$ , but has a stronger effect on  $V_{max\_SSE}$ , which enables higher values of  $V_{max\_SSE}/V_{SSE}$  ([Figure 4.8](#)). We will find this useful to obtain ratios between RTR and SSE propagation speeds as high as observed in Cascadia (section 4.4), a goal that has proven challenging for previous models (e.g. [Ando et al. 2010, 2012](#); [Colella et al. 2011, 2013](#); [Hawthorne and Rubin 2013b](#)).

## Response of isolated asperities to transient loading

Basic tremor observations and our conceptual model (section 4.2) provide constraints on asperity properties. Asperities should be pure VW (no VW-VS transition) so that they fail with high slip rates associated to seismic radiation, i.e. exceeding the dynamic velocity  $V_{dyn} = 2(a - b)C_s\sigma/G$  above which radiation damping becomes important (Rubin and Ampuero 2005). Because our focus is on ETS, to limit the computational cost of the simulations we consider only subcritical asperities, so that failure is induced during SSEs but does not occur spontaneously in between SSEs. Moreover, in Cascadia the “background tremor” activity in between ETS events is weaker and deeper (Wech et al. 2010). Lastly, we focus on modeling asperities that are triggered only a few times by an SSE. For a given loading rate, an asperity that breaks infrequently has a higher stress drop than an asperity that breaks often. It hence generates a stronger afterslip transient, which favors the emergence of migrating swarms. Observations show that LFEs break multiple times during a large SSE, but often in bursts that have been associated to secondary (smaller-scale) slip transients (e.g. Lengline et al. 2017; Peng et al. 2015).

To identify values of asperity properties that allow asperities to be triggered only a few times by an SSE, we study the response of an isolated asperity to a transient loading akin to the loading imposed by the passage of a SSE. We consider an elementary model: we study the response of a single-degree-of-freedom spring-block system to Gaussian shaped transient loadings as a function of the loading duration  $T_p$ , which represents the SSE rise time (local slip duration). (Figure 4.9) shows the resulting slip velocity for a range of  $T_p$  values. We find that the asperity is triggered only once if  $T_p$  is comparable to  $T_{rec\_asp} = \frac{2D_c}{V_{pl}}\sqrt{\frac{a}{b-a}}$ , the recurrence time of slip on an asperity of critical size. If  $T_p \ll T_{rec\_asp}$  the asperity is not triggered, and if  $T_p \gg T_{rec\_asp}$  it breaks too many times (when applying a higher transient loading amplitude than shown in Figure 4.9). Henceforth we consider subcritical asperities with  $T_p \approx T_{rec\_asp}$ .

## Modeling forward tremor migration and RTRs

To combine the above models of SSE and asperities, we first simulate multiple SSE “warm-up cycles” without asperities using the parametric settings identified in section 4.2 until the fault behavior reaches a limit cycle independent of the initial conditions. We then add asperities and run a few more warm-up cycles. The asperities are evenly distributed in space, with the properties identified in the

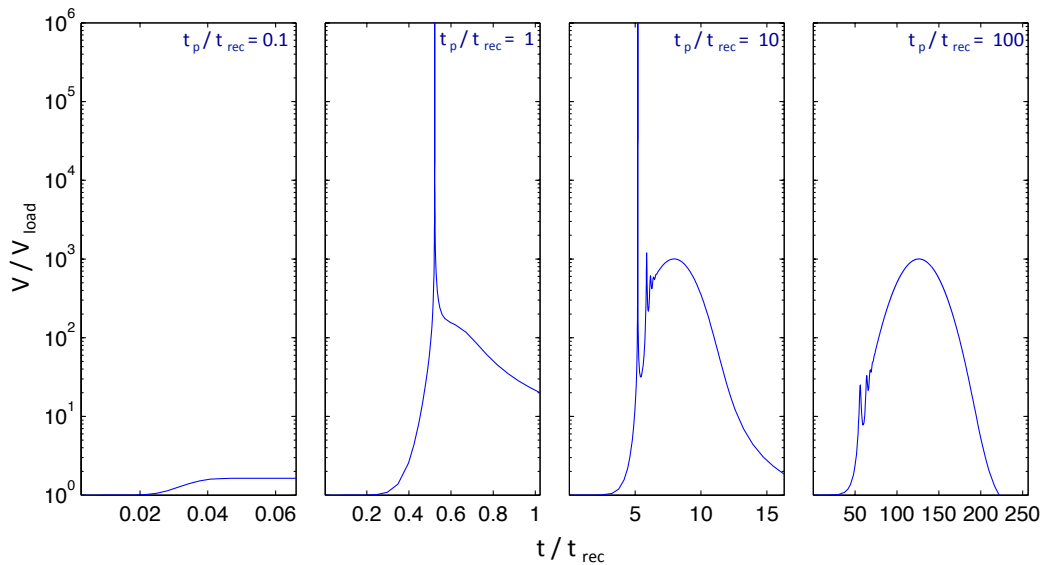


Figure 4.9: Slip velocity of a sub-critical spring-block system in response to transient loading with four different durations (indicated by labels at the top-right corner of each plot). The simulation time is normalized by the characteristic recurrence time ( $T_{rec\_asp}$ ) of a critical asperity. Slip rate is normalized by the background loading rate  $V_{pl}$ . The amplitude of the imposed loading perturbation is 1000 times  $V_{pl}$ . From left to right, the duration of the perturbation ( $T_p$ ) is 0.1, 1, 10 and 100 times  $T_{rec\_asp}$ , respectively. If  $T_p$  is comparable to  $T_{rec\_asp}$ , the system breaks seismically and only once during the loading transient.

previous section. We explore various values of asperity spacing and relative strength defined as the contrast of  $|b - a|\sigma$  values inside and outside asperities. We assign random  $D_c$  values to each asperity. This results in a broad range of individual asperity criticalness defined as  $\beta = L_{asp}/L_{c\_asp}$ , where  $L_{asp}$  is the asperity size (a single cell) and  $L_{c\_asp}$  is the critical size defined in Equation 4.6. Detailed parameter settings are presented in Table 4.1.

We find that, although the rich SSE and tremor behavior can be reproduced with a relatively wide range of asperity densities and relative strengths, the highly heterogeneous asperity criticalness is essential to generate RTRs matching observations in Cascadia. Thus we hypothesize that heterogeneity of asperity properties is a necessary condition for the generation of RTRs (section 4.3).

### **Tremor-driven-SSE model**

In the process of our exploration of the SSE-driven-tremor model, we found that asperities can have a large impact on the overall behavior of the fault. We thus conducted an extensive numerical and theoretical study of the stability of faults with mixtures of VW and VS materials (Luo and Ampuero 2017). That study complements previous work by Dublanchet et al. (2013), Skarbek et al. (2012), and Yabe and Ide (2017). The results show that a composite fault can be unstable even if the VW material occupies only a small fraction of the fault surface, provided it has high enough strength contrast relative to the VS material, quantified by the ratio of  $|b - a|\sigma$  between the two materials. In the SSE and tremor environment, strength contrast between asperities and matrix is likely due to contrast of effective normal stress  $\sigma$  arising from spatial and temporal fluctuations of fault zone fluid pressure.

The study of the stability of composite faults (Luo and Ampuero 2017) suggests that the mixture of VW and VS materials with relative strength contrast is a sufficient ingredient to reproduce a broad spectrum of fault behavior ranging from slow to rapid transients. In particular, it provides insight on the material mixture properties leading to spontaneous slip transients on heterogeneous faults. This motivates us to develop an alternative model which, unlike the SSE-driven-tremor model, can generate SSEs and tremors without appealing to friction with VW-VS transition in the fault matrix. In our tremor-driven-SSE model friction in the matrix is purely VS. The asperity properties are similar to those in the SSE-driven-tremor model. A distinct feature of the tremor-driven-SSE model is that SSEs are generated only in the presence of asperities; they emerge as the collective behavior of interacting VW and VS patches.

The SSE-driven-tremor model and tremor-driven-SSE model are end-member models to address the first key question formulated in section 4.1: is SSE a cause or a result of tremor? The considerations on asperity properties developed for the SSE-driven-tremor model are also valid for the tremor-driven-SSE model, if the loading on each asperity is viewed as imposed by the average slip rate resulting from the neighboring asperity failures and their afterslip.

## **4.3 Results**

### **Slow-slip events**

Both SSE-driven-tremor model and tremor-driven-SSE model can reproduce SSEs in quantitative agreement with observations in Cascadia (Figure 4.5). The target

SSE properties include recurrence time of about 6 months, duration of about 3 weeks, propagation speed of about 7 km/day, slip velocity lower than  $10^{-7}$  m/s (100 times plate velocity), stress drop of about 10 kPa, and a spatial span over 100 km. These SSE properties can be modified to match observations in other regions by varying parameters like fault dimension, effective normal stress and frictional properties. In the SSE-driven-tremor model, SSE properties are mainly controlled by effective normal stress  $\sigma$  and cut-off velocity  $V_2$ . They remain mostly unchanged by the addition of asperities, unless their density or relative strength are too high.

In the tremor-driven-SSE model there is no SSE in the absence of asperities, the SSE is rather the combined result of the post-seismic slip transients of asperities. [Luo and Ampuero \(2017\)](#) show how to predict the stability of slip on a composite fault with a regular alternation of VW and VS segments. Their findings suggest that in order to generate spontaneous slip transients the overall (homogenized) fault should be velocity weakening. Applying their results to the tremor-driven-SSE model, we infer that the overall relative strength (ratio between  $|b - a|\sigma$  values of asperity and matrix) should exceed a certain value. With fixed asperity density, the larger the strength contrast is, the faster the transient slip rate will be, ranging from SSE to seismic behavior. In a homogeneous pure VW fault with the slip law, SSEs occur only within a narrow range of fault width over critical length  $W/L_c$  ([Rubin 2008](#)). In our simulations of pure VW faults, the range of fault width  $W$  permitting steady SSE propagation over long distances is even narrower than the range that permits episodic aseismic transients. However, we find that, with the addition of asperities, the range of  $W$  permitting realistic SSEs is much wider than in a homogeneous VW fault, and no fine-tuning is required. We hypothesize that this behavior is enabled by a broad range of individual criticalness of asperities and by the non-linear nature of rate-and-state friction.

### **Tremor activity featuring rapid tremor reversals**

The RTRs observed in Cascadia have a propagation distance of about 20 km and travel about 5 to 50 times faster than the large-scale forward tremor migration. Varying the spatial distribution and frictional properties of asperities, our models generate various tremor and SSE phenomena that are in qualitative agreement with observations in Cascadia.

In the SSE-driven-tremor model, we systematically studied the effect of key model parameters. We varied  $b\sigma$  inside asperities from 10 kPa to 1 MPa, which is 1

to 100 times the background value outside the asperities. We varied  $D_c$  inside the asperities from  $4 \times 10^{-5}$  m to  $4 \times 10^{-3}$  m, 0.1 to 10 times the background value. We also varied the distance between asperities from 1 to about 20 cells, that is, 1 to 20 times the size of a single-cell asperity. We varied these parameters while keeping the asperity individual criticalness  $\beta$  in a typical range of 0.01 to 0.6. We successfully simulated tremor migration patterns in quantitative agreement with observations in Cascadia (Figure 4.10): recurrence interval of ETS, spatial-temporal distribution of tremor migrations, forward and reverse tremor migration speed (and their ratio). The slow forward tremor propagation is naturally associated with sequential asperity triggering by a propagating SSE. Less trivially, the model produces RTRs similar to those observed in Cascadia: spatially scattered swarms back-propagating at fast speed,  $V_{RTR}$ , about one order of magnitude faster than the forward migration speed,  $V_{SSE}$ , with spatial distribution patterns resembling observations in Cascadia (Houston et al. 2011) and propagation distances around 10 km. The  $V_{RTR}/V_{SSE}$  ratio spans a moderately broad range of values, owing to the randomness of asperity properties and to the non-linear nature of the model. In the example shown in (Figure 4.11)  $V_{RTR}/V_{SSE}$  ranges from 2 to 10, with an average value around 5, overlapping with the lower end of values observed in Cascadia. Varying the value of the cutoff velocity  $V_2$  we achieve more realistic values up to  $V_{RTR}/V_{SSE} \approx 20$  (Figure 4.12). In the analysis of our simulation results, we define tremors as asperity failure events with peak slip velocity exceeding a certain threshold (e.g. 1 mm/s). More tremors are detected if we lower the velocity threshold. The range of model parameters that produce realistic results is relatively large: e.g. with an asperity density of 20%, models with relative strength ranging from 10 to 50 reproduce hierarchical tremor behaviors in quantitative match with observations.

The tremor-driven-SSE model, with parameter settings similar to the SSE-driven-tremor model, can also simulate the observed tremor migration patterns in quantitative agreement with observations in Cascadia (Figure 4.13). In this model, the forward tremor migration operates by a progressive cascade of asperity failures mediated by their intervening aseismic afterslip. RTRs also result from a cascade process, but propagate much faster due to the elevated background slip rate owing to previous asperity activity. RTRs in the tremor-driven-SSE model have a wider range of propagation speeds than in the SSE-driven-tremor model. The  $V_{RTR}/V_{SSE}$  ratio can be as high as 50, in agreement with the range of values observed in Cascadia of  $V_{RTR}/V_{SSE} \approx 5$  to 50. From the perspective of  $V_{RTR}/V_{SSE}$  ratios, the

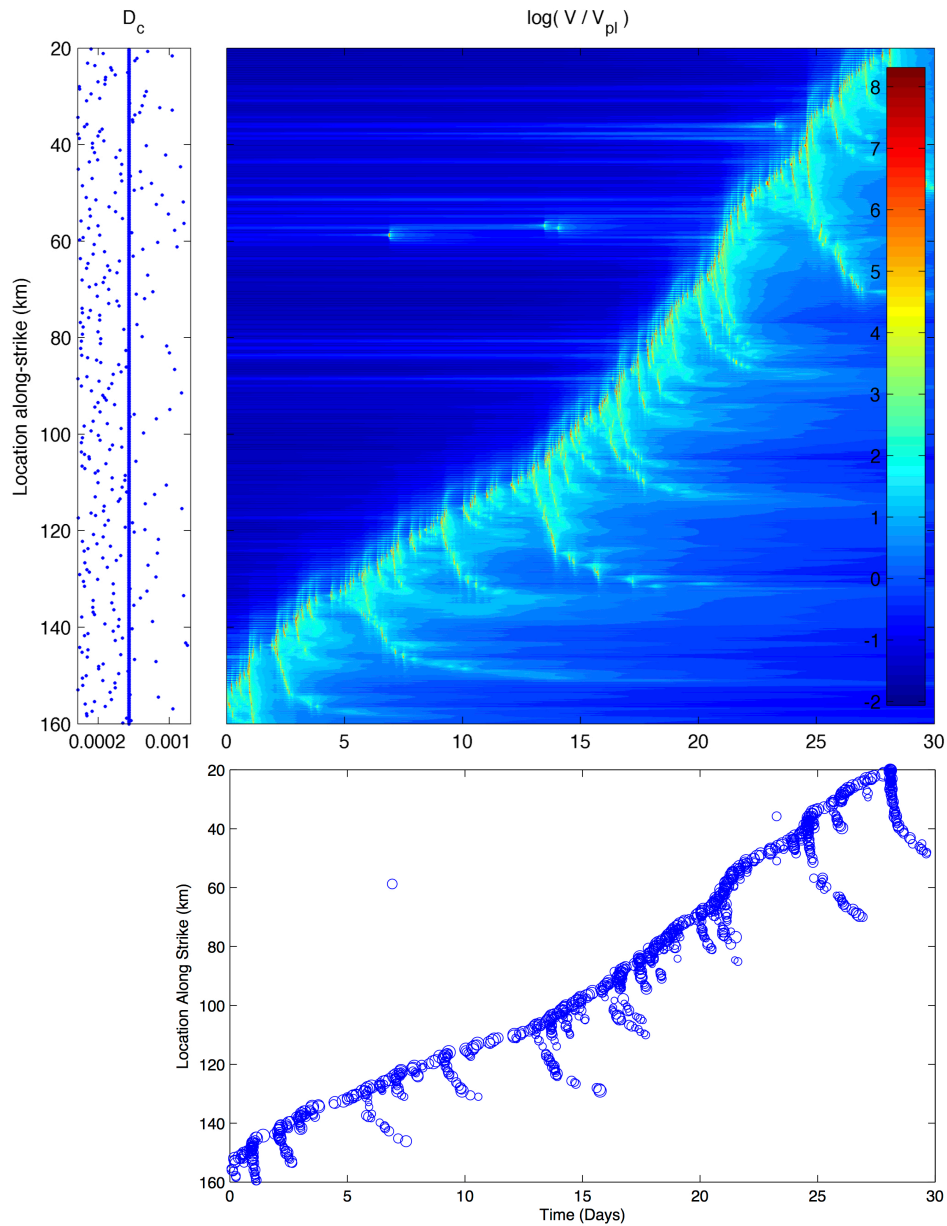


Figure 4.10: Top: modeled tremor forward migration and RTRs (rapid tremor reversals). Colors show the logarithmic slip rate normalized by plate loading rate  $V_{pl}$ . The left panel indicates the characteristic slip distance ( $D_c$ ) of the corresponding point on the fault. Every point with different  $D_c$  values are VW asperities (i.e. no velocity weakening to strengthening transition) and have a much higher  $(b - a)\sigma$  than the background. Bottom: seismicity distribution, each circle indicates a seismic event (slip velocity larger than ! mm/s) and its size is scaled with the magnitude.

tremor-driven-SSE model outperforms the SSE-driven-tremor model

Other observed tremor migration patterns, including tremor halting and branching

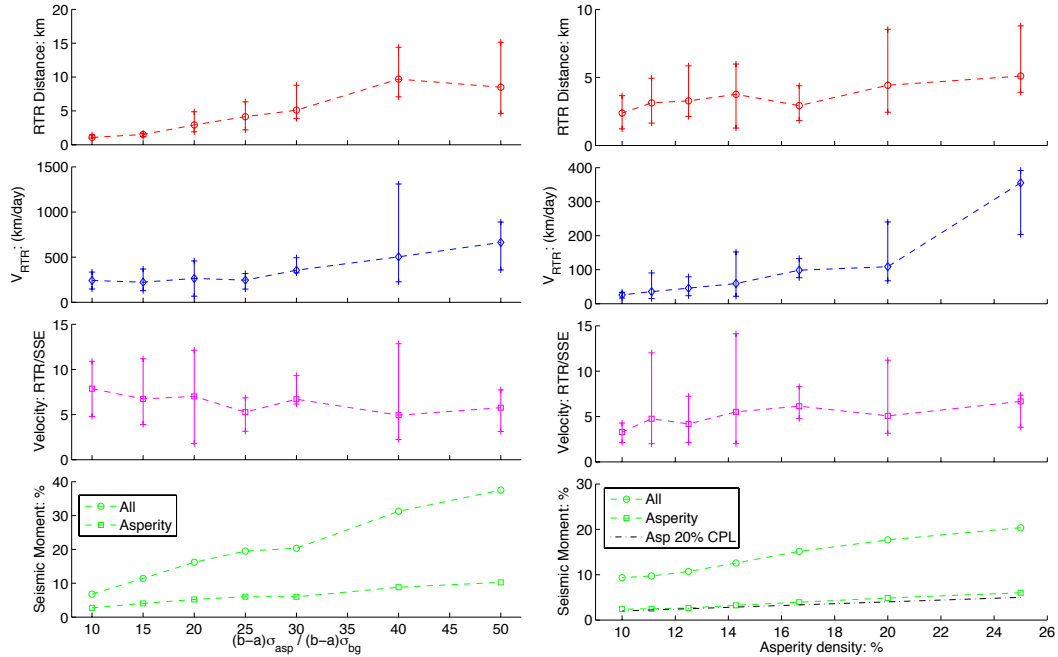


Figure 4.11: Effect of strength contrast (left) and density of asperities (right) on tremor properties. The strength contrast is quantified by the ratio of  $|b - a|\sigma$  inside and outside asperities. From top to bottom: RTR propagating distance, RTR propagation speed, ratio of  $V_{RTR}/V_{SSE}$ . Vertical bars show the range. Both RTR propagating distance and velocity increase with increasing  $b\sigma$  or asperity density, while  $V_{RTR}/V_{SSE}$  is not strongly affected by either values. Bottom: ratio of moment released seismically to total moment released during a tremor episode, for the whole fault (circles) and for asperities only (squares). Only a small fraction of the moment is released seismically. The dashed line indicates a coupling ratio of all the asperities of 20%.

(slower reversals), acceleration and deceleration (Kao et al. 2009), are also reproduced by both models. Figure 4.14 shows an example of modeled tremor halting and branching phenomena, where tremor propagation stops for hours, then resumes and branches.

### Nucleation of Rapid Tremor Reversals

We found that the characteristic slip distance  $D_c$  of the asperities plays a very important role in tremor migration patterns. For instance, RTRs occur rarely in our models because they nucleate at the asperities with largest  $D_c$  (Figure 4.15). We hypothesize that since these asperities are relatively strong, they do not break immediately at the arrival of the slow slip front, but are delayed by a period that depends on their relative stiffness. The delay allows neighboring asperities to

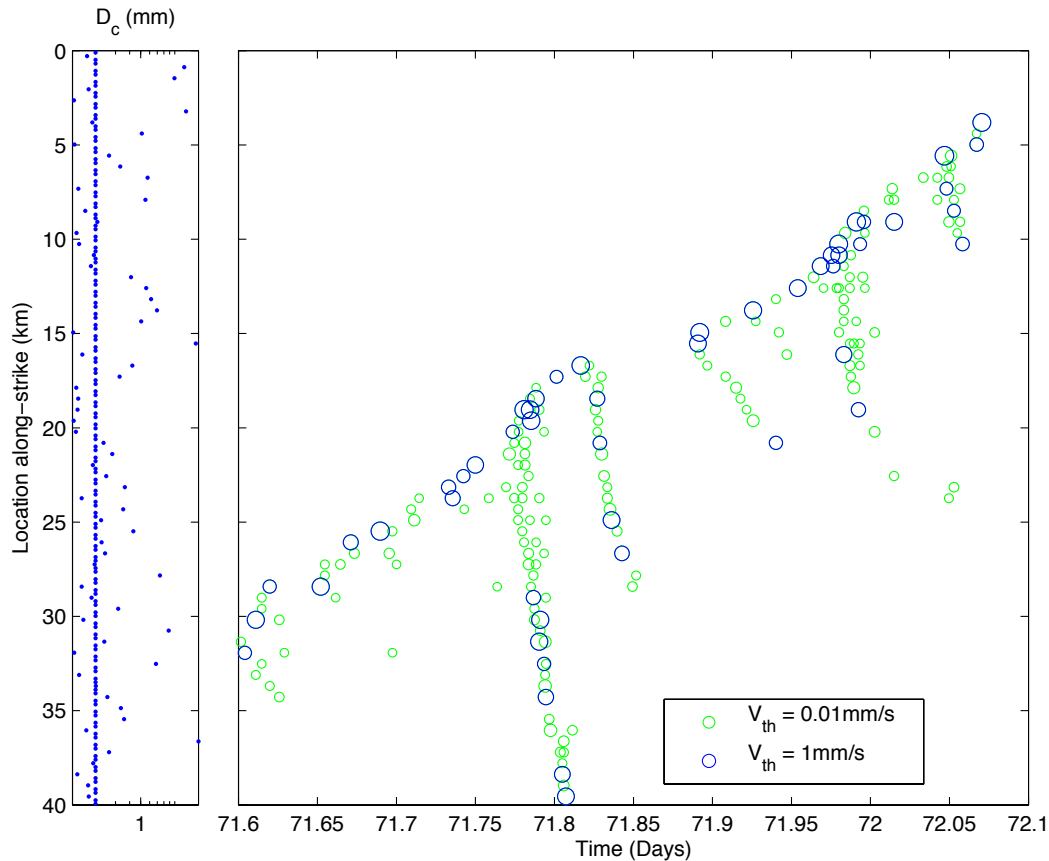


Figure 4.12: Higher  $V_{RTR}/V_{SSE}$  ratio, analogous to seismicity plot in Figure 4.10, achieved by tuning the cut-off velocity  $V_2$ . Green circles show the tremor events detected with a much lower velocity threshold. Note that more tremor activities are detected with the lower threshold, including RTR slowdown near day 72.

recover their strength and become again capable of triggering strong enough afterslip to sustain a cascading RTR. To confirm this idea, we designed a pair of controlled numerical experiments as shown in Figure 4.16. In the first simulation we set 10 very strong asperities with  $D_c$  value about one order of magnitude larger than that of the remaining asperities. All the resulting RTRs nucleated from these strong asperities. In the next simulation we removed three of the strong asperities (indicated by orange blocks in Figure 4.16). The RTRs that nucleated from those three asperities in the first simulation disappeared in the second simulation. Moreover, the other reversals that were either stopped or slowed down by these strong asperities in the first simulation, propagated faster and further beyond these removed asperity locations in the second simulation. The comparison results show that strong asperities not only nucleate RTRs but can also act as barriers that slow down or even stop RTRs.

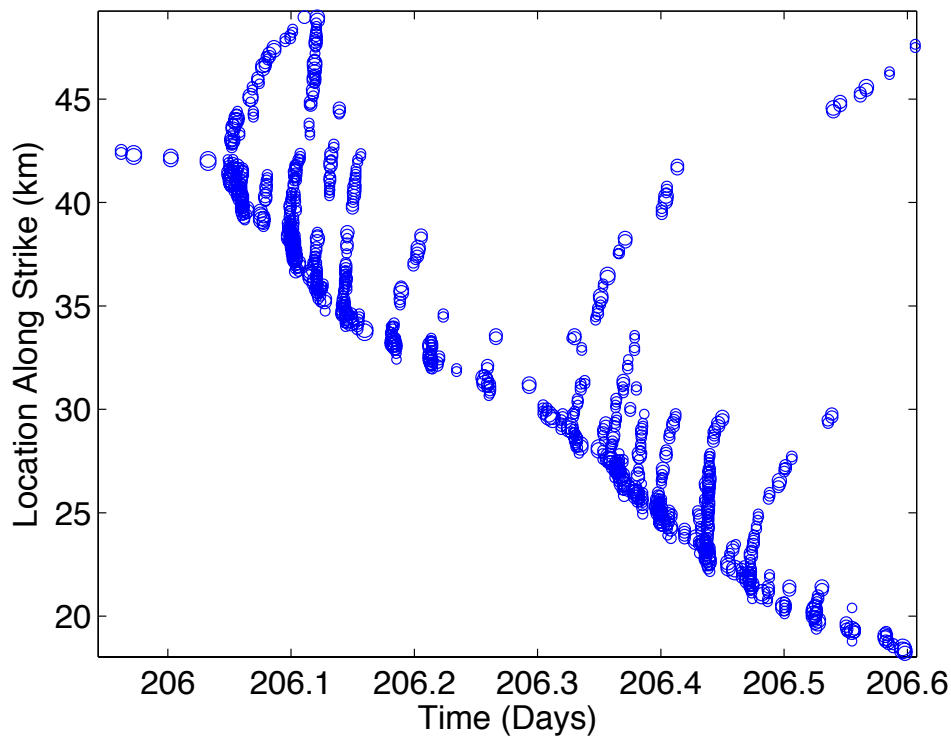


Figure 4.13: Tremor-driven-SSE model simulation. Various tremor migration patterns are also observed in this model. Figure analogous to Figure 4.10.

Tremor halting and branching occurs by the same mechanism but on asperities with even larger  $D_c$  (Figure 4.14) (either being a single asperity of very high  $D_c$  value, or a group of neighboring asperities with high  $D_c$ ). These very strong asperities induce longer delays before breaking, until the SSE slip velocity drops significantly. The low background slip velocity reduces the propagating speed of the subsequent post-seismic slip, resulting in a very slow tremor reversal which appears as a tremor halting and branching episode.

### **Effects of asperity properties on tremor migration speeds and seismic coupling**

Further study reveals that frictional properties inside the asperities control the RTR migration distance and speed, as well as the seismic coupling defined as the ratio of seismic moment to total moment (Figure 4.11).

Increasing the strength contrast (ratio of  $|b - a|\sigma$  inside and outside the asperities), while varying the asperities'  $D_c$  value to preserve the asperity criticalness, has very similar effects as decreasing the distance between asperities. In particular, both increase the propagation distance reached by RTRs and their migration speed.

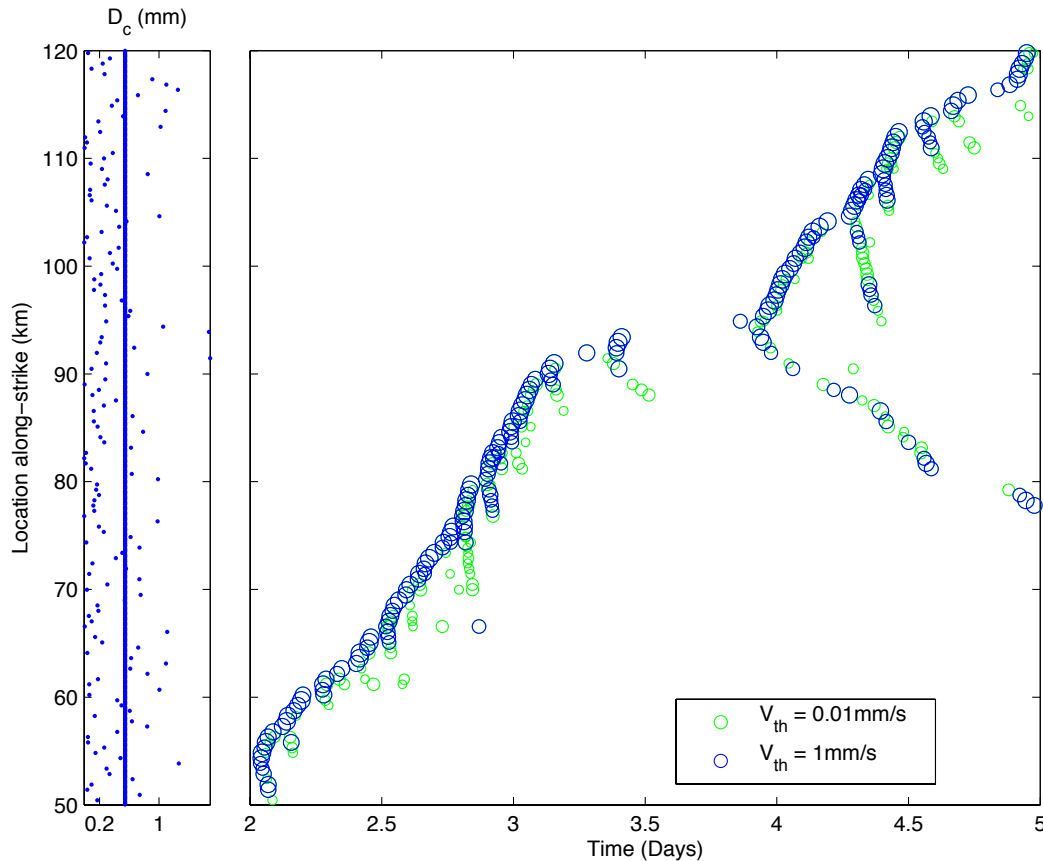


Figure 4.14: Tremor halting and branching. Tremor propagation halts for hours, and then resumes and branches. Different color in the seismicity plot shows results using different detection thresholds.

In contrast, the ratio  $V_{RTR}/V_{SSE}$  shows no strong correlation with these asperity properties. In addition, if the asperity distribution is too dense or the strength contrast is too large, the whole fault becomes seismic for both SSE-driven-tremor and tremor-driven-SSE model. If the asperity distribution is too sparse or the relative strength is too large, the interaction between asperities is too weak to produce RTRs in the SSE-driven-tremor model, and the whole fault creeps without transients in the tremor-driven-SSE model as in a sub-critical VW fault with  $W < L_c$ . These findings are consistent with those of the basic study of composite faults by [Luo and Ampuero \(2017\)](#).

In our models, the moment released seismically by asperities is only a small fraction, about 5% to 20% in most cases, of the total moment released by ETS events. Here we defined as seismic the moment cumulated while the local slip rate is higher than  $V_{dyn} \approx 1$  mm/s, and the total moment as the moment cumulated between the first

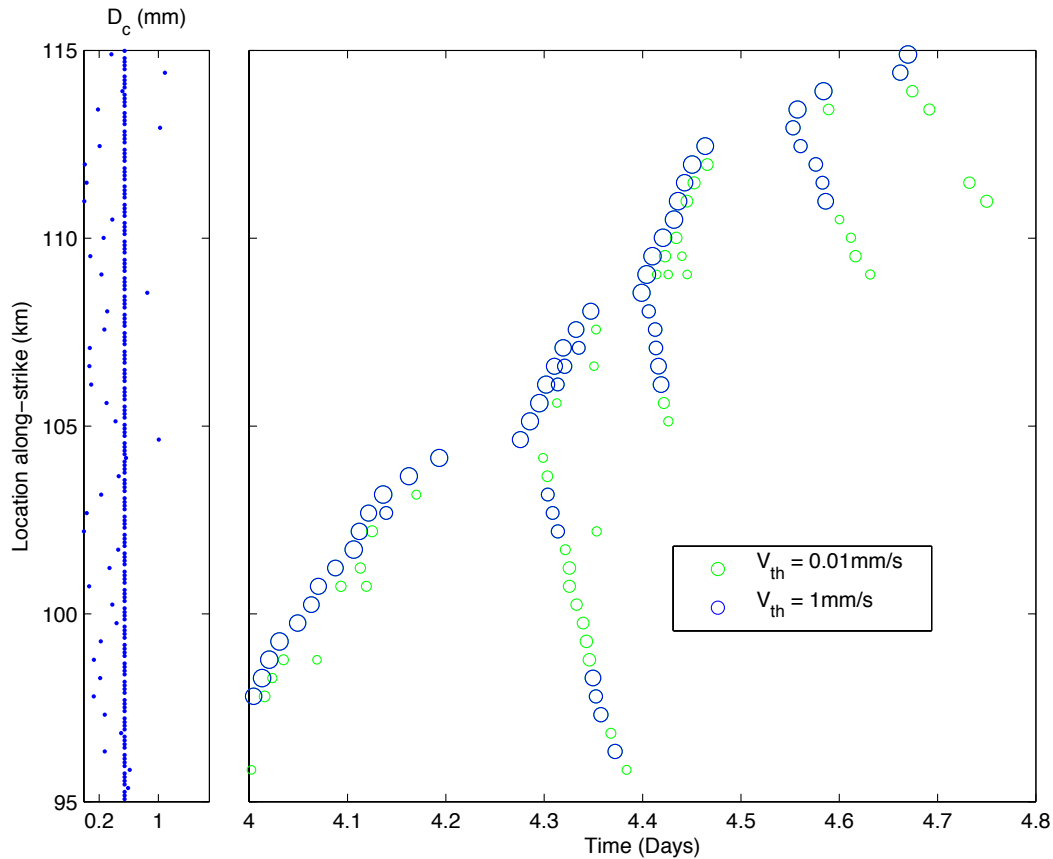


Figure 4.15: Nucleation of Rapid Tremor Reversals at "strong" asperities with large  $D_c$  values.

time fault slip rate at any point on the fault reaches 1 mm/s and the last time every point of the fault drops below 1 mm/s (Figure 4.11). The range of seismic coupling values is small, but at least one order of magnitude larger than observations. [Kao et al. \(2010\)](#) suggested the seismic coupling is of the order of 0.1% or less. Note that observational studies report a frequency-limited measure of the moment of tremor or LFE, which most likely represents a lower bound of the real tremor moment. It is also worth noting that in the tremor-driven-SSE model, despite being driven by asperity failures, most of the moment of ETS is aseismic, in the form of afterslip induced by asperity failure. We hypothesize that low seismic coupling is due to two reasons: the majority of the fault consists of VS materials and all the VW asperities are individually subcritical.

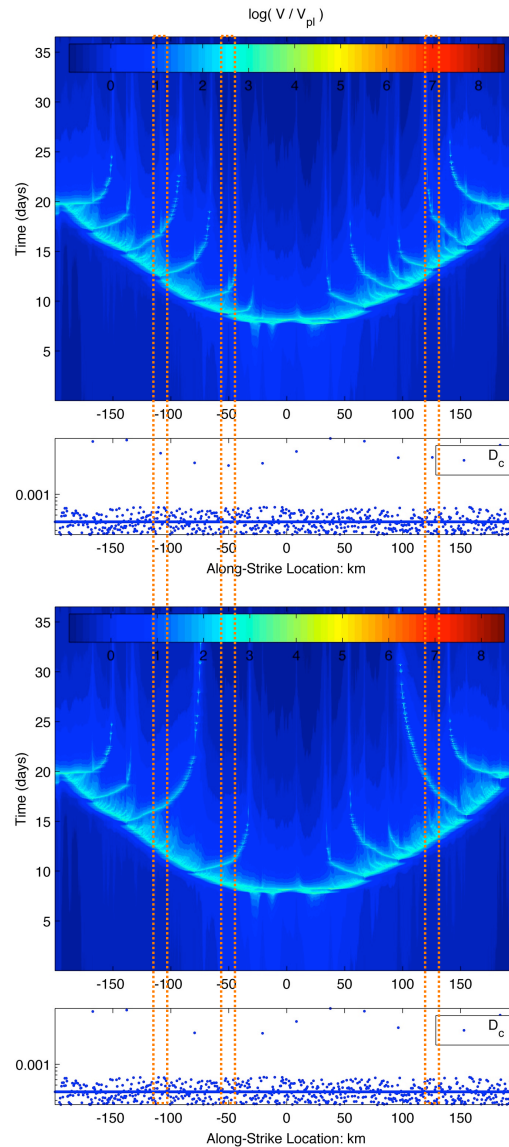


Figure 4.16: Test of the effect of strong asperities, analogous to Figure 4.10. Top: we set 10 very strong asperities with  $D_c$  value about one order of magnitude larger than a normal asperity. All RTRs nucleate from these strong asperities. Bottom: we removed three of the strong asperities (indicated by orange blocks). The three RTRs disappeared. The other reversals that were either stopped or slowed down by these asperities are able to propagate faster/further beyond these removed strong asperities. Strong asperities not only nucleate tremor reversals but also acts as a barrier to slow down or even stop the RTR propagation.

#### 4.4 Discussion

##### Comparison of SSE-driven-tremor and tremor-driven-SSE models

The two end-member models developed here have their own strengths and weaknesses. The SSE-driven-tremor model requires a more sophisticated friction law,

whose experimental support is limited, but allows SSEs without tremor, which has been reported in natural faults (e.g. SSE in New Zealand, [Peng and Gombert \(2010\)](#)). The tremor-driven-SSE model is based on a more conventional friction law and matches certain observations better and without fine tuning, in particular the ratio  $V_{RTR}/V_{SSE}$ . However it cannot explain observations of SSE without tremor, unless the fault is in a near-critical state in which asperity failures are too slow to be detected seismologically but strong enough to sustain an SSE.

We can identify potentially observable characteristics of the two models that can help distinguish them. Seismic coupling is not a discriminating characteristic. Given the small seismic moment attributed to tremors ([Kao et al. 2010](#)), the SSE-driven-tremor model is a widely accepted concept. However, as reported in section 4.3, in the tremor-driven-SSE model the fraction of moment released seismically is also small. A key difference between these two models is the asperity recurrence pattern. The stacked inter-event time between failures of a same asperity (normalized by the mean inter-event time) decays as a function of time  $t$  after its first break as  $1/\sqrt{t}$  in the SSE-driven-tremor model and as  $1/t$  in the tremor-driven-SSE model ([Figure 4.17](#)). An analysis of LFEs in the Mexico and Cascadia subduction zones by [Lengline et al. \(2017\)](#) reveals a  $1/t$  decay that favors the tremor-driven-SSE model ([See also Figure A.1](#)).

### **RTR propagation distance, velocity, and possible implications**

Our extended study shows that, in some simulations, RTRs tend to slow down when they propagate far enough (e.g. [Figures 4.10, 4.12 and 4.13](#)). According to the proportionality between tremor migration speed and the background slow slip velocity (Equation 4.11), this slowdown reflects the spatial distribution of the slip velocity of the SSE pulse. This model feature is consistent with observations by [Bletery et al. \(2017\)](#) of a tendency of tremor migration to slow down further behind the SSE front. This suggests that RTR migration speed provides a constraint on the spatial distribution of slip velocity in an SSE, and the distance reached by RTRs constrains the width of an SSE pulse.

### **Tremor rate as a proxy for local slip rate**

As discussed in section 4.1, obtaining observations of local slip rate of SSE with high spatial and temporal resolution is very important, but challenging with conventional methods such as slip inversion based on GPS data. Our simulations show that the tremor rate is proportional to the local slip rate (measured within background

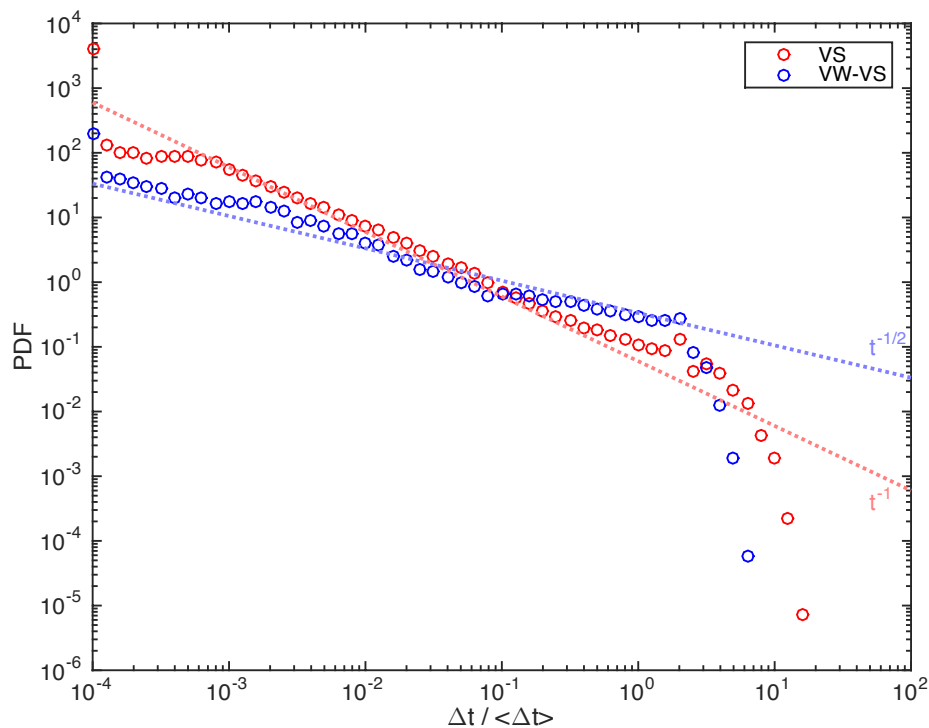


Figure 4.17: Probability density function of stacked tremor repeater recurrence interval distribution. Blue circles: SSE-driven-tremor model with friction with VW-VS transition in the matrix. Red circles: tremor-driven-SSE model with pure VS background. Both models have similar settings. Blue dashed line:  $1/\sqrt{t}$  decay. Red dashed line:  $1/t$  decay.

matrix) (Figure 4.18). If this relation is valid in nature, we can infer slip rate with fine spatial-temporal resolution by monitoring the tremor activity rate. The relation may be calibrated for instance on the basis of coarse-scale slip inferred from geodetic observations. While in practice the analysis might not be straightforward, it offers a new perspective on existing data that may help us probe SSEs with unprecedented resolution.

### Comparison to previous models

Several models have been previously proposed to explain subsets of observations of SSE and tremor. Here we discuss their relations to our model.

Various abstract models have been proposed to reproduce tremor signals. Ide et al. (2008)'s Brownian walk model reproduces the source time function of tremor swarms. Ide (2012) further developed the model to reproduce the large-scale tremor

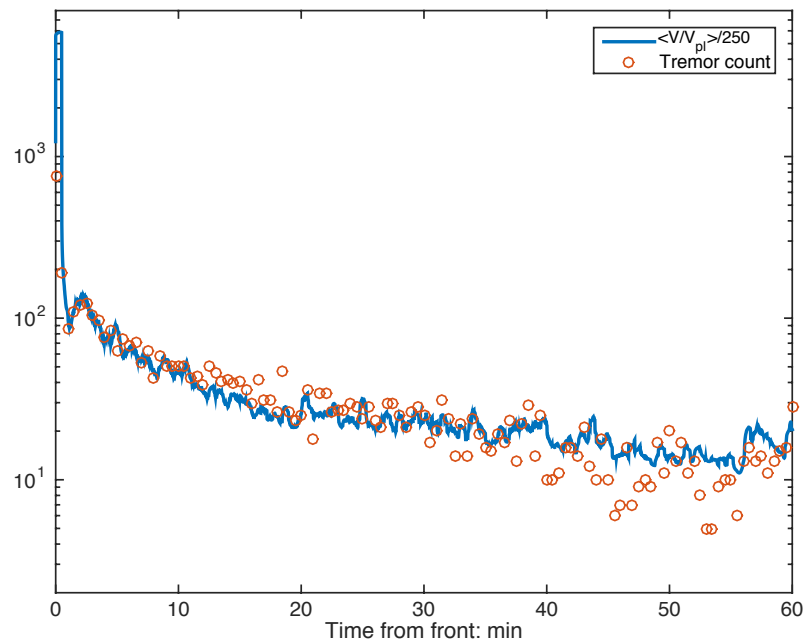


Figure 4.18: Tremor activity and local slip rate as a function of time during one tremor episode. Red circles: 30 second binned tremor activity as a function of time with respect to first local tremor activity. Blue solid curve: average local slip rate measured in matrix, aligned with local peak slip rate and low-pass filtered to 30 s. The tremor rate and local slip rate are in strikingly good agreement.

migration. [Daub et al. \(2011\)](#)'s fiber-bundle model reproduces the recurrence time and duration of tremor bursts. These models however do not reproduce hierarchical tremor migration patterns and the accompanying SSE.

Attempts have also been made to build analogies between tremors and other phenomena. [Gershenson et al. \(2011\)](#) developed analogies between tremor migration patterns and the propagation of dislocations in crystals. Given the similarity between the pulse-like mode of slow slip propagation and a crystal dislocation, this analogy is not surprising. They then applied to SSE and tremor phenomena the Frenkel-Kontorova model of crystal dislocations, which is similar to a Burridge-Knopoff model of a chain of spring-blocks with a periodically slip-dependent friction. An ingredient of their model, worth considering in our future models, is a certain roughness effect which may represent the actual waviness of the fault caused by continued slip.

Discrete models without explicit asperities and creep have also been proposed.

[Ben-Zion \(2012\)](#) treats tremor as the critical behavior of an inherently discrete model of a fault with zero net weakening. The model reproduces features of the incoherent background tremor activity in between SSEs, but not the organized migration patterns studied here. [Colella et al. \(2011, 2013\)](#)'s model reproduces the tremor migration patterns. Unlike our model, their model is inherently discrete and without quenched randomness. Thus the origin of RTR and along-dip tremor streaks in their model is not deterministic but stochastic, whereas our model reveals a clear mechanical origin of RTRs and along-dip tremor streaks. Also, the propagation velocity of RTRs and along-dip tremor streaks in their model are significantly slower than observations: both are at most 4 times the propagation velocity of the SSE, whereas observations are around 10 times and 100 times the SSE propagation velocity, respectively. The important difference is that in our model the asperities are embedded in a more stable fault matrix, so the tremor migration speeds are controlled by the propagation speed of transient creep between asperities, which in turn is directly proportional to the background slip velocity (section 4.2). In contrast, in their model the peak slip velocity is arbitrarily fixed.

Models without asperities but with creep have also been proposed. [Hawthorne and Rubin \(2013a,b\)](#) considered friction with VW-VS transition at increasing velocity and simulated SSEs in quantitative agreement with observations. They also modelled reversal fronts triggered and modulated by tidal loading. The difference between their SSE model and ours has been discussed in section 4.2. The propagation speed of RTRs (and the  $V_{RTR}/V_{SSE}$ ) in their model are at or below the lower values observed in Cascadia. Their model is not intended to simulate explicitly tremor activity. To develop further insight into tremor migration patterns, such models require additional assumptions about the relation between tremor rate and slow slip rate, which are evaluated in our model.

Homogeneous fault models with specially designed friction laws have also been considered. [Rubin \(2011\)](#) designed a rate-and-state friction law with two state variables to reproduce the different migration speeds of SSE along strike and along dip. However this model is not intended to reproduce tremor signals. Our models build upon earlier models of collective interaction of asperities: [Ariyoshi et al. \(2009, 2012\)](#) developed models of the whole subduction zone with a large megathrust asperity and tens of small asperities mimicking low frequency earthquake sources. In particular, [Ariyoshi et al. \(2012\)](#) introduced the important concept of swarms as a cascade of asperity failures. Also, [Ando et al. \(2010, 2012\)](#) presented an asperities-

in-matrix model in which the rheology of the matrix is Newtonian viscosity. Their model produces Parabolic Tremor Migration (PTM), and RTRs and forward tremor migration are the collective appearance of superimposed PTMs. However, in their model RTRs are not faster than forward migration: Rapid Tremor Forward (RTF) occurs and propagates even faster and further than their RTRs. Because of the assumption of linear viscosity which, in contrast to a rate-and-state friction model, leads to tremor propagation speed uncorrelated to the background slip velocity (Ando et al. (2012); see also Ida (1974) and Savage (1971)), their model is not expected to produce the hierarchy of forward, reverse and along-dip tremor migration with distinct speeds and the slow-down of RTRs. The slower forward migration in their model is actually an apparent effect of overlapping PTMs, but observations in Southwest Japan do not support such PTM pattern. Moreover, In Cascadia, RTFs have not been reported: observations in Cascadia show a clear trend of tremors propagating along strike with a rather steady velocity (Figure 4.1).

### **Model limitations and future work**

The quasi-dynamic approximation of elastodynamic effects adopted here is not a severe shortcoming, since the interaction of asperities in our model operates through slow creep fronts in the matrix, in which dynamic effects do not play an important role. Dynamic effects are more important inside asperities, but here we represented asperities as single cells without resolving the internal details of their rupture, which may not affect crucially the overall stress transfer to the creeping matrix that controls tremor migration patterns.

Whereas our conceptual model encompasses tremor migration along-strike and along-dip, the simulations presented here are 2D and are not intended to reproduce along-dip tremor migration. These 2D results do represent the essence of the conceptual model, as shown by its ability to reproduce forward and reverse along-strike tremor swarms with distinct migration speed. An animation of one of our 3D tremor and SSE simulations done with QDYN is shown in the supplemental materials. Further 3D results will be reported elsewhere that build up on the 2D results presented here, especially to set appropriate frictional properties and distributions of the asperities.

A further ingredient to consider in our model is non-planar fault geometry with anisotropic waviness, mimicking grooves aligned with the slip direction caused by wear and erosion of the megathrust interface. This can help address observations

suggesting that the along-dip tremor migration is actually parallel to the ancient slip direction in some subduction zones (e.g. Ide 2012).

#### 4.5 Conclusions

In this study, we developed mechanical models that reproduce imbricated tremor migration patterns along-strike accompanying slow slip events. The models represent a collection of frictionally unstable asperities embedded in a frictionally stable fault zone matrix, to investigate the role of fault heterogeneity and multi-asperity interactions mediated by creep. We focused on two models representing end-member behaviors: the SSE-driven-tremor model and the tremor-driven-SSE model. Both models reproduce qualitatively and quantitatively a broad range of observed characteristics of slow slip and tremor. In particular, they reproduce the distinct migration speed of forward tremor propagation and rapid tremor reversals (RTRs) and provide a mechanical relation between tremor migration speed and the slip velocity of the underlying slow slip.

Additional main findings of this work are as follows. (1) A model of SSE driven by tremor is viable, and seems favored by observations over the conventional model of tremor driven by SSE. While both models reproduce observed characteristics of SSE and tremor quantitatively, the tremor-driven-SSE model is based on a more conventional friction law and reproduces key observations better and without fine-tuning, in particular the range of RTR to SSE migration speeds and the decay of LFE inter-event times. (2) Tremor activity sheds light on fault rheology. The hierarchical patterns of tremor migration, with distinct propagation speeds in different directions, rule out a linear viscous rheology of the fault matrix and favor non-linear rheologies such as rate-and-state friction. The initiation points of RTRs also shed light on fault rheology at a fine scale: RTRs tend to nucleate at asperities that are stronger. Comparing RTR locations over multiple tremor episodes can probe temporal changes of local asperity strength which may be related, for instance, to changes of pore pressure. (3) A heterogeneous fault with a mixture of velocity-strengthening and velocity-weakening materials can generate SSEs robustly. This mechanism of SSE generation works without fine tuning, even under classical rate-and-state friction and with the slip law for state evolution, over a range of model parameter values much wider than in a homogeneous fault. It is enabled by collective interactions on heterogeneous faults with a broad range of stochastic asperity properties. (4) Tremor activity may be used to monitor SSE properties at a fine scale. Despite strong interactions between asperities, our models yield a simple relation between

tremor rate and the underlying slip rate. This provides quantitative support for an approach to constrain SSE slip rate at high spatial and temporal resolution through observations of tremor rates.

## References

- Ampuero, J. P. and A. M. Rubin (2008), “Earthquake nucleation on rate and state faults—Aging and slip laws”. *Journal of Geophysical Research: Solid Earth*, 113 (B1).
- Ampuero, J. P., O. Lengliné, Y. Luo, V. Durand, and J. A. Ruiz (2014), “Segmentation and Large-Scale Nucleation of the 2014 Pisagua Earthquake Sequence”. *AGU Fall Meeting Abstracts*.
- Ando, R., R. Nakata, and T. Hori (2010), “A slip pulse model with fault heterogeneity for low-frequency earthquakes and tremor along plate interfaces”. *Geophysical Research Letters*, 37 (10).
- Ando, R., N. Takeda, and T. Yamashita (2012), “Propagation dynamics of seismic and aseismic slip governed by fault heterogeneity and Newtonian rheology”. *Journal of Geophysical Research: Solid Earth*, 117 (B11).
- Ariyoshi, K., T. Hori, J. P. Ampuero, Y. Kaneda, T. Matsuzawa, R. Hino, and A. Hasegawa (2009), “Influence of interaction between small asperities on various types of slow earthquakes in a 3-D simulation for a subduction plate boundary”. *Gondwana Research*, 16 (3), pp. 534–544.
- Ariyoshi, K., T. Matsuzawa, J.P. Ampuero, R. Nakata, T. Hori, Y. Kaneda, R. Hino, and A. Hasegawa (2012), “Migration process of very low-frequency events based on a chain-reaction model and its application to the detection of preseismic slip for megathrust earthquakes”. *Earth, Planets and Space*, 64 (8), pp. 693–702.
- Bebout, G. E. and M. D. Barton (2002), “Tectonic and metasomatic mixing in a high-T, subduction-zone mélangé—insights into the geochemical evolution of the slab–mantle interface”. *Chemical Geology*, 187 (1), pp. 79–106.
- Ben-Zion, Y. (2012), “Episodic tremor and slip on a frictional interface with critical zero weakening in elastic solid”. *Geophysical Journal International*, 189 (2), pp. 1159–1168.
- Beroza, G. C. and S. Ide (2011), “Slow earthquakes and nonvolcanic tremor”. *Annual Review of Earth and Planetary Sciences*, 39, pp. 271–296.
- Bhattacharya, P. and A. M. Rubin (2014), “Frictional response to velocity steps and 1-D fault nucleation under a state evolution law with stressing-rate dependence”. *Journal of Geophysical Research: Solid Earth*, 119 (3), pp. 2272–2304.
- Bletery, Q., A. M. Thomas, J. C. Hawthorne, R. M. Skarbek, A. W. Rempel, and R. D. Krogstad (2017), “Characteristics of secondary slip fronts associated with slow earthquakes in Cascadia”. *Earth and Planetary Science Letters*, 463, pp. 212–220.
- Chen, K. H., R. M. Nadeau, and R. J. Rau (2007), “Towards a universal rule on the recurrence interval scaling of repeating earthquakes?” *Geophysical Research Letters*, 34 (16).

- Colella, H. V., J. H. Dieterich, and K. Richards-Dinger (2011), “Multi-event simulations of slow slip events for a Cascadia-like subduction zone”. *Geophysical Research Letters*, 38 (16).
- (2013), “Spatial and temporal patterns of simulated slow slip events on the Cascadia megathrust”. *Geophysical Research Letters*, 40 (19), pp. 5101–5107.
- Daub, E. G., D. R. Shelly, R. A. Guyer, and P. A. Johnson (2011), “Brittle and ductile friction and the physics of tectonic tremor”. *Geophysical Research Letters*, 38 (10).
- Dieterich, J. H. (1979), “Modeling of rock friction: 1. Experimental results and constitutive equations”. *Journal of Geophysical Research: Solid Earth*, 84 (B5), pp. 2161–2168.
- Dublanchet, P., P. Bernard, and P. Favreau (2013), “Interactions and triggering in a 3-D rate-and-state asperity model”. *Journal of Geophysical Research: Solid Earth*, 118 (5), pp. 2225–2245.
- Fagereng, Å. (2011), “Fractal vein distributions within a fault-fracture mesh in an exhumed accretionary mélange, Chrystalls Beach Complex, New Zealand”. *Journal of Structural Geology*, 33 (5), pp. 918–927.
- Fagereng, Å. and A. F. Cooper (2010), “The metamorphic history of rocks buried, accreted and exhumed in an accretionary prism: an example from the Otago Schist, New Zealand”. *Journal of Metamorphic Geology*, 28 (9), pp. 935–954.
- Fagereng, Å. and R. H. Sibson (2010), “Melange rheology and seismic style”. *Geology*, 38 (8), pp. 751–754.
- Field, E. H. et al. (2017), “A Synoptic View of the Third Uniform California Earthquake Rupture Forecast (UCERF3)”. *Seismological Research Letters*.
- Gershenzon, N. I., G. Bambakidis, E. Hauser, A. Ghosh, and K. C. Creager (2011), “Episodic tremors and slip in Cascadia in the framework of the Frenkel-Kontorova model”. *Geophysical Research Letters*, 38 (1).
- Ghosh, A., J. E. Vidale, J. R. Sweet, K. C. Creager, A. G. Wech, H. Houston, and E. E. Brodsky (2010), “Rapid, continuous streaking of tremor in Cascadia”. *Geochemistry, Geophysics, Geosystems*, 11 (12).
- Gomberg, J. et al. (2010), “Slow-slip phenomena in Cascadia from 2007 and beyond: A review”. *Geological Society of America Bulletin*, 122 (7-8), pp. 963–978.
- Hawthorne, J. C. and A. M. Rubin (2010), “Tidal modulation of slow slip in Cascadia”. *Journal of Geophysical Research: Solid Earth*, 115 (B9).
- (2013a), “Laterally propagating slow slip events in a rate and state friction model with a velocity-weakening to velocity-strengthening transition”. *Journal of Geophysical Research: Solid Earth*, 118 (7), pp. 3785–3808.

- Hawthorne, J. C. and A. M. Rubin (2013b), “Tidal modulation and back-propagating fronts in slow slip events simulated with a velocity-weakening to velocity-strengthening friction law”. *Journal of Geophysical Research: Solid Earth*, 118 (3), pp. 1216–1239.
- Horowitz, F. G. and A. Ruina (1989), “Slip patterns in a spatially homogeneous fault model”. *Journal of Geophysical Research: Solid Earth*, 94 (B8), pp. 10279–10298.
- Houston, H., B. G. Delbridge, A. G. Wech, and K. C. Creager (2011), “Rapid tremor reversals in Cascadia generated by a weakened plate interface”. *Nature Geoscience*, 4 (6), p. 404.
- Ida, Y. (1974), “Slow-moving deformation pulses along tectonic faults”. *Physics of the Earth and Planetary Interiors*, 9 (4), pp. 328–337.
- Ide, S. (2012), “Variety and spatial heterogeneity of tectonic tremor worldwide”. *Journal of Geophysical Research: Solid Earth*, 117 (B3).
- Ide, S., G. C. Beroza, D. R. Shelly, and T. Uchide (2007a), “A scaling law for slow earthquakes”. *Nature*, 447 (7140), p. 76.
- Ide, S., D. R. Shelly, and G. C. Beroza (2007b), “Mechanism of deep low frequency earthquakes: Further evidence that deep non-volcanic tremor is generated by shear slip on the plate interface”. *Geophysical Research Letters*, 34 (3).
- Ide, S., K. Imanishi, Y. Yoshida, G. C. Beroza, and D. R. Shelly (2008), “Bridging the gap between seismically and geodetically detected slow earthquakes”. *Geophysical Research Letters*, 35 (10).
- Ito, Y., K. Obara, T. Matsuzawa, and T. Maeda (2009), “Very low frequency earthquakes related to small asperities on the plate boundary interface at the locked to aseismic transition”. *Journal of Geophysical Research: Solid Earth*, 114 (B11).
- Kao, H., S. Shan, H. Dragert, and G. Rogers (2009), “Northern Cascadia episodic tremor and slip: A decade of tremor observations from 1997 to 2007”. *Journal of Geophysical Research: Solid Earth*, 114 (B11).
- Kao, H., K. Wang, H. Dragert, J. Kao, and G. Rogers (2010), “Estimating seismic moment magnitude (M<sub>w</sub>) of tremor bursts in northern Cascadia: Implications for the “seismic efficiency” of episodic tremor and slip”. *Geophysical Research Letters*, 37 (19).
- Kato, A., K. Obara, T. Igarashi, H. Tsuruoka, S. Nakagawa, and N. Hirata (2012), “Propagation of slow slip leading up to the 2011 Mw 9.0 Tohoku-Oki earthquake”. *Science*, 335 (6069), pp. 705–708.
- Kato, N. (2007), “Expansion of aftershock areas caused by propagating post-seismic sliding”. *Geophysical Journal International*, 168 (2), pp. 797–808.

- Lay, T., H. Kanamori, C. J. Ammon, K. D. Koper, A. R. Hutko, L. Ye, H. Yue, and T. M. Rushing (2012), “Depth-varying rupture properties of subduction zone megathrust faults”. *Journal of Geophysical Research: Solid Earth*, 117 (B4).
- Lengline, O., W.B. Frank, D. Marsan, and J. P. Ampuero (2017), “Imbricated slip rate processes during slow slip transients imaged by low-frequency earthquakes”.
- Liu, Y. and J. R. Rice (2005), “Aseismic slip transients emerge spontaneously in three-dimensional rate and state modeling of subduction earthquake sequences”. *Journal of Geophysical Research: Solid Earth*, 110 (B8).
- Lui, S. K. Y. and N. Lapusta (2016), “Repeating microearthquake sequences interact predominantly through postseismic slip”. *Nature communications*, 7, p. 13020.
- Luo, Y. and J. P. Ampuero (2017), “Stability and effective friction of heterogeneous faults with mixed velocity-weakening and velocity-strengthening rheology”.
- Luo, Y., J. P. Ampuero, P. Galvez, M. Ende, and B. Idini (2017), *QDYN: a Quasi-DYNAMIC earthquake simulator (v1.1)*. DOI: 10.5281/zenodo.322459. URL: <https://doi.org/10.5281/zenodo.322459>.
- Marone, C. (1998), “The effect of loading rate on static friction and the rate of fault healing during the earthquake cycle”. *Nature*, 391 (6662), p. 69.
- Meneghini, F., G. Di Toro, C. D. Rowe, J. C. Moore, A. Tsutsumi, and A. Yamaguchi (2010), “Record of mega-earthquakes in subduction thrusts: the black fault rocks of Pasagshak Point (Kodiak Island, Alaska)”. *Geological Society of America Bulletin*, 122 (7-8), pp. 1280–1297.
- Meng, L., A. Inbal, and J. P. Ampuero (2011), “A window into the complexity of the dynamic rupture of the 2011 Mw 9 Tohoku-Oki earthquake”. *Geophysical Research Letters*, 38 (7).
- Peng, Y., A. M. Rubin, M. G. Bostock, and J. G. Armbruster (2015), “High-resolution imaging of rapid tremor migrations beneath southern Vancouver Island using cross-station cross correlations”. *Journal of Geophysical Research: Solid Earth*, 120 (6), pp. 4317–4332.
- Peng, Z. and J. Gomberg (2010), “An integrated perspective of the continuum between earthquakes and slow-slip phenomena”. *Nature Geoscience*, 3 (9), pp. 599–607.
- Perfettini, H. and J. P. Ampuero (2008), “Dynamics of a velocity strengthening fault region: Implications for slow earthquakes and postseismic slip”. *Journal of Geophysical Research: Solid Earth*, 113 (B9).
- Rice, J. R. (1993), “Spatio-temporal complexity of slip on a fault”. *Journal of Geophysical Research: Solid Earth*, 98 (B6), pp. 9885–9907.
- Rogers, G. and H. Dragert (2003), “Episodic tremor and slip on the Cascadia subduction zone: The chatter of silent slip”. *Science*, 300 (5627), pp. 1942–1943.

- Rolandone, F., R. Bürgmann, and R. M. Nadeau (2004), “The evolution of the seismic-aseismic transition during the earthquake cycle: Constraints from the time-dependent depth distribution of aftershocks”. *Geophysical Research Letters*, 31 (23).
- Rouet-Leduc, B., C. Hulbert, N. Lubbers, K. Barros, C. Humphreys, and P. A. Johnson (2017), “Machine Learning Predicts Laboratory Earthquakes”. *arXiv preprint arXiv:1702.05774*.
- Rubin, A. M. (2008), “Episodic slow slip events and rate-and-state friction”. *Journal of Geophysical Research: Solid Earth*, 113 (B11).
- (2011), “Designer friction laws for bimodal slow slip propagation speeds”. *Geochemistry, Geophysics, Geosystems*, 12 (4).
- Rubin, A. M. and J. P. Ampuero (2005), “Earthquake nucleation on (aging) rate and state faults”. *Journal of Geophysical Research: Solid Earth*, 110 (B11).
- Ruina, A. (1983), “Slip instability and state variable friction laws”. *Journal of Geophysical Research: Solid Earth*, 88 (B12), pp. 10359–10370.
- Ruiz, S., M. Metois, A. Fuenzalida, J. Ruiz, F. Leyton, R. Grandin, C. Vigny, R. Madariaga, and J. Campos (2014), “Intense foreshocks and a slow slip event preceded the 2014 Iquique Mw 8.1 earthquake”. *Science*, 345 (6201), pp. 1165–1169.
- Savage, L. J. (1971), “Elicitation of personal probabilities and expectations”. *Journal of the American Statistical Association*, 66 (336), pp. 783–801.
- Segall, P., A. M. Rubin, A. M. Bradley, and J. R. Rice (2010), “Dilatant strengthening as a mechanism for slow slip events”. *Journal of Geophysical Research: Solid Earth*, 115 (B12).
- Shelly, D. R., G. C. Beroza, S. Ide, and S. Nakamura (2006), “Low-frequency earthquakes in Shikoku, Japan, and their relationship to episodic tremor and slip”. *Nature*, 442 (7099), p. 188.
- Shelly, D. R., G. C. Beroza, and S. Ide (2007), “Complex evolution of transient slip derived from precise tremor locations in western Shikoku, Japan”. *Geochemistry, Geophysics, Geosystems*, 8 (10).
- Shibazaki, B. and Y. Iio (2003), “On the physical mechanism of silent slip events along the deeper part of the seismogenic zone”. *Geophysical Research Letters*, 30 (9).
- Skarbek, R. M., A. W. Rempel, and D. A. Schmidt (2012), “Geologic heterogeneity can produce aseismic slip transients”. *Geophysical Research Letters*, 39 (21).
- Wech, A. G., K. C. Creager, H. Houston, and J. E. Vidale (2010), “An earthquake-like magnitude-frequency distribution of slow slip in northern Cascadia”. *Geophysical Research Letters*, 37 (22).

Yabe, S. and S. Ide (2017), “Slip-behavior transitions of a heterogeneous linear fault”. *Journal of Geophysical Research: Solid Earth*, 122 (1), pp. 387–410.

*Appendix A***SUPPLEMENTS**

An animation preview of 3D tremor migrations:

*[https://github.com/ydluo/qdyn/wiki/Simulation\\_Cascadia\\_Tremor](https://github.com/ydluo/qdyn/wiki/Simulation_Cascadia_Tremor)*

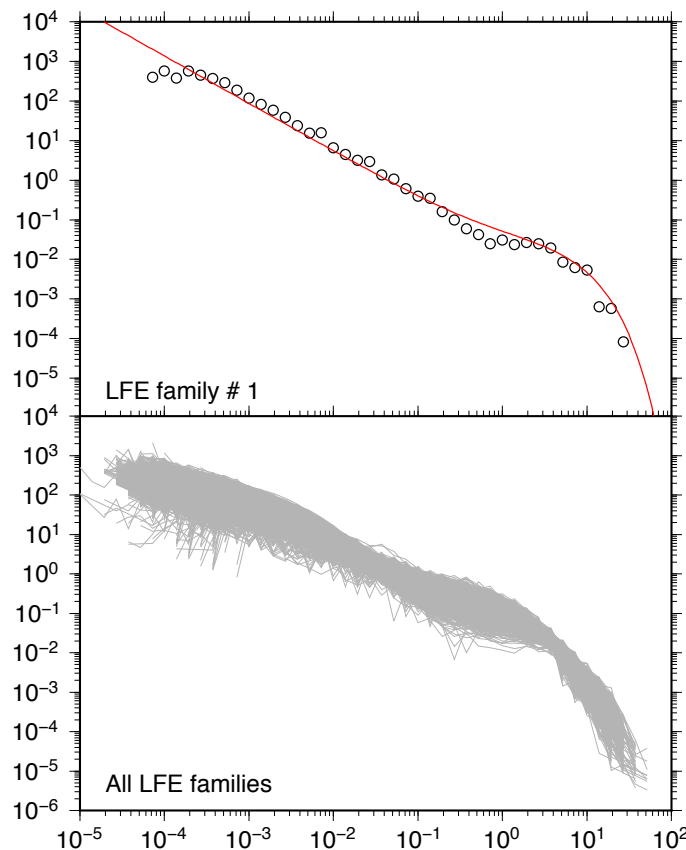


Figure A.1: (From written communication with [O. Lengliné 2015](#), see also [Lengline et al. \(2017\) supplemental materials](#)). PDF (probability density function) of LFE families from Mexico, analogous to Figure 4.17. Top: repeater recurrence interval distribution from a selected LFE family in Mexico subduction (black circles) and fit (red curve), the fit shows a transition from a power-law decay with an exponent  $q = 1.0$  ( $1/t$ ) at short time scale to an exponential decay. Bottom: superposed pdfs computed for all families (gray curves). The same shape of the pdf is recovered for all families.

*Appendix B*NUMERICAL CODE: QDYN - QUASI-DYNAMIC  
EARTHQUAKE SIMULATOR



# QDYN

Quasi-DYNamic earthquake simulator

V 1.1

## User's Manual



[github.com/ydluo/qdyn](https://github.com/ydluo/qdyn)

## Developers

[Yingdi Luo](#) (Caltech Seismo Lab, USA)  
[Jean-Paul Ampuero](#) (Caltech Seismo Lab, USA)  
Percy Galvez (AECOM, Switzerland)  
Martijn van den Ende (Utrecht University, the Netherlands)  
Benjamin Idini (University of Chile)

Last modification on 08/29/2017

[Click here](#) to access the most recent version

# Table of contents

## [1 Introduction](#)

- [1.1 Summary](#)
- [1.2 Main features](#)
- [1.3 Documentation](#)
- [1.4 Support](#)
- [1.5 License](#)
- [1.6 Acknowledgements](#)
  - [1.6.1 Code contributions](#)
  - [1.6.2 Funding](#)
- [1.7 Suggested references](#)

## [2 Installation](#)

- [2.1 Requirements](#)
- [2.2 Download QDYN](#)
  - [2.2.1 Stable versions](#)
  - [2.2.2 Development version](#)
  - [2.2.3 Pre-compiled executables](#)
- [2.3 Install QDYN](#)
- [2.4 Update QDYN](#)

## [3 Model assumptions](#)

- [3.1 Model geometry](#)
- [3.2 Boundary conditions](#)
- [3.3 Friction laws](#)

## [4 Running a simulation](#)

- [4.1 The Matlab wrapper](#)
- [4.2 Simulation parameters structure \(pars\)](#)
- [4.3 Output structures \(ot, ox\)](#)
- [4.4 Examples](#)
  - [4.4.1 A simple 2D example](#)
  - [4.4.2 Two asperities interacting](#)
  - [4.4.3 3D simulations](#)

## [5 Optimizing Performance](#)

- [5.1 Running simulations outside the Matlab environment](#)
- [5.2 Managing parallel computing](#)
  - [5.2.1 OpenMP](#)

### [5.2.2 MPI](#)

### [5.3 Managing outputs of large simulations](#)

## [6 Visualizing simulation results](#)

## [7 Coupling with the dynamic rupture code SPEC3D](#)

### [7.1 The QDYN-SPEC3D Bridge \(QSB\)](#)

### [7.2 Pre-requisites](#)

### [7.3 The master QSB Bash Script](#)

### [7.4 The job request script for clusters with job scheduling system](#)

### [7.5 How to run fully coupled QDYN-SPEC3D simulations](#)

### [7.6 QSB Example: fully-dynamic earthquake cycle simulation on a heterogeneous fault](#)

# 1 Introduction

## 1.1 Summary

**QDYN** is a boundary element software to simulate earthquake cycles (seismic and aseismic slip on tectonic faults) under the quasi-dynamic approximation (quasi-static elasticity combined with radiation damping) on faults governed by rate-and-state friction and embedded in elastic media.

QDYN includes various forms of rate-and-state friction and state evolution laws, and handles non-planar fault geometry in 3D and 2D media, as well as spring-block simulations. Loading is controlled by remote displacement, steady creep or oscillatory load. In 3D it handles free surface effects in a half-space, including normal stress coupling. The medium surrounding the fault is linear, isotropic and elastic, and may be uniform or (in 2D) contain a damaged layer.

QDYN implements adaptive time stepping, shared-memory parallelization, and can deal with multi-scale earthquake cycle simulations with fine details in both time and space. It is equipped with a user-friendly Matlab interface and graphical output utilities.

## 1.2 Main features

- Rate-and-state friction, with velocity cut-offs, aging and slip laws
- Arbitrarily heterogeneous frictional properties
- Slow and fast, aseismic and seismic slip transients (adaptive timestep)
- Non-planar faults (currently limited to variable dip, rectangular elements)
- 3D, 2D and 1D (spring-block)
- Steady and oscillatory loads
- Normal stress coupling
- Faults surrounded by damaged zones
- Matlab wrapper and graphic output display utilities
- Parallelized for shared memory systems (OpenMP)
- Parallelized for distributed memory systems (MPI)
- Fully coupled with SPECFEM3D via QSB (QDYN-SPECFEM Bridge)

## 1.3 Documentation

Documentation for QDYN is available through the following resources:

- This User's Manual. [Click here](#) to access the most recent version.
- The `examples` directory contains several examples, some have a `README` file

- The Matlab tools provided with the QDYN package are documented through Matlab's help. For instance `help qdyn` provides an overview of the usage of the `qdyn` Matlab interface.
- The `ToDo` file contains a list of known issues and features that we plan to implement in the future.

## 1.4 Support

The QDYN development team offers online support to users who report bugs, installation problems, documentation issues, feature requests, or questions about QDYN usage by submitting “issues” at <https://github.com/ydluo/qdyn/issues>.

In particular, please do not contact the QDYN developers directly by email.

Before submitting an issue please make sure that:

- you have read the QDYN documentation (see section 1.3)
- you are running the most recent version of QDYN (see sections 2.2 and 2.4)
- your problem has not been treated in previous issues. You can browse and search the list of [closed issues](#)

New issues are submitted via <https://github.com/ydluo/qdyn/issues/new>. Please include all information needed to reproduce your problem: input files, operating system, compiler, QDYN version.

## 1.5 License

**This software is freely available for academic research purposes. If you use QDYN please include proper attributions to its authors and cite one of the references in section 1.7 in your scientific papers and reports.**

This program is free software: you can redistribute it and/or modify it under the terms of the GNU General Public License as published by the Free Software Foundation, either version 3 of the License, or (at your option) any later version.

This program is distributed in the hope that it will be useful, but WITHOUT ANY WARRANTY; without even the implied warranty of MERCHANTABILITY or FITNESS FOR A PARTICULAR PURPOSE. See the GNU General Public License for more details.

You should have received a copy of the GNU General Public License along with this program. If not, see <http://www.gnu.org/licenses/>.

## 1.6 Acknowledgements

### 1.6.1 Code contributions

QDYN outgrew from a 2D code written by Allan Rubin (Princeton University) in the early 2000s. The main developers are Jean Paul Ampuero and Yingdi Luo. Bryan Riel contributed the double-FFT version. Percy Galvez contributed to the MPI parallelization. Martijn van den Ende contributed code fixes for Octave. Benjamin Idini implemented damaged fault zones.

The subroutines implementing Okada's formulas were provided by Shinichi Miyazaki (Kyoto University). They include subroutines written by Y. Okada.

The FFT subroutines are based on the [General Purpose FFT Package](#) written by Takuya Ooura (Kyoto University).

### 1.6.2 Funding

The development of QDYN has been supported by the US National Science Foundation, the Southern California Earthquake Center and Japan's Nuclear Regulation Authority (formerly Japan Nuclear Energy Safety Organization).

## 1.7 Suggested references

Y. Luo, J. P. Ampuero (2011), Numerical Simulation of Tremor Migration Triggered by Slow Slip and Rapid Tremor Reversals, AGU Fall Meeting 2011 Abstract S33C-02

Y. Luo, J. P. Ampuero (2012), Simulation of Complex Tremor Migration Patterns, AGU Fall Meeting 2012 Abstract S44B-02

Y. Luo, J. P. Ampuero, K. Miyakoshi and K. Irikura (2017) *Surface effects on earthquake moment-area scaling relations* PAGEOPH, Topical Volume on "Best Practices in Physics-based Fault Rupture Models for Seismic Hazard Assessment of Nuclear Installations", [doi:10.1007/s00024-017-1467-4](https://doi.org/10.1007/s00024-017-1467-4)

Y. Luo, J. P. Ampuero, P. Galvez, M. Ende and B. Idini. (2017). *QDYN: a Quasi-DYNamic earthquake simulator (v1.1) [Data set]*. Zenodo. [doi:10.5281/zenodo.322459](https://doi.org/10.5281/zenodo.322459)

## 2 Installation

### 2.1 Requirements

- [Make](#) and [Subversion](#) or [GIT](#) facilitate code installation and updates. Both are standard Linux tools.
- A Fortran compiler.
- MPI (e.g. [MPICH](#), [Open MPI](#)) linked to your Fortran compiler (mpif90).
- Matlab or Octave.

We mostly develop and use QDYN with Linux, the Intel Fortran compiler (ifort) and Matlab. The code has been successfully compiled and used on Windows or Mac, with gfortran and Octave.

### 2.2 Download QDYN

QDYN is hosted on [GitHub](#). You have several options to download it:

#### 2.2.1 Stable versions

You can download stable versions from the [releases page](#).

#### 2.2.2 Development version

You can download development versions of QDYN. These usually contain bug fixes and new features, but they may not be fully tested yet (use it at your own risk and please report issues - see section 1.4).

QDYN is managed under a version control system compatible with both [Subversion](#) (SVN) and [Git](#). You can choose either option. In GitHub, Git is the recommended, native version control system. SVN is provided through an interface (Git-SVN bridge) that does not implement all the features of SVN. To switch between Git and SVN you need to checkout the code again from scratch.

To download for the first time the latest development version of QDYN execute the following SVN command:

```
svn checkout https://github.com/ydluo/qdyn qdyn-read-only
```

or the following GIT command:

```
git clone https://github.com/ydluo/qdyn qdyn-read-only
```

This creates a directory `qdyn-read-only` which contains the whole QDYN package. You can create a directory with a different name.

### 2.2.3 Pre-compiled executables

You can download pre-compiled QDYN executables for Windows or Mac OS directly from [this link](#). However, these may not be most recent versions and they may run slower than if you compile the code by yourself.

## 2.3 Install QDYN

1. Move to the `src` directory
2. Modify the section “User Settings” of file `Makefile` following the instructions and examples therein:
  - a. In section 1, set the variable `EXEC_PATH = [the path to your executable file]`. If you leave the default value (recommended) the executable file `qdyn` is placed in the `src` directory. If you change this variable (not recommended), you must set the `EXEC_PATH` input variable accordingly when you call `qdyn.m`.
  - b. In section 2, adjust your Fortran compiler settings: set the variables `F90 = [your compiler name]`, `OPT = [your compiler optimisation flags]` and `PREPROC = [your compiler option to enable preprocessing]`. Intel Fortran (`ifort`) is the default compiler, but settings for several commonly used compilers are provided. Note that specific optimisation flags need to be set to enable parallelization through OpenMP (see section 4.2.1).
3. Set the parameters in the section “User Settings” of `constants.f90` following the instructions therein
4. Run `make`
5. If in step 2 you changed the path or name of the executable file, modify accordingly the line `status = system('~/.bin/qdyn')` of file `qdyn.m`

## 2.4 Update QDYN

If you are using the development version, after the first-time checkout you can update the package by executing the following command in your `qdyn-read-only` directory:

```
svn update
```

Any source file that you have modified will be flagged as “conflicted” by SVN, and you will be prompted to select a conflict resolution method. You can preserve your modifications by selecting the option `mc` (“mine-conflict”). This is particularly useful to preserve your user settings in `Makefile` and `constants.f90` (otherwise you would need to repeat the steps in the [“Install QDYN” section](#)). For that purpose, the following command eliminates the interactive prompt:

```
svn update --accept mc
```

If you are using GIT instead of SVN, update QDYN with the following command:

```
git fetch
```

GIT automatically marks conflicts and you have to fix them manually following the instructions in the [GITHUB help pages](#).

## 3 Model assumptions

### 3.1 Model geometry

QDYN handles the following geometries:

- “0D fault”, a spring-block model
- “Finite 1D fault” embedded in a 2D unbounded elastic medium. The fault is straight and actually infinitely long, but its frictional part is confined to a segment of finite length  $L$ ,  $x \in [-L/2, L/2]$ .
- “Periodic 1D fault” embedded in a 2D unbounded elastic medium. The fault is infinitely long but has a spatially periodic distribution of friction parameters, normal stress and slip with spatial period  $L$ . The modeled segment is  $x \in [-L/2, L/2]$ . We account approximately for a characteristic length of the slip distribution in the third dimension (the axis normal to the modeled 2D medium) by assuming slip has a sinusoidal pattern over a length  $W$  in the third dimension. This is effectively a 1.5D approximation, in which  $W$  is a proxy for the seismogenic width of a 2D fault.
- 1D fault bisecting an elastic slab
- 2D fault embedded in a 3D elastic space or half-space. The fault surface has fixed strike, but possibly depth-dependent dip. The fault is infinite but only a finite area is frictional.

Periodic 1D faults can be embedded in a homogeneous medium or in a damaged fault zone model. The latter is a heterogeneous medium composed of two materials: a layer of damaged material with constant thickness in contact with the fault embedded in an intact material.

### 3.2 Boundary conditions

Spring-block models are loaded by an imposed load-point velocity. On continuum faults, the frictional segment is loaded by slip imposed along the remaining, non-frictional part of the fault. In all cases, the imposed loading is composed of a steady velocity and an oscillatory component.

The fault shear strength equals the normal stress times the friction coefficient. In rate-and-state friction, the fault shear stress is always equal to the strength.

In the quasi-dynamic approximation adopted in QDYN, fault stresses are the sum of static elastic stresses induced by slip and a radiation damping stress. The latter approximates the effect of wave radiation: it represents exactly the stresses induced by waves radiated in the direction normal to the fault but not the complete elastodynamic stresses.

### 3.3 Friction laws

The friction coefficient is governed by one of the following rate-and-state laws:

- Conventional rate-and-state

$$\mu(V, \theta) = \mu^* + a \ln(V/V^*) + b \ln(\theta V^*/D_c)$$

- Rate-and-state with cut-offs

$$\mu(V, \theta) = \mu^* - a \ln(1 + V_1/V) + b \ln(1 + \theta V_2/D_c)$$

The state variable follows one of the following evolution equations:

- Aging law

$$d\theta/dt = 1 - \theta V/D_c$$

- Slip law

$$d\theta/dt = -\theta V/D_c \ln(\theta V/D_c)$$

All frictional properties can be spatially heterogeneous.

## 4 Running a simulation

### 4.1 The Matlab wrapper

The core of QDYN is a Fortran code. While the format of its input and output files is well defined, we find it more convenient to set up the input parameters, perform simulations and read the output data within the Matlab environment through the wrapper function `qdyn.m`. You first need to set in Matlab the full path to the `src` directory, for instance:

```
addpath ~/qdyn-read-only/src
```

**Tip for Mac users:** if you get an error message related to gfortran libraries (e.g. `libgfortran.3.dylib`) when running `qdyn` in Matlab, do:

```
setenv('DYLD_LIBRARY_PATH', '/usr/local/bin/')
```

The second argument should be the path to your gfortran libraries (sometimes `/opt/local/lib/libgcc`).

The general usage syntax is:

```
[pars,ot,ox] = qdyn(mode, [parsin], ['Property',Value,...])
```

The default input values can be listed by executing:

```
pars = qdyn('set')
```

The input parameters are:

<i>mode</i>	<p>One of the following execution modes:</p> <ul style="list-style-type: none"> <li>'set'      Outputs the default parameter structure (<i>pars</i>) or overrides it with fields present in the structure <i>parsin</i> or with <i>Property/Value</i> pairs</li> <li>'write'    Sets parameters and writes the qdyn input file</li> <li>'run'      Sets parameters, writes the input file and runs a simulation</li> <li>'read'     Reads parameters and outputs from a previous simulation</li> </ul>
<i>parsin</i>	Parameter structure to override the default parameters (see section 3.2 for details)
' <i>Property</i> '	Name of a field to be set in the parameter structure (see section

	3.2)
<i>Value</i>	Value to override the default value and the value in <i>parsin</i>

The output variables are:

<i>pars</i>	Structure containing the parameters (see section 3.2)
<i>ot</i>	Structure containing time series outputs, global or at selected points (see section 3.3)
<i>ox</i>	Structure containing snapshot outputs, i.e. quantities over the whole fault, output at selected times (see section 3.3)

## 4.2 Simulation parameters structure (*pars*)

The parameters in the structure *pars*, that can be set through 'parsin' or 'Prop/Value' pairs are:

### Parameters defining the geometry of the problem and loading:

<i>MESHDIM</i>	Dimension of the problem: 0 = Spring-block model 1 = 1D fault in a 2D elastic medium 2 = 2D fault in a 3D elastic medium 4 = Same as 2 but fault stresses computed via 2D-FFT (works only if the grid spacings and dip angle are uniform)
<i>MU</i>	Shear modulus (Pa)
<i>LAM</i>	Elastic modulus lambda for 3D simulations (Pa)
<i>VS</i>	Shear wave speed (m/s). If <i>VS=0</i> , radiation damping is turned off
<i>D</i>	Damage level = $1 - (\text{damaged shear modulus}) / (\text{intact shear modulus})$  Currently implemented only for <i>MESHDIM=1</i> and <i>FINITE=0</i>

<i>H</i>	<p>If <math>D &gt; 0</math>, half-thickness of the fault damage zone (m)  If <math>D = 0</math>, half-thickness of an elastic slab bisected by a fault</p> <p>Currently implemented only for <math>MESHDIM=1</math> and <math>FINITE=0</math></p>
<i>L</i>	<p>If <math>MESHDIM=1</math>, <math>L</math> is the fault length (or spatial period)  If <math>MESHDIM=0</math>, <math>MU/L</math> is the spring stiffness</p>
<i>FINITE</i>	<p>Boundary conditions when <math>MESHDIM=1</math></p> <p>0 = Periodic fault: the fault is infinitely long but slip is spatially periodic with period <math>L</math>, loaded by steady displacement at distance <math>W</math> from the fault</p> <p>1 = Finite fault: the fault is infinitely long but only a segment of length <math>L</math> has rate-and-state friction, the rest has steady slip. If running the code with this option gives the error message “kernel file src/kernel_1.tab is too short”, you should create a larger “kernel file” with the matlab function <i>TabKernelFiniteFlt.m</i></p> <p>2 = Symmetric periodic fault: like option 0 but slip is symmetric relative to the first element</p> <p>3 = Symmetric finite fault: like option 1 but slip is symmetric relative to the first element. This can be used to set a free surface next to the first element</p>
<i>W</i>	Distance between displacement loading and fault, only if $MESHDIM=1$ and $FINITE=0$
<i>DIP_W</i>	Fault dip angle (degree) if $MESHDIM=2$ or $4$ . If depth-dependent, values must be given from deeper to shallower depth.
<i>Z_CORNER</i>	Fault bottom depth (m, negative down) if $MESHDIM=2$ or $4$
<i>SIGMA_CPL</i>	Normal stress coupling: 0 = disable, 1 = enable
<i>APER</i>	Amplitude of additional time-dependent oscillatory shear stress loading (Pa)
<i>TPER</i>	Period of oscillatory loading (s)

### Rate-and-state friction parameters:

<i>A</i>	Direct effect coefficient
<i>B</i>	Evolution effect coefficient
<i>DC</i>	Characteristic slip distance (m)
<i>MU_SS</i>	Reference steady-state friction coefficient
<i>V_SS</i>	Reference steady-state slip velocity (m/s)
<i>TH_SS</i>	Reference steady-state state (s). The default is $TH\_SS=DC/V\_SS$ .
<i>RNS_LAW</i>	Type of rate-and-state friction law: 0 = original  1 = with cut-off velocities $V1$ and $V2$
<i>V1</i>	Cut-off velocity of direct effect (m/s)
<i>V2</i>	Cut-off velocity of evolution effect (m/s), controls the transition from weakening to strengthening when $a < b$ . $V2$ should be $\leq V1$ .
<i>THETA_LAW</i>	Type of evolution law for the state variable: 0 = ageing law in the "no-healing" approximation 1 = ageing law 2 = slip law

**Initial conditions:**

<i>SIGMA</i>	Initial effective normal stress (Pa). Remains constant unless $SIGMA\_CPL = 1$
<i>V_0</i>	Initial slip velocity (m/s)
<i>TH_0</i>	Initial state (s)

**Discretization and accuracy parameters:**

<i>N</i>	Number of fault elements if $MESHDIM=1$
----------	---

NX	Number of fault elements along-strike, in 3D
NW	Number of fault elements along-dip, in 3D
NPROCS	Number of processors if running in parallel with MPI (only implemented for MESHDIM=2 and FFT_TYPE=1)
DW	Along-dip length (m) of each element, from deep to shallow
TMAX	Threshold for stopping criterion: Final simulation time (s) when NSTOP=0 Slip velocity threshold (m/s) when NSTOP=3
NSTOP	Stopping criterion <ul style="list-style-type: none"> <li>0 = Stop at t=TMAX (s)</li> <li>1 = Stop at end of slip localization phase</li> <li>2 = Stop soon after first slip rate peak</li> <li>3 = Stop when slip velocity exceeds TMAX (m/s)</li> </ul>
DTRY	First trial timestep (s)
DTMAX	Maximum timestep (0=unrestricted)
ACC	Solver accuracy

**Output control parameters:**

OX_SEQ	Type of snapshot outputs <ul style="list-style-type: none"> <li>0 = All snapshots in a single output file (fort.19)</li> <li>1 = One output file per snapshot (fort.1001, ...)</li> </ul>
NXOUT	Spatial interval for snapshot outputs (in number of elements)
NTOUT	Temporal interval (in number of time steps) for snapshot outputs
OX_DYN	Output specific snapshots of dynamic events defined by thresholds on peak slip velocity DYN_TH_ON and DYN_TH_OFF (see below)

	<p>0 = Disable</p> <p>1 = Enable outputs for event #i:  Event start: fort.19998+3i  Event end: fort.19999+3i  Rupture time: fort.20000+3i</p>
NXOUT_DYN	Spatial interval (in number of elements) for dynamic snapshot outputs
DYN_TH_ON	Peak slip rate threshold (m/s) to define the beginning of a dynamic event
DYN_TH_OFF	Peak slip rate threshold (m/s) to define the end of a dynamic event
IC	Index of selected element for time series outputs
IOT	Indices of elements for additional time series outputs: set $IOT(i)=1$ to enable time series outputs at the i-th element. By default, $IOT(i)=0$ and this output is not done. Each element has a separate output file named <code>fort.xxxxxx</code> , where <code>xxxxxx</code> is an index (different than <code>i</code> ) that starts at 10001 and is incremented by 1 for each selected element. For instance, if $IOT=[0\ 0\ 1\ 1]$ , the output of elements $i=3$ and $i=4$ are in files <code>fort.10001</code> and <code>fort.10002</code> , respectively.
IASP	Auxiliary flags for elements (will not affect outputs, identification purpose only. e.g you can set elements of the VS part to -1 and VW to 0 and particular points of interests like asperities to numbers you want to use )

### Parameters for integration with dynamic code:

DYN_FLAG	Integration with dynamic code <p>0 = Disable</p> <p>1 = Enable: stop QDYN at the DYN_SKIP+1-th event with seismic moment &gt; DYN_M</p>
DYN_M	Target seismic moment of a dynamic event
DYN_SKIP	Number of dynamic events to skip (warm up cycles)

### 4.3 Output structures (*ot*, *ox*)

The outputs are:

pars	Structure containing the same fields as <i>parsin</i> (see above) plus the positions of the fault elements (X,Y,Z)
ot	<p>Structure of time series outputs, with the following fields:</p> <p>t            Output times (s)</p> <p>locl        Localization length (distance between stressing rate maxima)</p> <p>cl           Crack length (distance between slip rate maxima)</p> <p>p            Seismic potency</p> <p>pdot        Seismic potency rate</p> <p>Outputs at the fault location with maximum slip rate:</p> <p>xm        Location of maximum slip rate</p> <p>v            Maximum slip rate</p> <p>th          State variable theta</p> <p>om        (slip rate)*theta/DC</p> <p>tau        Shear stress</p> <p>d          Slip</p> <p>Outputs at selected fault element with index IC:</p> <p>vc        slip rate</p> <p>thc       state variable</p> <p>omc      (slip rate)*theta/DC</p> <p>tauc      shear stress</p> <p>dc        slip</p>

ox	Structure of snapshot outputs, with the following fields:																		
	<table> <tr> <td>x</td> <td>fault coordinates</td> </tr> <tr> <td>t</td> <td>output times</td> </tr> <tr> <td>v</td> <td>slip rate</td> </tr> <tr> <td>th</td> <td>state variable theta</td> </tr> <tr> <td>vd</td> <td>slip acceleration</td> </tr> <tr> <td>dtau</td> <td>shear stress relative to initial stress</td> </tr> <tr> <td>dtaud</td> <td>shear stress rate</td> </tr> <tr> <td>d</td> <td>slip</td> </tr> <tr> <td>sigma</td> <td>effective normal stress</td> </tr> </table>	x	fault coordinates	t	output times	v	slip rate	th	state variable theta	vd	slip acceleration	dtau	shear stress relative to initial stress	dtaud	shear stress rate	d	slip	sigma	effective normal stress
x	fault coordinates																		
t	output times																		
v	slip rate																		
th	state variable theta																		
vd	slip acceleration																		
dtau	shear stress relative to initial stress																		
dtaud	shear stress rate																		
d	slip																		
sigma	effective normal stress																		

## 4.4 Examples

### 4.4.1 A simple 2D example

This example is in directory `examples/uniform_slip`. It's a 2D run with uniform slip and initial velocity slightly above steady state. In Matlab:

```
% get default parameters:
p = qdyn('set');
% reset some parameters:
p.N = 16; p.TMAX = 6e9; p.V_0=1.01*p.V_SS;
% run:
[p,ot,ox] = qdyn('run',p);
```

The estimated simulation time is shorter than 10 s on a single thread machine. Let's plot some outputs. Slip velocity as a function of time:

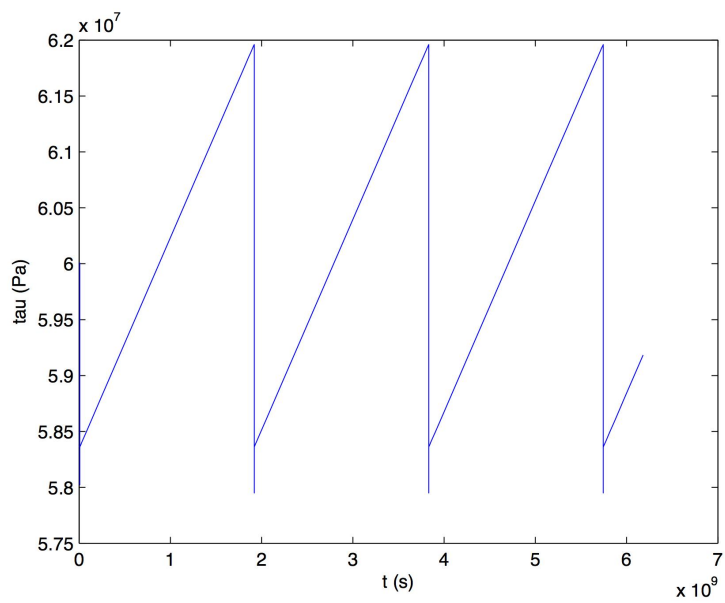
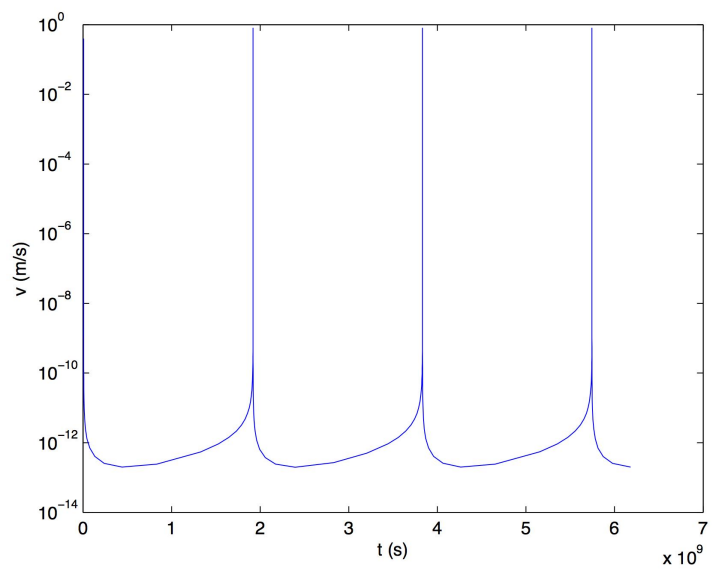
```
semilogy(ot.t,ot.v); xlabel('t (s)'); ylabel('v (m/s)')
```

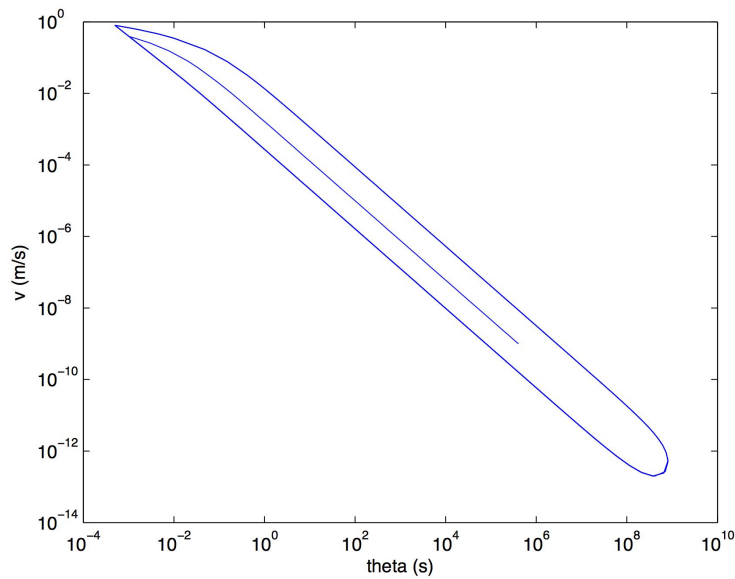
Plot shear stress as a function of time:

```
plot(ot.t,ot.tau); xlabel('t (s)'); ylabel('tau (Pa)')
```

Visualize the convergence to a limit cycle in a state-velocity plot:

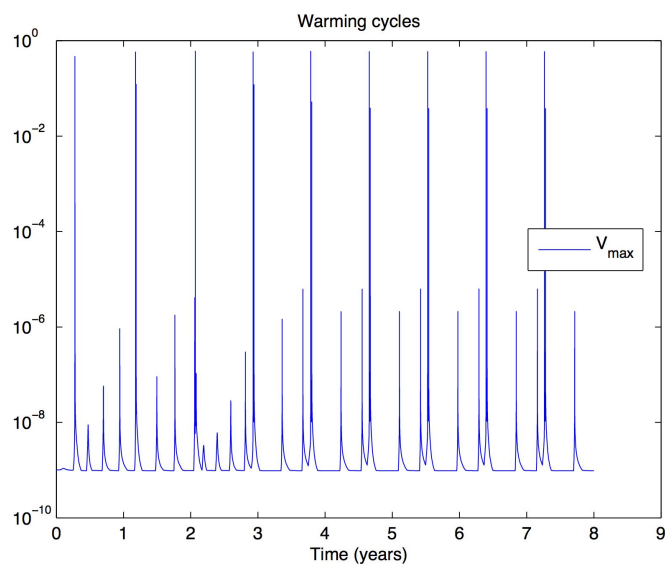
```
loglog(ot.th,ot.v); xlabel('theta (s)'); ylabel('v (m/s)')
```

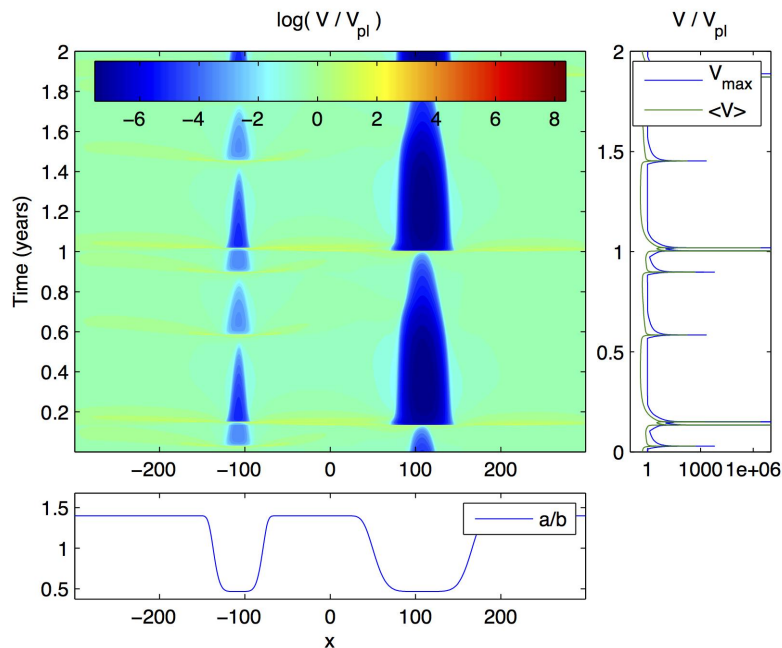




#### 4.4.2 Two asperities interacting

This example is in directory `examples/double_asperities`. A velocity-weakening asperity interacts with a smaller asperity. Both are embedded in a velocity-strengthening (creeping) fault. When the large asperity breaks, its post-seismic slip propagates bi-laterally and triggers rupture of the small asperity. During the interseismic period of the large asperity, the smaller asperity breaks twice with a decreasing recurrence interval. The estimated simulation time is about 6 mins on a single thread machine.



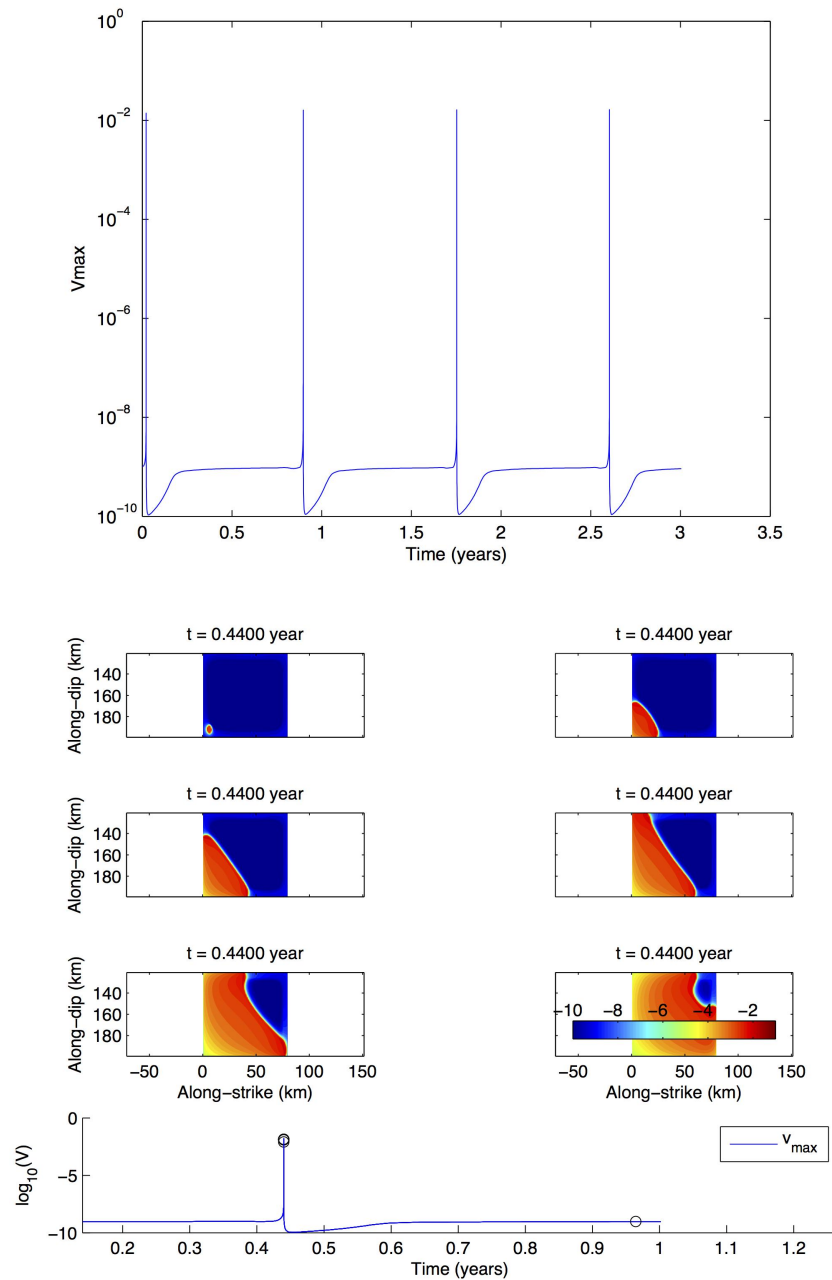


#### 4.4.3 3D simulations

An upper-layer Matlab wrapper for the base-layer Matlab wrapper `qdyn.m` is recommended for complicated simulations. We have included some examples for reference:

a) A 3D simulation: `examples/3d_fft/test_3dfft.m`

The estimated simulation time is about 10 mins on a single thread machine for the first earthquake cycle. The figures shown below are for a complete multi-cycle simulation, comprising 4 warm-up cycles and one cycle output.



b) A simplified model for the Tohoku earthquake (2D along-dip and 3D simulations): [examples/Tohoku](#)

For more examples and real-world applications please refer to the [wiki pages on the QDYN website](#).

## 5 Optimizing Performance

### 5.1 Running simulations outside the Matlab environment

To run simulations outside the Matlab environment, e.g. when computing on an HPC cluster: run first the Matlab wrapper only to generate the input file `qdyn.in`, then run the `qdyn` executable outside Matlab.

### 5.2 Managing parallel computing

#### 5.2.1 OpenMP

For 3D simulations on 2D faults (`MESHDIM=2` or `4`), QDYN is parallelized for shared memory multi-processor systems with OpenMP. Before compiling the code, you should set the specific compiler optimisation flags that enable OpenMP, as described in the `Makefile` (see step 2.b in section 2.3). Before performing parallel simulations, you should set the following environment variable:

```
setenv OMP_NUM_THREADS 8
```

This command allows QDYN to run on 8 threads, which will roughly speed up calculations by a factor of 8. The number of threads should be set according to demand. In general, set this value to the maximum number of threads available on your shared memory system.

#### 5.2.2 MPI

For 3D simulations with `MESHDIM=2`, QDYN can run in parallel in distributed memory clusters with MPI. The number of processors must be set in the variable `p.NPROCS`.

### 5.3 Managing outputs of large simulations

QDYN by default outputs results as a single ASCII file (`fort.19`). In most multi-cycle 3D simulations this file is very large. It is then helpful to set `OX_SEQ = 1` when calling `qdyn.m`, to generate separate “ox” files outputs for each snapshot (`fort.1001, ...`). Also, setting `OX_DYN = 1` will automatically detect seismic events (according to parameters `DYN_TH_ON` and `DYN_TH_OFF`) and generate 3 snapshots for each event.

## 6 Visualizing simulation results

The QDYN software package includes several Matlab scripts to visualize simulation results in directory `utils/post_processing`. These scripts are all self-documented:

<code>plot_default.m</code>	Plots slip rate of a 2D problem (along-strike)
<code>plot2d_slip.m</code>	Plots slip of a 2D problem (along-dip)
<code>plot3d_m.m</code>	Plots a sequence of snapshots of slip rate of a 3D simulation
<code>plot3d_faultview_3.m</code>	Plots several snapshots of slip rate for 3D simulation in a single figure

## 7 Coupling with the dynamic rupture code SPECFEM3D

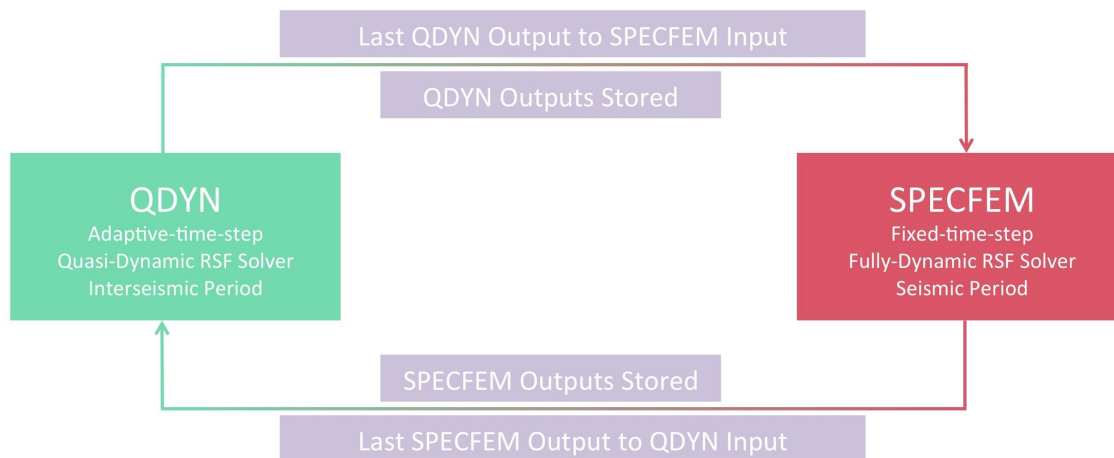
### 7.1 The QDYN-SPECFEM Bridge (QSB)

[SPECFEM3D](#) is a software for dynamic rupture simulations. It is fully dynamic, i.e. it accounts for inertial effects that are important during earthquakes. However, it is based on a solver with fixed time-step, which cannot be applied to interseismic and postseismic periods involving slow, quasi-static (aseismic) deformation.

QDYN is a software for quasi-dynamic earthquake cycle simulations. It is based on the quasi-dynamic approximation and an adaptive time-step solver. These features are accurate and efficient during periods of aseismic slip, but their accuracy degrades during seismic slip, especially in the presence of severe fault weakening mechanisms at high slip rates.

QSB, the QDYN-SPECFEM3D Bridge module, is a two-way interface between the QDYN and the SPECFEM3D softwares. QSB employs each of these codes in its optimal usage conditions to enable efficient and accurate simulations of multiple earthquake cycles containing periods of both seismic (SPECFEM3D) and aseismic (QDYN) slip. The figure below summarizes the QSB workflow and its pattern of data communication between the two codes.

### QSB: The QDYN-SPECFEM BRIDGE



### 7.2 Pre-requisites

- Obtain a copy of the development version of SPECSEM, which includes a rate-and-state friction solver, using the following git command: `git clone https://github.com/geodynamics/specsem3d.git -b devel`.
- Obtain a copy of the QDYN package on [GITHUB](#) following the instructions described in the [QDYN online manual](#). The QSB module is made of Bash and Matlab scripts contained in directory `QSB/` of the QDYN package.

### 7.3 The master QSB Bash Script

`QDYN_SPECSEM_bridge.sh` is the master script of the QSB. It utilizes the matlab script `QDYN_to_SPECSEM_RSFF.m` to convert the output of QDYN right before an earthquake into a SPECSEM3D input and the matlab script `SPECSEM_to_QDYN_RSFF.m` to convert the output of SPECSEM3D right after an earthquake into a QDYN input.

The control variables in `QDYN_SPECSEM_bridge.sh` are:

<code>N_core_allco</code>	Number of cores in the SPECSEM simulations
<code>N_loop</code>	Number of earthquakes to be simulated
<code>QDYN_dir_work</code>	QDYN working directory
<code>QDYN_dir_out_store</code>	Directory to store QDYN outputs. Data for each earthquake is stored in a separate sub-directory named <code>QDYN_dir_out_store/run{i}</code> where $i = 1, 2, \dots$ is the earthquake index
<code>SPECSEM_dir_work</code>	SPECSEM working directory
<code>SPECSEM_dir_in</code>	Directory where QDYN will place output data for SPECSEM input
<code>SPECSEM_dir_out</code>	Directory where SPECSEM will place output data for QDYN input
<code>SPECSEM_dir_out_store</code>	Directory to store SPECSEM outputs. Data for each earthquake is stored in a separate sub-directory named <code>SPECSEM_dir_out_store/run{i}</code> where $i = 1, 2, \dots$ is the earthquake index

### 7.4 The job request script for clusters with job scheduling system

In most High Performance Computing clusters, job requests are submitted through a job scheduling system to better utilize computational resources. The sample job request script `QSB/run_bridge_sh` should serve on most clusters. The script may need slight modifications to adapt it to your job scheduler; please contact your system administrator to get the most accurate information.

To submit your QSB job, edit the control variables in `run_bridge_sh`, then run the following command:

```
qsub run_bridge_sh
```

The control variables in the request script `run_bridge_sh` are:

<code>#PBS -l nodes=[nodes]</code>	Number of cores requested, set to the same value as <code>N_core_allco</code>
<code>#PBS -l walltime=[time]</code>	Total walltime requested, process will be terminated briefly after exceeding the requested walltime total queue time is in general assessed over cluster load and <code>[nodes]*[time]</code>
<code>#PBS -m bae</code>	Get notifications at the beginning, end and if an error occurs
<code>#PBS -M [email]</code>	Notification will be sent to [email]
<code>./QDYN-SPECFEM_bridge.sh &gt; [output]</code>	Submit job QDYN-SPECFEM_bridge.sh, simulation progress stores (and overwrites previous existing) outputs file [output]

## 7.5 How to run fully coupled QDYN-SPECFEM simulations

**Step 1:** Setup the control variables in the script `QDYN_SPECFEM_bridge.sh`. For most variables you can keep the default settings found in the script.

**Step 2:** Setup a QDYN simulation and generate first-run input file `qdyn.in`

**Step 3:** Setup the SPECFEM simulation:

- Set switch `RATE_AND_STATE = .true.` and `RSF_HETE = .true.` in `src/specfem3D/DATA/Par_file_faults`
- Generate a spectral element mesh with same fault geometry (length, width and dip angles) as the QDYN mesh. The average spacing of the GLL nodes on the fault in the SPECFEM mesh should be similar to the grid

- spacing in QDYN. If the coordinates of the SPECIFEM mesh have different starting values, set the values of `x_off`, `y_off` and `z_off` in `QDYN_to_SEM_RSF_f.m` and `SEM_to_QDYN_RSF.m` accordingly.
- Partition the mesh into `N_core_allco` processors. Please refer to the SPECIFEM3D manual for further details.
  - Set values in `DATA/Par_file`, `DATA/Par_file_faults` and `DATA/FAULT_STATIONS` accordingly. You can find sample files in `EXAMPLES/fault_examples/tpv103/DATA`. Set the 6 components of CMT source in file `CMTsolution` to 0. Please refer to the SPECIFEM3D manual for further details.
  - Set the `t_dyn` = [SPECIFEM target simulation time] in `QDYN_to_SEM_RSF_f.m`
  - Store the coordinates of the fault nodes in file `nodesonfault`, a text file with five columns, IX IZ X Y Z, where IX and IZ are node indices (actually not used) and X, Y and Z are fault node coordinates with units of meters. An example is provided in `QSB/nodesonfault`. You can create it by making a test run of SPECIFEM and then running the provided matlab script `SEM_write_nodesonfault.m`.

**Step 4:** Run the Bash script `QDYN_SPECIFEM_bridge.sh`, or, on a cluster with scheduler, submit the request script `run_bridge.sh`. You can modify `run_bridge.sh` to change the name of the progress monitoring file (default is `QSB/output.txt`) and your email notification address (see previous section)

**Step 5:** Monitor the simulation progress in file `QSB/output.txt`. Once the simulation of `N_loop` earthquakes is over, an email notification will be sent

**Step 6:** Process the outputs, matlab scripts `plot_QDYN_seq.m` and `plot_SEM_seq.m` are provided for your convenience to visualize QDYN and SPECIFEM outputs, respectively.

## ***7.6 QSB Example: fully-dynamic earthquake cycle simulation on a heterogeneous fault***

**Step 1:** We want to run SPECIFEM with 108 cores and simulate 2 earthquakes, so we set `N_core_allco=108`, and `N_loop=2` in the script `QDYN_SPECIFEM_bridge.sh`. We keep the default values for other variables.

**Step 2:** We prepare the example `hete_3d_ss.m` to run QDYN simulations on a 3D strike-slip fault with 50 km depth and 512 km length and heterogeneous frictional properties. In the script we set `p.OX_SEQ=1`, `p.OX_DYN=1` and `p.DYN_TH_ON=0.1` to generate a snapshot output `fort.20001` when the maximum slip rate reaches 0.1 m/s. We also set `p.NSTOP=3` and

`p.TMAX=0.1001` to stop QDYN soon after, when maximum slip rate reaches 0.1001 m/s.

**Step 3:** We generate a SPECIFEM mesh matching the QDYN mesh and store the nodes coordinates in `nodesonfault`. In SPECIFEM we set the time step to 0.005 s (as dictated by the mesh) and run 60000 steps with a total target simulation time of 300 s, which is sufficient to allow an event to nucleate and rupture the whole 512 km fault from one side to another (extreme scenario). Accordingly, we set `t_dyn = 300 s` in `QDYN_to_SEM_RSF_f.m`

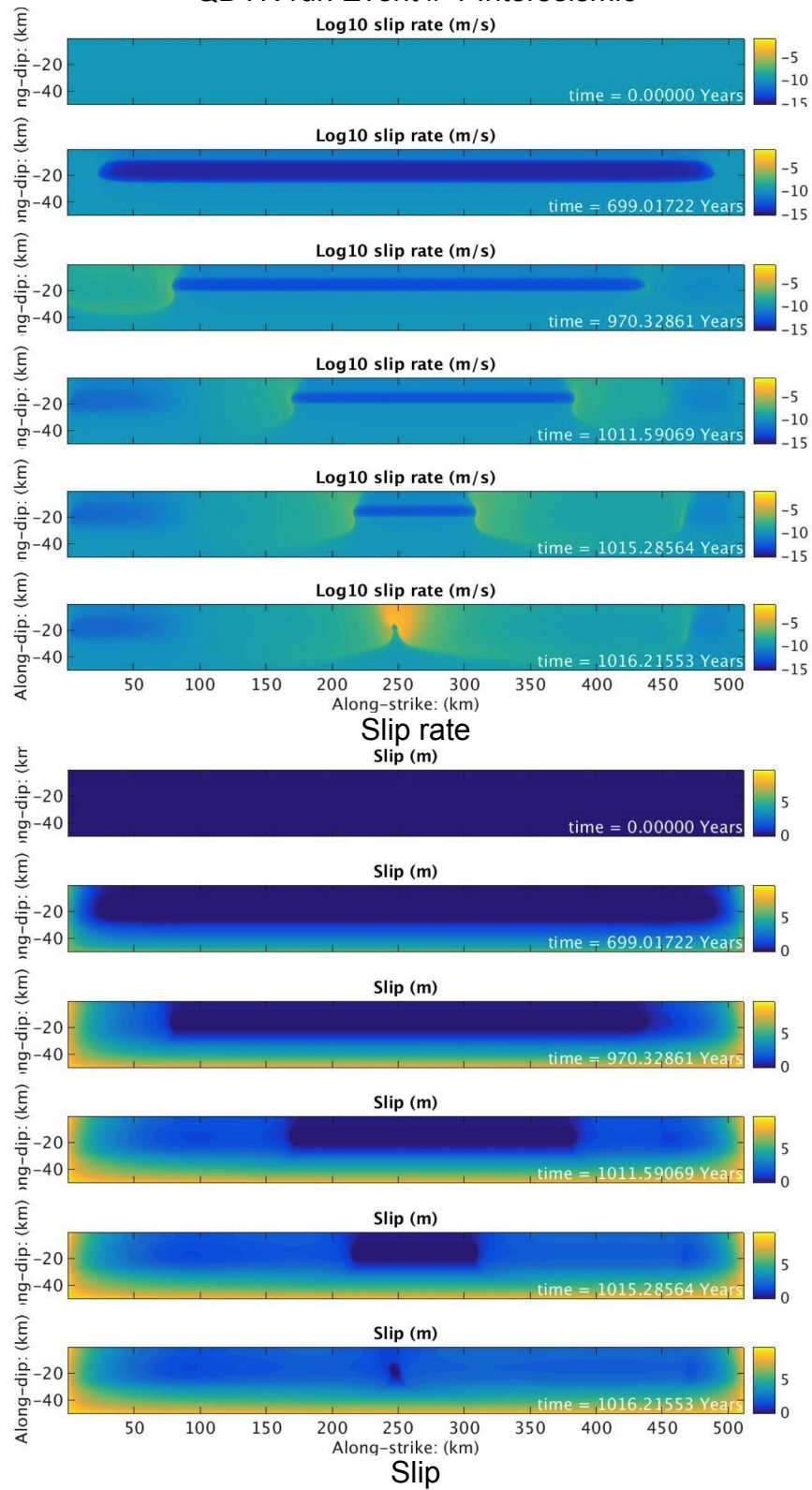
**Step 4:** We run the script `QDYN_SPECIFEM_bridge.sh` on our cluster with command `qsub run_bridge_sh`

**Step 5:** The monitoring file shows typically [this](#):

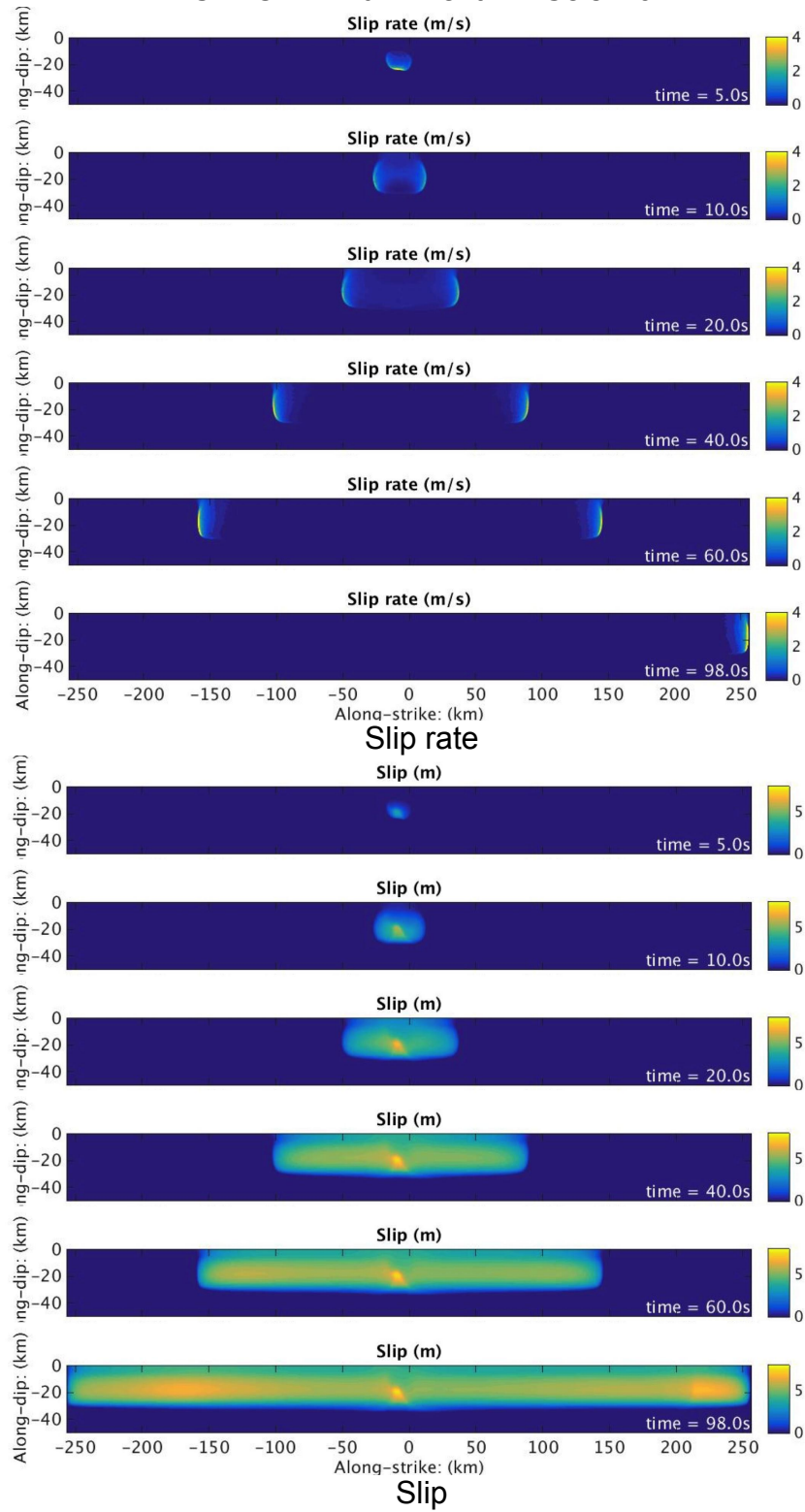
```
N_core_allco = 108
N_loop = 2
Tue Aug 4 03:01:49 PDT 2015
QSB: run no. 1
QSB: run no. 1 QDYN simulation ...
...
...
...
```

**Step 6:** Once the simulation of the 2 earthquakes is over, we process the outputs using matlab scripts `plot_QDYN_seq.m` and `plot_SEM_seq.m`. The figures below show results of a simulation comprising two earthquake cycles. They include the QDYN simulation of the two interseismic periods and the SPECIFEM3D simulation of two earthquakes. We show also the results of the first earthquake computed by QDYN only, to highlight the differences introduced by the fully dynamic effects.

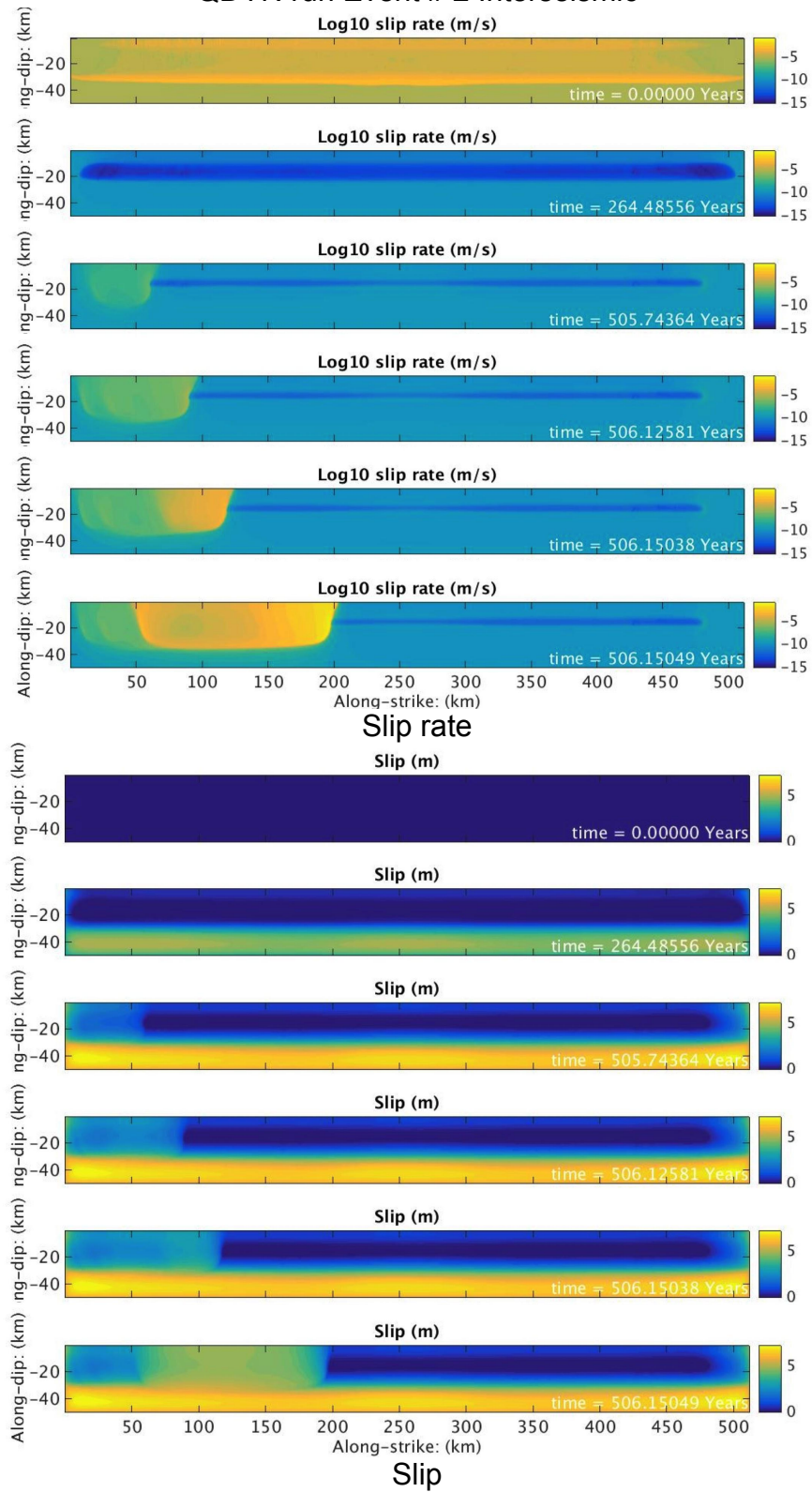
### QDYN run Event # 1 Interseismic



## SPECFEM run Event # 1 Seismic



### QDYN run Event # 2 Interseismic



### SPECFEM run Event # 2 Seismic

